AN ABSTRACT OF THE DISSERTATION OF

Chih-Heng Tseng for the degree of Doctor of Philosophy in Industrial Engineering presented on December 8, 2008
Title: Sources of Flow Maldistribution in Microreactor-Assisted Synthesis of Ceria Nanoparticles.

Abstract approved:

_____

Brian K. Paul

Recent efforts show that microchannel technologies have much to offer the field of nanomanufacturing: the structuring of matter on the order of one billionth of a meter. During the synthesis of nanomaterials, microchannel reactors take advantage of large surface-to-volume ratios to accelerate heat and mass transport. This accelerated transport allows for rapid changes in reaction temperatures and concentrations leading to faster, more uniform heating, cooling and mixing. This dissertation includes five chapters. Chapter 2 provides a comparison of conventional batch mixing and microchannel mixing (Tee-mixer) techniques for the synthesis of cerium oxide (ceria) nanoparticles. Results demonstrate the advantages of the micromixer approach including better control of nanoparticle shape and composition. Chapters 3 and 4 consider the scale-up of such nanomaterials for enabling new forms of microreactor-assisted nanomanufacturing. At flow volumes necessary for supporting nanomanufacturing, one of the key challenges in microreactor-assisted processing is flow maldistribution within microchannel components. Chapter 3 summarizes various mechanically-induced failure mechanisms known to impact flow maldistribution within microchannel arrays. In Chapter 4, one of these failure mechanisms is studied in more detail. Microchannel fin buckling has been observed during diffusion bonding due to the compressive stress caused by the lateral translation of the bonding pressure via Poisson's ratio. A theoretical model is described and validated using experimental results. Implications of the theoretical model are discussed.

Sources of Flow Maldistribution in Microreactor-Assisted Synthesis of Ceria Nanoparticles

by
Chih-Heng Tseng

A DISSERTATION

submitted to

Oregon State University

In partial fulfillment of
the requirements for the
degree of

Doctor of Philosophy

Presented December 8, 2008
Commencement June 2009

Doctor of Philosophy dissertation of Chih-Heng Tseng presented on December 8, 2008

APPROVED:

Major Professor, representing Industrial Engineering

Head of the School of Mechanical, Industrial and Manufacturing Engineering

---

Dean of the Graduate School

I understand that my dissertation will become part of the permanent collection of Oregon State University libraries. My signature below authorizes release of my dissertation to any reader upon request.

Chih-Heng Tseng, Author

ACKNOWLEDGEMENTS

The author acknowledges with gratitude the guidance and patience of my committee. Especially thanks are due to Dr. Brian K. Paul for giving me an opportunity to work with him for the last several years. The advice and support I got from him was very important to me. I learned not only the knowledge, but also the passion to pursue knowledge and to make the world of a difference. Special recognition is also due to several professors (Dr. Kevin Drost, Dr. Tom Plant, and Dr. Vince Remcho…etc.) that I interacted with over the course of my study.

The author would also like to thank all my friends in OSU. They are wonderful persons with great personalities despite different nationality. I like to thank them for standing beside me and provide me with help to continue my study. Thanks to Santosh Tiwari and Gopi Lingam for the support which helped me in finishing my dissertation. Thanks a million to Jack Rundel and Bruce Johnson for giving me quick feedbacks on my dissertation draft.

I would also like to express my sincere appreciation to my parents for providing me both mental and financial support throughout my study. Last but not least the author would like to express my gratitude to my wife, Sandy Chen who gave me the strength in completing my PhD.

TABLE OF CONTENTS

TABLE OF CONTENTS (Continued)

Page

TABLE OF CONTENTS (Continued)

TABLE OF CONTENTS (Continued)

Page

LIST OF FIGURES

LIST OF FIGURES (Continued)

Figure Page

LIST OF FIGURES (Continued)

Figure Page

LIST OF FIGURES (Continued)

Figure Page

LIST OF TABLES

LIST OF APPENDICES

Sources of Flow Maldistribution in Microreactor-Assisted Synthesis of Ceria Nanoparticles

CHAPTER 1

Introduction

Recent efforts show that microchannel technologies have much to offer the field of nanomanufacturing. In synthesis, microchannel reactors take advantage of the large surface-to-volume ratios to accelerate heat and mass transport. This accelerated transport allows for rapid changes in reaction temperatures and concentrations leading to non-gradient/uniform heating and mixing.

Chapter Two compares the conventional batch mixer results with a Tee-mixer. The system chosen is cerium oxide (ceria). Cerium oxide (ceria) nanoparticles were synthesized continuously from a microchannel mixer. Comparisons were made between the nanoparticles' characteristics produced by traditional batch mixer and a Tee-mixer. Results show advantages of the micromixer approach including better control of nanoparticle shape, film morphology, and composition.

However, nanomanufacturing also considers mass production and deployment of nanotechnology: the structuring of matter on the order of one billionth of a meter. The manufacturing needs, at this scale, are complicated by the sheer number of matters required to make a functional structure. To satisfy the need, large volumes of reactants are needed. At these production volumes, quality control and material manipulation become extreme. One of the key parameters is to control flow maldistribution in the microchannel device. Chapter Three summaries main sources of flow maldistribution and found that most of the sources can be minimized by appropriately selection of applications. However, mechanically induced warpage have significant effect and needs

to be addressed so the defect modes and causes are then discussed and analyzed.

Chapter Four focuses on one of the defect modes, which is Poisson's effect. This warpage mechanism is observed when the structure is subjected to compressive pressure (longitudinal stress). When converted to lateral stress due to Poisson's effect, it will translate to side loading and compresses the microchannel structures within the device. In this study, a theoretical model was developed and compared with the experimental results.

Finally, in Chapter Five, all the key findings from this research are summarized.

CHAPTER 2

Continuous Nanomanufacturing Synthesis of Ceria Nanoparticles from a Microchannel Mixer

2.1 Abstract

Cerium oxide (ceria) nanoparticles are synthesized continuously from a micromixer. Comparisons were made between the nanoparticles' characteristics produced by traditional batch precipitation and a continuous flow micromixer (Tee-mixer). Experiments were carried out by varying the reactant concentration level. Results show advantages of the micromixer approach including better control of nanoparticle shape, film morphology, and composition.

2.2 Introduction

Nanomanufacturing considers the mass production and deployment of nanotechnology: the structuring of matter on the order of one billionth of a meter. Current "bottom-up" production schemes involve the synthesis and assembly of nanobits such as nanoparticles, quantum dots and macromolecules to produce novel structures with manifold performance advantages. The manufacturing needs, at this scale, are complicated by the sheer number of bits required to make a functional structure. Consider the assembly of a 300 nm anti-reflective thin film on the surface of a 50 mm diameter lens using 20 nm nanoparticles. Over 100 trillion nanoparticles would be needed. At these production volumes, quality control and material manipulation become extreme.

Recent efforts show that microchannel technologies have much to offer to the field of nanomanufacturing. In synthesis, microchannel reactors take advantage of the

large surface area-to-volume ratios to accelerate heat and mass transport. This accelerated transport allows for rapid changes in reaction temperatures and concentrations leading to more uniform heating and mixing. Other features include better defined flow characteristics and integrated separation. Microreactors have been demonstrated to have dramatic impacts on macromolecular yields (Chang et al., 2005) and nanoparticle size distributions (Nakamura et al., 2002; Chan et al., 2003; Yen et al., 2003; Krishnadasan et al., 2004).

In assembly, nanoparticles and macromolecules can be mixed, dispersed or functionalized *in channel* and directly deposited onto flat or contoured surfaces with minimal nanobit agglomeration. At Oregon State Univeristy, microreactors have been found to be compatible with various film deposition techniques by dispensing reactant streams directly onto moving or stationary substrates yielding dense, functional, nanostructured films.

2.3 Literature Review

The following sections first summarize different applications and forms of cerium dioxide nanoparticles. Afterwards, general procedures and chemistries for synthesizing ceria nanoparticles are introduced and compared. After comparison, the precipitation approach is discussed in terms of different control parameters during nanomanufacturing.

2.3.1 Cerium Dioxide (Ceria)

Ceria (CeO_2) has drawn much attention in recent years due to its distinctive characteristics, such as unique UV absorptivity (Tsunekawa et al., 2000), high stability and hardness at high temperature, and high reactivity to oxygen (Trovarelli et al., 1999).

Unique optical characteristics such as Raman-allowed modes shifting and broadening (Tsunekawa et al., 2000); lattice expansion; and the blue shift in ultraviolet absorption spectra (Tsunekawa et al., 2000) have been reported. Catalytic applications such as support or promoter for exhaust-gas conversion (three-way catalyst application, TWC) (Bekyarova et al., 1998), oxygen ion conductor in fuel cells (Yahiro et al. 1988), and gas sensors (Izu et al., 2002) have also been reported.

With such variety of applications, different forms (particle, mesoporous membrane/film, or composite membrane/film) of CeO_2 had been proposed and analyzed. In particular, nanometer CeO_2 particles have greatly been exploited because of the significant size-induced property changes. In oxygen sensor applications, by changing the particle size from micrometers to hundreds of nanometers, the response time shortened from minutes to milliseconds (Izu et al., 2002). This suggests that the surface adsorption or surface reaction was improved by reducing the particle size. Moreover, nanocrystalline CeO_2 particles have allowed 200-400°C decreases in sintering temperature when compared with micron sized CeO_2 particles (Hirta et al., 2005). In this case, nanoparticles with small radius of curvature and high surface area remarkably reduce the sintering temperature. To further investigate and facilitate these property enhancements, it is important to identify a rapid way to synthesize different sizes/morphologies of the nanoparticles with a narrow size distribution.

2.3.2 Ceria Nanoparticle Synthesis

Over the past few years, several methods had been proposed for producing CeO_2 nanoparticles, such as the sol-gel process (Chu et al., 1993), hydrothermal or solvothermal synthesis (Hakuta et al., 1998), forced hydrolysis (Dong et al., 1997), microemulsion (Masui et al. 1998), precipitation (Hsu et al., 1988), etc. In the sol-gel process, alkoxide or organometallic compounds are usually used as precursors. These precursor materials are generally expensive and lead to complicated reaction

mechanisms that often restrict the use of sol-gel processing (Zhou et al., 2002). The hydrothermal synthesis and forced hydrolysis are often carried out under more severe conditions, such as higher temperature, higher pressure, and longer reaction time.

Researchers at Pacific Northwest National Laboratory (PNNL) have invented a flow-through hydrothermal technique to produce highly monodispersed nanoparticles referred to as the Rapid Thermal Decomposition of precursors in Solutions (RTDS) (Darab et al, 1994; Darab et al., 1999). However, this process suffers from the drawbacks of traditional hydrothermal synthesis mentioned before. Microemulsion is an efficient method for preparing highly monodispersed CeO_2 nanoparticles, but is hard to scale up commercially.

Compared to these methods, precipitation is a more attractive method/route due to the cheap salt precursors, simple operation, and ease for mass production (Zhou et al., 2002).

2.3.3 Precipitation of Ceria Nanoparticle

The precipitation approach generally involves an intermediate formation (see Figure 2-1) of metal hydroxides, nitrites, sulfates, oxalates, and so forth (Wang and Feng, 2000). In most cases, these precursor powders must be thermally decomposed to obtain the desired ceramic powder (Ring, 1996). Thus if the ideal result is to form nanoparticles, intermediate precursor powders have to be separated from their supernatants by drying and calcination. On the bottom of Figure 2-1, the precursor and the intermediate form used in this dissertation are listed.

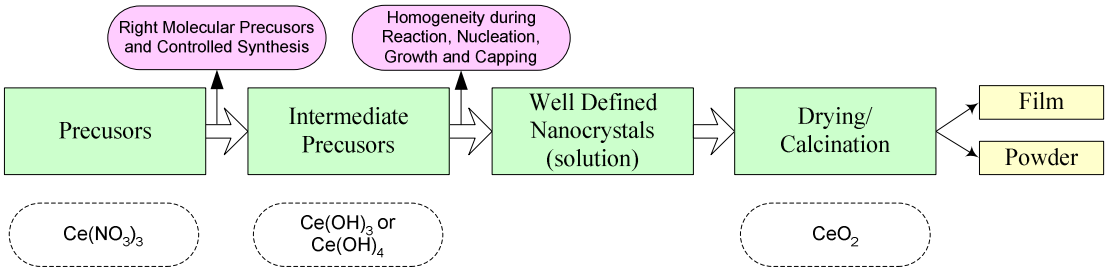

Figure 2-1. Flow chart of the precipitation procedure assuming solution chemistry.

The precipitation process used in this dissertation starts with dissolving $Ce(NO_3)_3$ (cerium nitrate) in deionized water expressed as

$$2Ce(NO_3)_3 \xrightarrow{H_2O} 2Ce^{3+} + 6NO^{3-} \tag{2-1}$$

According to this equation, hydration of the nitrate generates Ce^{3+}. Since the desired final product is CeO_2 (ceria), the Ce^{3+} ion must go through an oxidation transition to a Ce^{4+} ion, that is

$$2Ce^{3+} \longrightarrow 2Ce^{4+} + 2e^- \tag{2-2}$$

When dissolved in water, according to the emf (electromotive force) data (Weast, 1984), the transition can be expressed as

$$Ce^{3+} + H_2O \Leftrightarrow Ce(OH)^{3+} + H^+ + e^-$$
$$E^\circ_{OX} = -1.70V \tag{2-3}$$

Thus, an increase in emf can be realized by changing the pH to a higher value. This favors the hydrolysis of the relatively large Ce^{3+} ion,

$$Ce^{3+} + OH^- \Leftrightarrow Ce(OH)_3 \tag{2-4}$$

To increase the pH value (facilitate the oxidation process), NH_4OH (ammonium hydroxide) is added to the solution. When NH_4OH dissolves in water, it becomes protonated. Hence ammonium and hydroxide ions will be present in the aqueous solution of ammonia according to

$$NH_3 + H_2O \rightarrow NH_4^+ + OH^- \quad (2\text{-}5)$$

When the pH value is changed, immediately $Ce(OH)_3$ (cerium(III) hydroxide) precipitates out because the solubility constant ($K_{sp}=6.3\times10^{-24}$ at 25℃) is extremely low (Chen et al. 2004). This phenomenon is thermodynamically driven, which will be explained in the next section. The hydroxide then experiences a Ce^{3+} to Ce^{4+} transition. This transition involves Ce^{3+} ions having contact with oxygen. This reaction is expressed in formula (2-6). Zhou et al., 2003 further proved that particle size of the CeO_2 can be reduced by bubbling oxygen into the solution to react with $Ce(OH)_3$. This finding indicates that by controlling the precipitation condition, the nanoparticles size and size distributions of the nanoparticles can be changed.

$$2Ce(OH)_3 + \tfrac{1}{2}O_2 \rightarrow 2CeO_2 + 3H_2O \quad (2\text{-}6)$$

2.3.4 Nanoparticle Size and Size Distributions

Since CeO_2 is the direct product of $Ce(OH)_3$, all variables described in this section are associated with $Ce(OH)_3$. According to Eq (2-4), intermediate $Ce(OH)_3$ particles are formed. It can be calculated according to the system's thermodynamic offset from equilibrium (Jones, 2002; Mullin, 2001)

$$\Delta G^* = \frac{16\pi v^2 \gamma^3}{3(kT)^2 (\ln S)^2} \tag{2-7}$$

where ΔG^* is the Gibbs free energy reduced from the supersaturated state to equilibrium, v is the molecular volume of the $Ce(OH)_3$ (which can be substituted with m/ρ where m is the molecular weight and ρ is the density of the $Ce(OH)_3$ molecule), γ is the surface/interfacial energy, k is the Boltzmann's constant, T is the temperature, and S is the supersaturation value. From the equation, supersaturation S and temperature T are the variables for changing ΔG^*. Assuming all experiments are operated in the same temperature, the supersaturation value becomes the only variable in the precipitation process. The supersaturation value can then be calculated according to

$$S = \frac{\left[Ce^{3+}\right] \cdot \left[OH^-\right]^3}{K_{SP}} \tag{2-8}$$

where K_{SP} is 6.3×10^{-24} at 25°C (Chen et al. 2004). From Eq. 2-8, the supersaturation value (S) increases significantly when $[OH^-]$ increases. Therefore according to Eq. (2-8), when the supersaturation value is high, the thermodynamic offset ΔG^* becomes low. This would result in the $Ce(OH)_3$ haing small nuclei size (r^*), which can be calculated using Eq. 2-9. The relationship between ΔG^* and r^* is demonstrated in Figure 2-2.

$$r^* = \frac{2\upsilon\gamma}{kT \ln(S)} \tag{2-9}$$

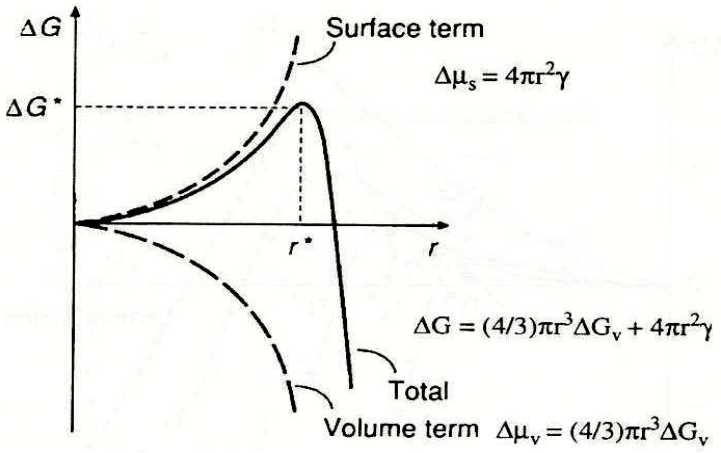

Figure 2-2. Dependence of nuclei size r* on Gibbs free energy ΔG* (Jones, 2002; Mullin, 2001).

From Eq. 2-7 and Eq. 2-9, when supersaturation *S* is high, the thermodynamic offset Δ*G** and nuclei size *r** become small. Thus, by assuming the size of the nanoparticles relatively the same as the nuclei size, it is expected that the varying supersaturation value *S* will result in changes in the nanoparticle size. Consequently, from Eq 2-9, uniform mixing of the [Ce^{3+}] and [OH^-] becomes crucial for obtaining a narrow distribution of particle size. This indicates that the design of the mixer is important for the precipitation process.

2.3.5 Controlling Nanoparticle Precipitation Synthesis

According to previous discussions, varying the reactant mixing condition (exposure to oxygen) would affect nanoparticles size and size distribution. The following literature review summarizes different approaches to precipitate CeO_2 nanoparticles.

One approach is to decrease the rate of pH change that allows time for the batch mixer to fully mix the reactants. Chu et al., 1993 selected $(NH_2)_2CO$ (urea) and Chen et al. 1993 selected $C_6H_{12}N_4$ (hexamethylenetetramine or HMT) for their experiments. By

using urea, it slowly decomposes to ammonia and HNCO, thus the major ligands are OH^- ions and CO_3^{2-} ions. On the other hand, when HMT is heated to higher temperature, it slowly hydrolyzes to yield ammonia and formaldehyde (CH_2O), thus the major ligand in the solution is OH^- ions. By slowing down the change in pH, according to Eq. 2-4, the rate of precipitation can be reduced.

Another approach is to reduce the temperature on one of the reactants thus the kinetics is reduced. Zou et al., 2004 demonstrated that by adding 5°C H_2O_2 (hydrogen peroxide) to room temperature cerium(III) nitrate, the lower temperature H_2O_2 will slowly absorb heat from cerium(III) nitrate. Once the H_2O_2 reaches higher temperature, Ce^{3+}/Ce^{4+} transition starts to occur. This transition is expressed as

$$Ce^{3+} + H_2O_2 + 2H^+(aq) \Leftrightarrow Ce^{4+} + 2H_2O \qquad (2\text{-}10)$$

After transformation of Ce^{3+} to Ce^{4+}, ammonium hydroxide was added which is similar to the precipitation process described in Eq. 2-2 and Eq. 2-4.

Since controlling the formation of $Ce(OH)_3$ is crucial in controlling the particle size and size distribution, researchers have tried to mix the reactants with different chemicals to change the reactant property to adjust the kinetics. Hu et al., (2000) and Park et al., (1997) both changed the dielectric property of the reactants and successfully synthesized ZrO_2 and TiO_2, respectively. Recently, Chen et al., (2004) applied this concept to the CeO_2 system and achieved good control on the size of the nanoparticle. By changing the dielectric property of the reactant, the solubility of the dissolved solute (i.e. inorganic salt molecules) and the colloidal interaction between solid particles Chen et al., (2004) is affected.

The previously mentioned methods use either different chemicals (reactants) or conditions (temperature or reactant property) to optimize the kinetics of precipitation. In 2003, Zhou et al., 2003 focused on applying different “processing” parameters then validated the results. Parameters such as impeller speed, feeding method, and oxygen bubbling were tested and the characteristics of the ceria nanoparticles were verified.

Furthermore, they validated the effect of oxygen exposure expressed in Eq. 2-6 and indicated that the nanoparticles become smaller when exposed to oxygen. These findings demonstrate that the processing parameters are as important as the chemical parameters when precipitating fine nanoparticles.

Schwarzer et al., 2004 and Kockmann et al., 2007 used a Tee-mixer setup to validate experimentally, as well as numerically, a classical precipitation model using barium sulfate. The results showed that narrow particle size distribution was achieved by changing the input flow rate (Reynolds number: 127 to 15280) and supersaturation value (concentration of reactants). They concluded that the time scales of precipitation (for barium sulfate system) depend strongly on the effective supersaturation of the reactants and can vary from a few microseconds to more than 100 milliseconds. This indicates that mixing is the most crucial step for precipitating fine nanoparticles. The results also demonstrated that enhanced mixing could be achieved by using microchannels.

2.4 Hypothesis

Based on the literature review, microchannel mixing will also provide uniform mixing and residence time for ceria precipitation. This allows better control of the precipitation process.

2.5 Preliminary Experimental Approach

Both batch mixer and the microchannel Tee-mixer configurations were tested. The objective is to validate the hypotheses by changing the reactant concentration for each mixer configuration. Two sets of concentration level were used in the experiment and the results were characterized.

2.5.1 Parameters

Two sets of concentration levels, experiment (i) and (ii), were used for both batch mixer and the Tee-mixer. In experiment (i), higher amount (0.0375M) of cerium nitrate was used then lower amount (3mL) of NH_4OH was added. For experiment (ii), lower amount (0.0187M) of cerium nitrate was used then higher amount (5mL) of NH_4OH was added.

2.5.2 Experimental Setup

An analytical balance (Acculab AL Analytical Series AL-104) was used for measuring the amount of the cerium(III) nitrate. The quantity of ammonium hydroxide was measured then applied to the batch mixer by a pipettor (EPPENDORF® REPEATER™ PLUS Pipettor). Both equipment are shown in Figure 2-3.

Figure 2-3. Acculab AL analytical balance (left) and Pipettor from Cole-Parmer (right).

To pump the reactants through the Tee-mixer (P-728, Upchurch Figure 2-4), a peristaltic pump (ISM 833, Upchurch Figure 2-5) was used. The advantage of using a peristaltic pump is that the reactants are not exposed to the pumping mechanism; this prevents clogging by reducing contamination. In addition, the setup is relatively easy.

Figure 2-4. High pressure PEEK™ Tee-mixer purchased from Upchurch Scientific.

Peristaltic Pump

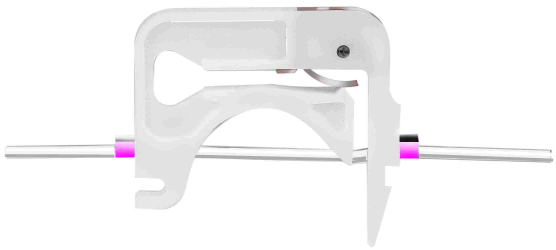

Cassettes for the Peristaltic Pump

Figure 2-5. Peristaltic pump (ISMATEC 833) purchased from Upchurch Scientific.

2.5.3 Experimental Protocol

The experimental protocol was separated into two sections. One is for batch mixer and the other is for Tee-mixer approach. After synthesizing, the nanoparticles were then deposited onto quartz substrates for characterization purposes.

2.5.3.1 Batch Mixer

For batch mixer approach, (shown in Figure 2-6), cerium(III) nitrate was dissolved in D.I. water then ammonium hydroxide (NH_4OH) was pipetted in until the pH is above 10. When pH >10, precipitation/nucleation of ceria nanoparticles takes place then followed by particle growth. As described before, the difference between experiments (i) and (ii) is the molar concentration level. By changing the [Ce^{3+}] and [OH^-] concentration, the supersaturation value S is changed. The supersaturation value S can be calculated by Eq. 2-8. When [OH^-] increases, the supersaturation value increases significantly. In theory, higher supersaturation value results in smaller nanoparticle size.

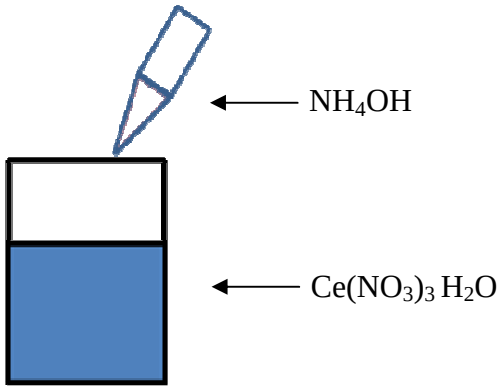

Figure 2-6. Schematic diagram of the batch mixer approach.

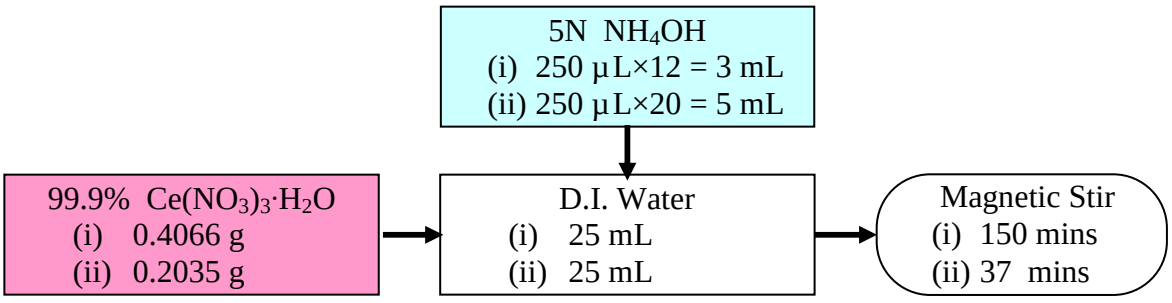

Figure 2-7. Batch mixer precipitation process procedure.

In the batch mixer approach, experiment (i) involves using 0.0375M of cerium nitrate (given that the molar mass for cerium nitrate is 434.22 g/mole), and then 3mL of NH4OH was pipetted in with increments of 250μL. For experiment (ii), 0.0187M of cerium nitrate was used then 5mL of NH_4OH was applied with the same increment as experiment (i) (shown in Figure 2-7). The reactants were mixed using a magnetic stirrer with at 500 rpm.

2.5.3.2 Tee-Mixer

The protocol for the Tee-mixer approach is shown in Figure 2-8. Since the peristaltic pump can only function when the two reactants have equal amount of volume (same flow rate), different amounts of D.I. water were used to dissolve cerium(III) nitrate and dilute ammonium hydroxide. Overall, the amount of reactants and solvents used in the Tee-mixer is roughly the same as the batch recipe. After the cerium(III) nitrate and the dilute ammonium hydroxide were pumped through the Tee-mixer, the resultant solution was immediately transferred and poured into a beaker with 50mL of D.I. water. The idea is to terminate the reaction by reducing the pH value. As mentioned before, the precipitation/nucleation of the ceria nanoparticles take place when pH >10.

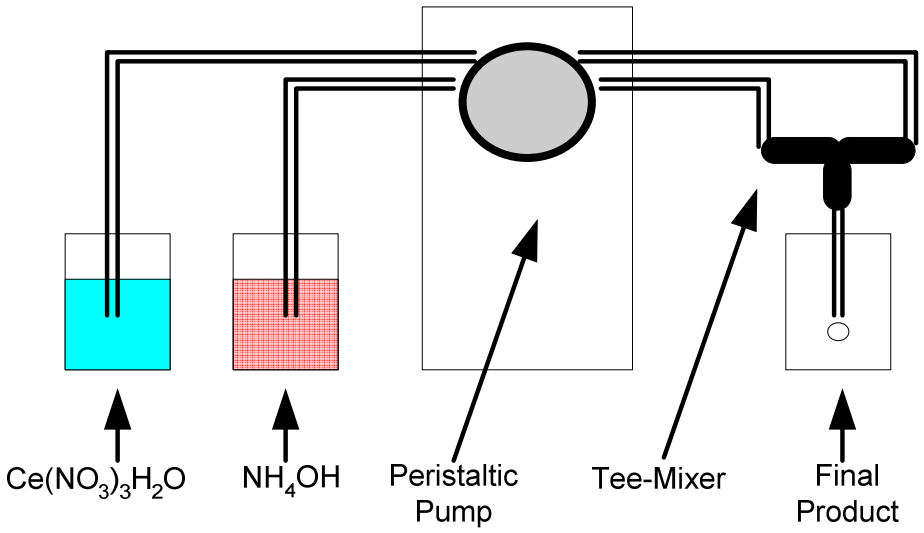

Figure 2-8. Schematic diagram of the batch mixer approach.

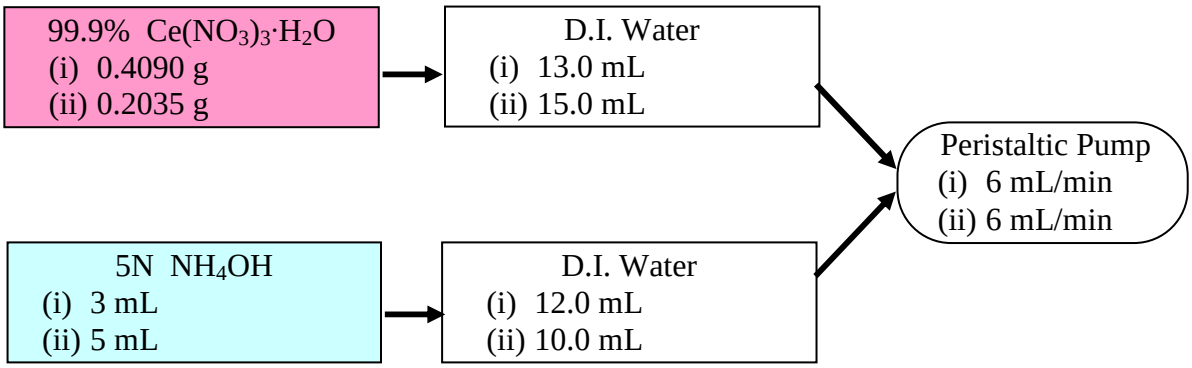

Figure 2-9 Tee-mixer precipitation process procedure.

Again, two levels of conditions were performed in the Tee-mixer approach driven by the peristaltic pump. For experiment (i), 0.0375M of cerium nitrate was introduced on one side and 3mL of NH_4OH was introduced on the other side of the Tee-mixer. For experiment (ii), 0.0187M of cerium nitrate was used and 5mL of NH_4OH was applied (Figure 2-9).

According to the protocols (Figure 2-7 and Figure 2-9), the concentrations of the cerium(III) nitrate and the ammonium hydroxide from the Tee-mixer experiments were higher than the batch mixer experiments. In this experiment, it was assumed that the

reactants are fully mixed before the reaction starts. Thus it was assumed that the concentrations of the reactants used in the Tee-mixer experiments were essentially the same as those of the batch mixer experiments. This was a good assumption based on the experimental results reported by (Schwarzer and Peukert 2004) for the precipitation of barium sulfate. The mixing time for that particular system was reported to be less than 100 milliseconds.

2.5.3.3 Film Deposition

After the completion of reaction, the resultant solution was spin coated onto a quartz substrate for further characterization. The spin coating process was carried out in two sequential steps. In the first step, 500 rpm (100 rpm/sec acceleration) was employed for 10 seconds. During this step, about 8mL of the resultant solution was slowly dropped onto the substrate. For the second step, the spincoater was ramped up to 2500 rpm (300 rpm/sec acceleration) then held for 30 seconds. This spun away extra colloidal solution and accelerated the evaporation of D.I. water. The coated substrates were then kept at 90°C for 12 hours.

2.5.4 Characterization

The morphology of the prepared CeO_2 nanoparticles was observed with transmission electron microscope (TEM, FEI Tecnai F-20 field emission high resolution) at Portland State University. The preparation of the samples was carried out by dropping an appropriate amount of CeO_2 suspension onto a copper grid with tissue paper on the bottom.

The CeO_2 nanoparticle suspension was also deposited onto quartz substrates. To characterize the sample, a Zeiss Ultra scanning electron microscope (SEM, Micro

Analytical Facility, CAMCOR, Univ. of Oregon) was used to examine the structure of the cerium oxide. Furthermore, the elemental distribution of the sample surface was also collected by energy dispersive X-ray spectroscopy (EDS).

2.6 Preliminary Results

The preliminary results were compared using different nanoparticle characterization techniques such as appearance, scanning electron microscopy, energy dispersive X-ray spectroscopy, and transmission electron microscopy.

2.6.1 Appearance

Due to the characteristic of poor mixing in the batch mixer, a longer time was needed for experiment (i) when the molar concentration of [OH−] was lower. Batch mixing required 162 minutes to form light yellow precipitates (CeO_2) in experiment (i) (shown in Figure 2-10) and experiment (ii) required 37 minutes.

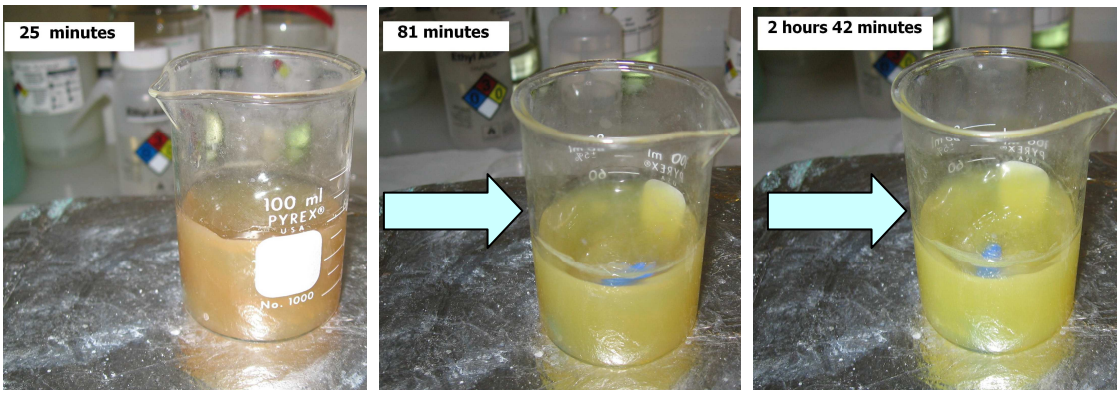

25 minutes 81 minutes 162 minutes

Figure 2-10. Change of color with regard to reaction time for the batch mixer in experiment (i).

With flow rate of 6mL/min, the Tee-mixer finished the process within 2.5 minutes for experiment (i) and (ii). Both resultant nanoparticles were purple colored instead of yellow as compared with the batch mixing experiment (shown in Figure 2-11). Based on past work, purple colored nanoparticles suggests the presence of $Ce(OH)_3$ (Chen et al., 2004) in the solution. Further characterization needs to be performed by XPS to verify the composition of the purple nanoparticles. This is an interesting result suggesting an additional potential benefit to the microreactor approach. Abi-aad et. al. 1993 had reported that $Ce(OH)_3$ is extremely sensitive to oxygen environment. Thus in the batch reaction, the length of time needed to mix the reactants causes enough exposure to ambient oxygen that the process progresses directly to its end product (CeO_2). In contrast, the nanoparticles generated from the micromixer maintain the form of $Ce(OH)_3$ until after deposited on a surface and dried. The light purple colored $Ce(OH)_3$ then undergoes a transition to CeO_2 yielding a resultant color change to light yellow.

Figure 2-11. Results from experiment (i) for batch (left) and Tee-mixer (right).

2.6.2 Scanning Electron Microscopy (SEM)

The SEM images (Figure 2-12) show significant differences in the morphologies of both the nanoparticles and the films. The batch mixer tends to have smaller particles but the particle size distribution tends to be wider. The film structure

from the batch mixer is more complex and less uniform. Another interesting finding from the Tee-mixer results (Experiment ii which had lower [Ce^{3+}] molar ratio and higher ammonium hydroxide concentration), the structures appear to be “sticks” or nanorods. This is consistent with the technical literature which shows that [OH^-] has to be above a certain value to precipitate nanorods (Yamashita et. al. 2002). In addition from the morphologies, the nanoparticles from the batch mixer also show more agglomeration when compared to the Tee-mixer. This can be observed from Figure 2-12 that the Tee-mixer results tend to form more uniform coatings than the batch mixer results.

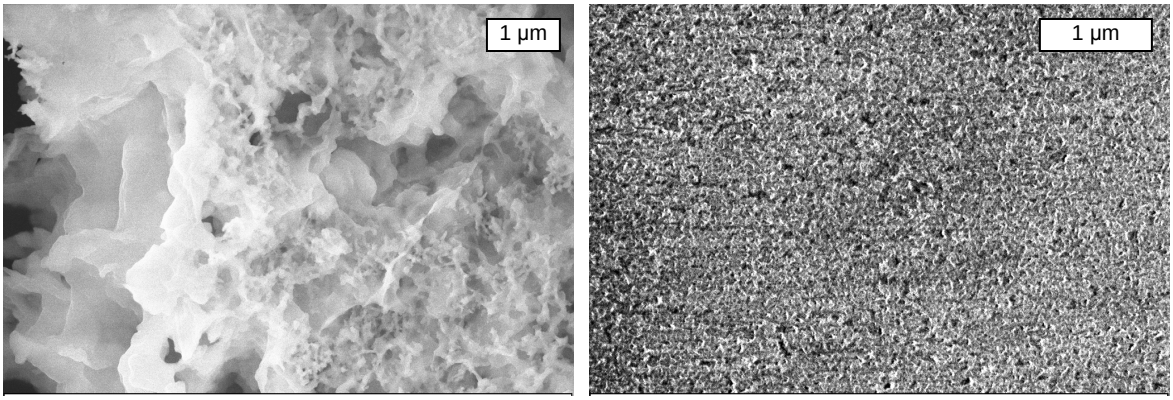

Experiment (i) using batch mixer Experiment (i) using Tee-mixer

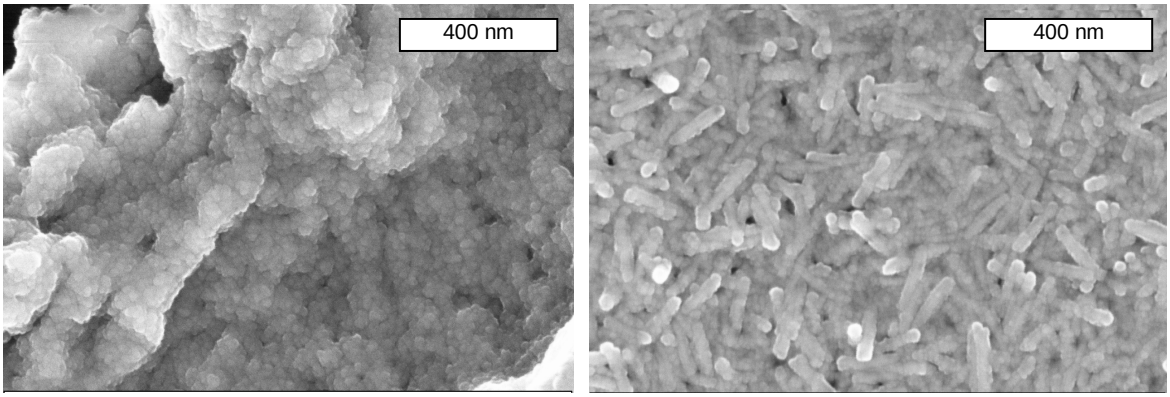

Experiment (ii) using batch mixer Experiment (ii) using Tee-mixer

Figure 2-12. Comparison of the film morphology by different synthesis approach and concentration.

2.6.3 Energy Dispersive X-ray Spectroscopy (EDS)

Though the morphologies of the nanoparticles were diversely different between the batch and Tee-mixer, EDS analysis (See Appendix A) shows similar results of a high percentage of Ce and O (which strongly implies the existence of CeO_2). A small carbon and potassium peak suggests a small amount of contamination due to normal environmental contact. The silicon peak was from the substrates.

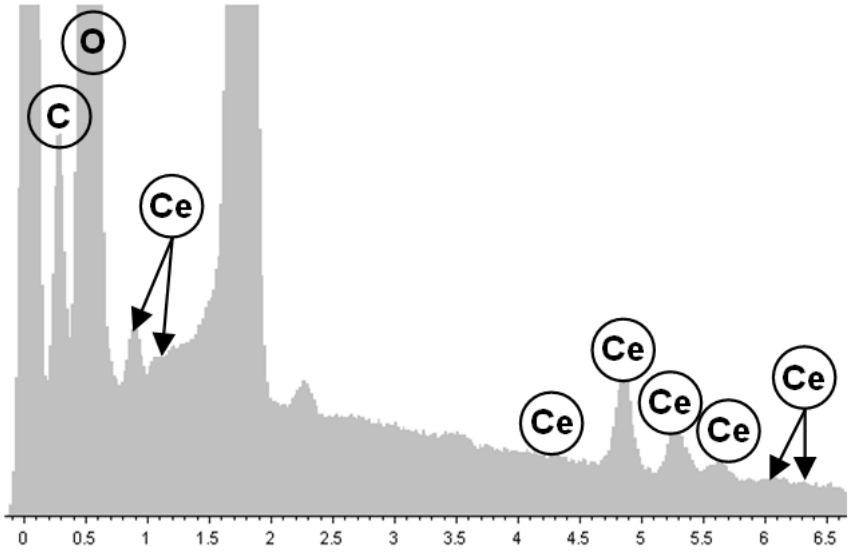

Figure 2-13. Energy dispersive X-ray spectroscopy results for films deposited from colloidal from Tee-mixer experiment (ii) indicates the existence of C, Ce, and O.

2.6.4 Transmission Electron microscopy (TEM)

The TEM results show that the nanoparticles from the batch mixer have an average size of about 5nm and those from the Tee-mixer an average size of have about 8nm. Interestingly, HRTEM images (Figure 2-14) gathered from the Tee-mixer samples

confirm the nanorod features. The nanorod analyzed from this image was found to have uniform atomic structure, which is suggestive of monocrystallinity.

Both results from the batch and the Tee-mixer show tendencies of particle agglomeration. However, the agglomeration was due to capillary forces mainly introduced during the drying process.

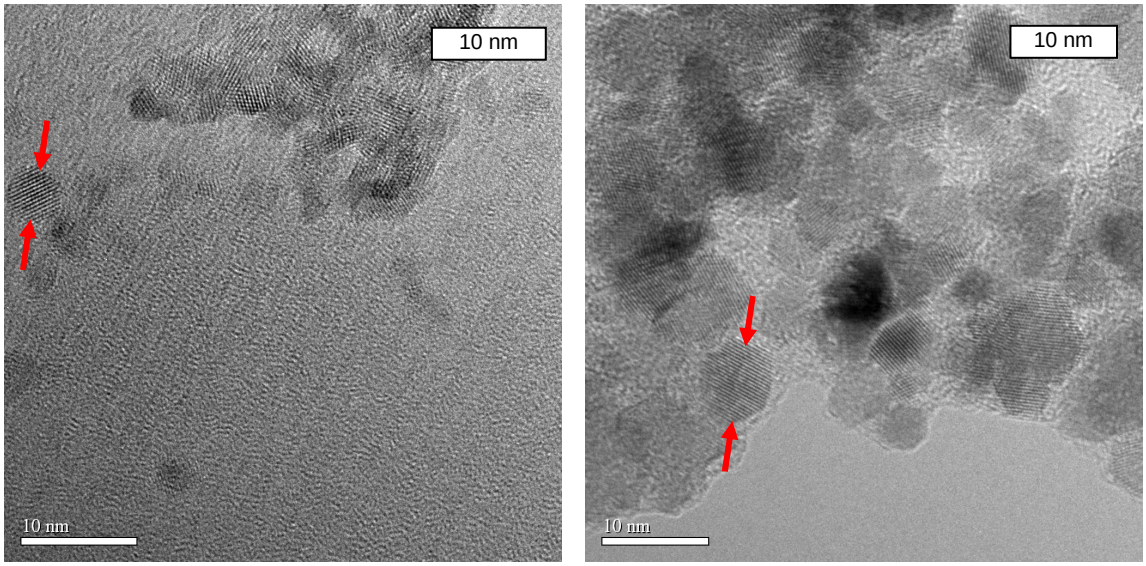

Experiment (i) using batch mixer Experiment (i) using Tee-mixer

Figure 2-14. TEM micrographs for the CeO2 nanoparticles prepared in batch mixer and Tee-mixer.

2.6.5 Preliminary Results Discussion

The preliminary results from the batch and Tee-mixer indicate that mixing is crucial in the ceria precipitation process. In batch mixing and deposition, agglomeration dominates the deposited film. In micromixing and deposition, more uniform films are attainable without the use of surfactants.

At high [OH−] concentration, results from the Tee-mixer yielded different nanoparticle morphologies than the batch mixer. This finding indicates that the

micromixer permitted the formation and capture of an unstable intermediate $Ce(OH)_3$ molecule by shielding the intermediate from exposure to the oxygen environment. However, further characterizations need to be done to validate the results.

In addition, to compare different synthesis approaches (shown in Figure 2-6 and Figure 2-8), the initial reactants need to have same quantity and concentration. Details of the new protocol will be discussed in subsequent paragraphs.

2.7 Experimental Approach

From preliminary study, micromixing approach yielded different nanoparticle morphologies. The nanorod formation was assumed to be formed from intermediate $Ce(OH)_3$ molecule thus additional characterization tools were used. The experimental protocols were changed based on the previous findings.

2.7.1 Batch Mixer

For batch mixer approach, (shown in Figure 2-15), cerium(III) nitrate and ammonium hydroxide (NH_4OH) were both dissolved/diluted in D.I. water. The volume for each reactant was kept the same to allow the Tee-mixer to have the same setup for experiment.

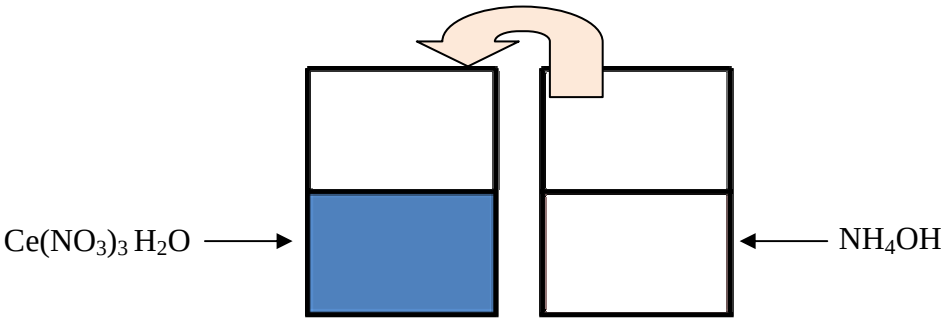

Figure 2-15 Schematic diagram of the batch mixer approach.

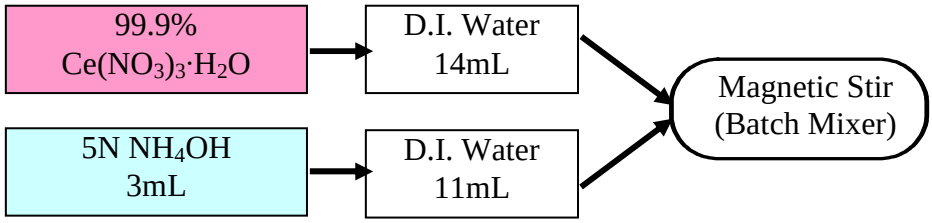

Figure 2-16. Batch mixer precipitation process procedure.

In this batch mixer approach, 0.0375M of cerium nitrate (given that the molar mass for cerium nitrate is 434.22 g/mole) was used. 3mL of NH_4OH was diluted with 11mL of D.I. water (shown in Figure 2-16). The reactants were mixed using a magnetic stir with 500 rpm.

2.7.2 Tee-Mixer

The protocol for the Tee-mixer approach is shown in Figure 2-17. As discussed before, the reactants were prepared the same way as the batch mixer samples. Shown in Figure 2-18, the only difference is the final mixing step.

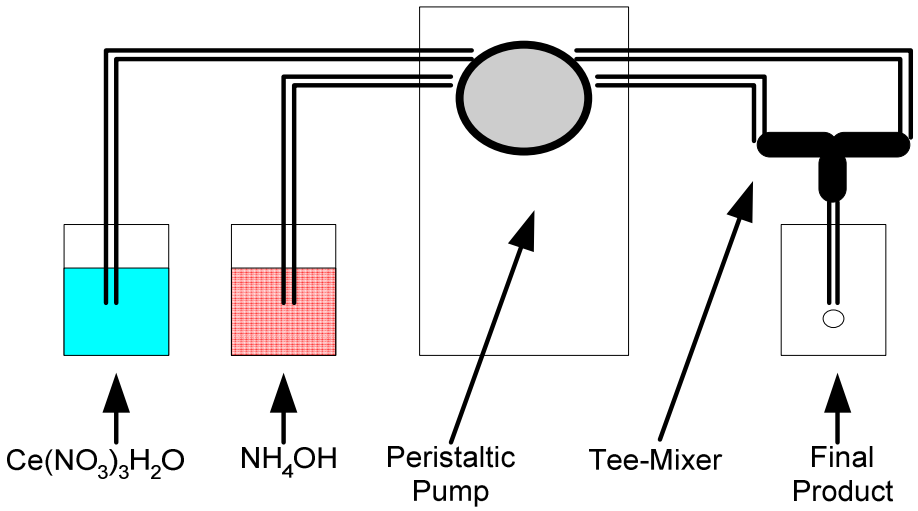

Figure 2-17. Schematic diagram of the batch mixer approach.

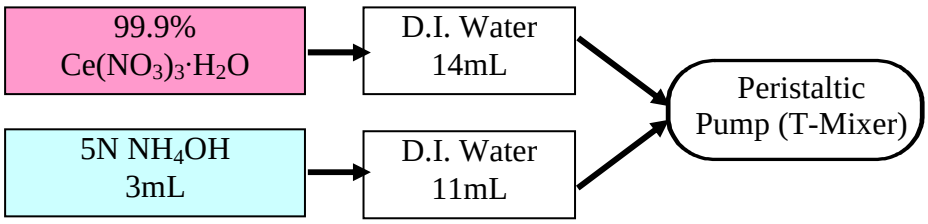

Figure 2-18. Tee-mixer precipitation process procedure.

2.7.3 Film Deposition

After the completion of reaction, the resultant solution was spin coated onto a quartz substrate for further characterization. The spin coating process was carried out in two sequential steps. In the first step, 500 rpm (100 rpm/sec acceleration) was employed for 10 seconds. During this step, about 8mL of the resultant solution was slowly dropped onto the substrate. For the second step, the spincoater was ramped up to 2500 rpm (300 rpm/sec acceleration) then held for 30 seconds. This span away extra colloidal solution and accelerated the evaporation of D.I. water. The coated substrates were then kept at 90°C for 12 hours.

2.7.4 Characterization

The morphology of the prepared CeO_2 nanoparticles was observed with transmission electron microscope (TEM, FEI Tecnai F-20 field emission high resolution) at Portland State University. The preparation of the samples was carried out by dropping an appropriate amount of CeO_2 suspension onto a copper grid with tissue paper on the bottom. Furthermore, the elemental distribution of the sample surface was also collected by energy dispersive X-ray spectroscopy (EDX).

The CeO_2 nanoparticle suspension was also deposited onto quartz substrates. To characterize the sample, a Zeiss Ultra scanning electron microscope (SEM, Micro Analytical Facility, CAMCOR, Univ. of Oregon) was used to examine the structure of the cerium oxide.

To characterize the chemical composition of the nanoparticles, X-ray diffractometer (XRD) was be used. The chemical (oxidation) state of nanoparticles is determined by X-ray photoelectron spectroscopy (XPS). This would differentiate the oxidation state from the CeO_2 sample to validate Ce^{3+} or Ce^{4+}.

2.8 Results and Discussion

The synthesized nanoparticles were characterized using different techniques. The chemical composition was characterized by X-ray diffraction. The nanoparticle size and morphologies were characterized by scanning electron microscopy and transmission electron microscopy. Finally, energy dispersive X-ray spectroscopy, and X-ray photoelectron spectroscopy was used to identify the compositions.

2.8.1 X-ray diffraction

To verify the chemical composition of the nanoparticles, the resultant nanoparticles were deposited onto a glass slide then dried for 12 hours at room temperature. Afterwards, the samples were characterized by X-ray Diffraction (XRD). The patterns from the XRD (see Figure 2-19) indicate that the nanoparticles are CeO_2 (PCPDF CAS#810792). In addition, the result from the Tee-mixer seems to have sharper peaks than the batch mixer. This suggests that the nanoparticles acquired from the micromixer approach are more crystalline.

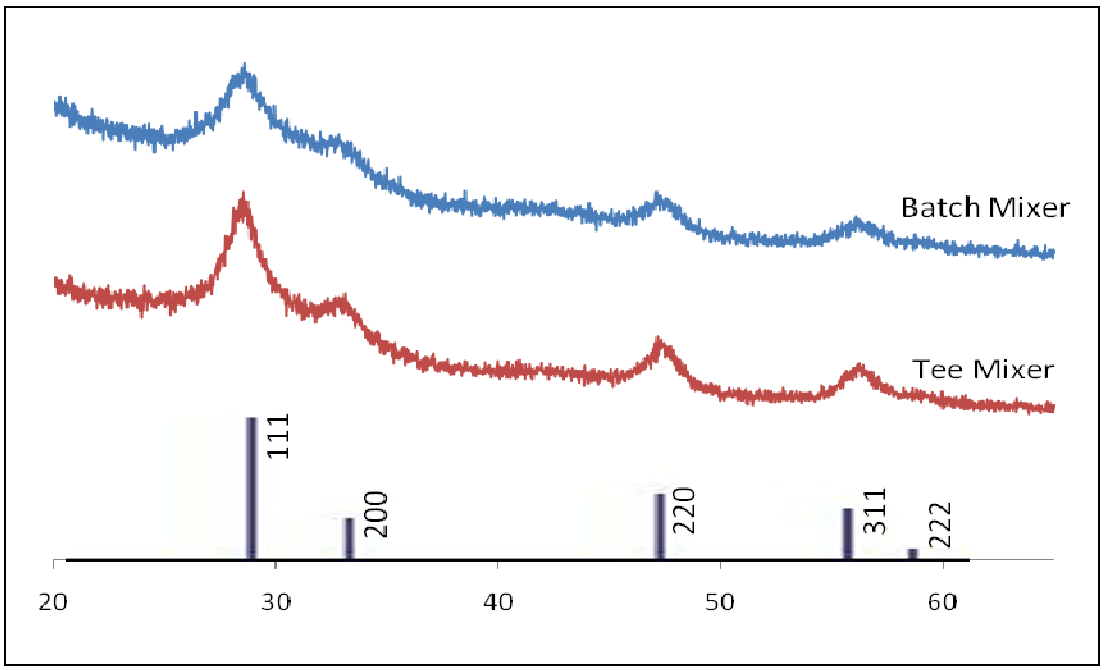

Figure 2-19. Powder XRD pattern of the product compared with reference to CeO2 PCPDF CAS #810792.

2.8.2 Scanning Electron Microscopy (SEM)

The SEM images (Figure 2-20 and Figure 2-21) show both approaches yields structures of “sticks” or nanorods. However, more nanoparticles (instead of nanorods)

were formed using the batch mixer approach. In literature, research has shown that the nanoparticles are formed by breakage from the nanorods (Mai et al. 2005). This indicates that the Tee-mixer approach retained more nanorods due to controlled mixing environment.

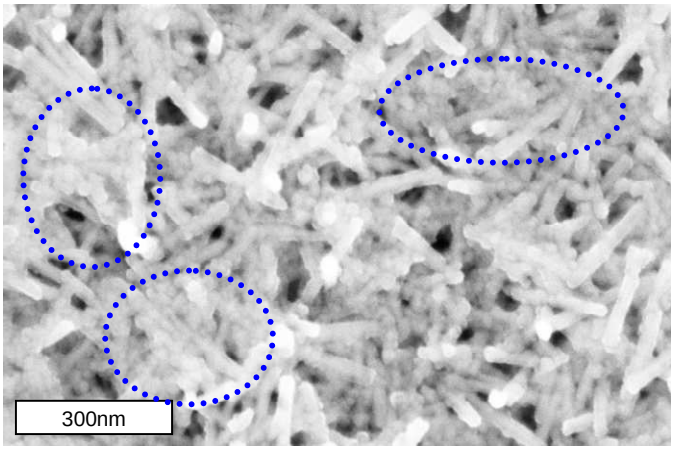

Figure 2-20. SEM image of nanoparticle morphology synthesized using batch precipitation approach. The circles indicate breakage of nanorods into nanoparticles.

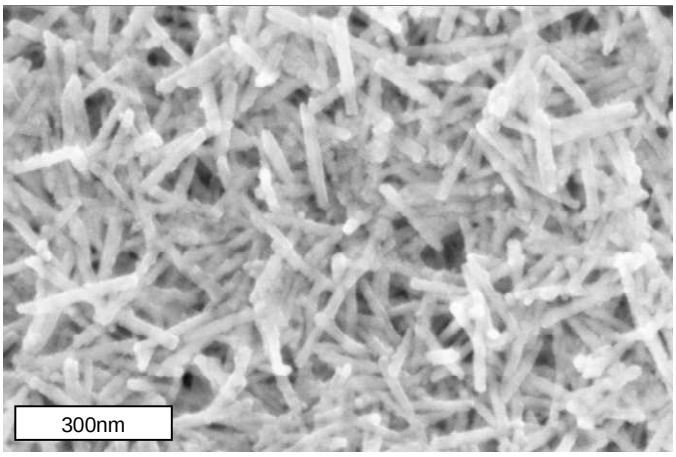

Figure 2-21. SEM image of nanoparticle morphology synthesized using Tee-mixer precipitation approach.

2.8.3 Transmission electron microscopy (TEM)

The TEM results show that both batch mixer and Tee-mixer (Figure 2-22) yields nanorod features. The nanorod analyzed from this image was found to have uniform atomic structure, which is suggestive of monocrystallinity.

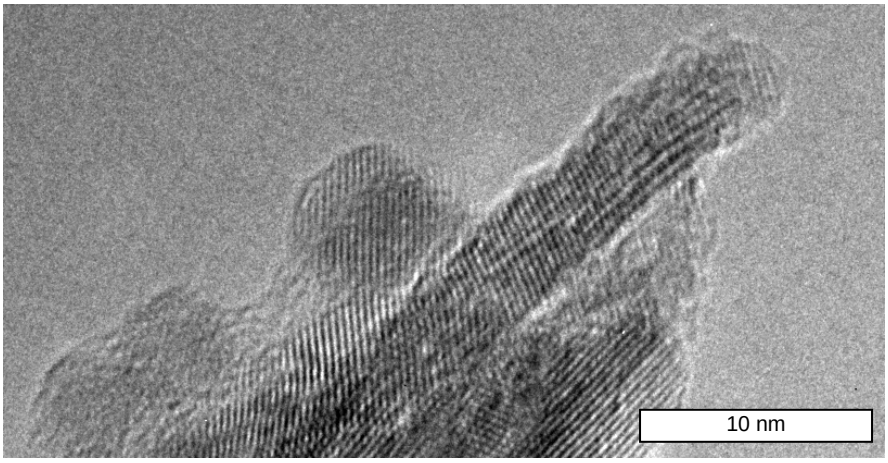

Figure 2-22. HRTEM micrograph of the “nanorod” from Tee-mixer.

2.8.4 Energy Dispersive X-ray Spectroscopy (EDS)

The EDX analysis (Appendix B) again showed similar results of a high percentage of Cu, Ce, and O (which strongly implies the existence of CeO_2). The copper peak was from the substrate used for carrying the nanoparticles. A small carbon peak suggests a small amount of contamination due to normal environmental contact.

2.8.5 X-ray Photoelectron Spectroscopy (XPS)

As described earlier, the micromixer approach reduced the probability of exposure to oxygen thus yield more Ce^{3+} ions which forms the intermediate $Ce(OH)_3$

instead of CeO_2. To quantify the results, an X-ray photoelectron spectroscopy (XPS) tool was used (Physical Electronics Incorporated Quantum 2000 Scanning ESCA Microprobe). The nanoparticles were deposited by pipette onto clean Si wafers inside a nitrogen purged I^2R glove bag attached to the XPS sample introduction chamber. The resultant solution was allowed to dry while inside the N_2 purged glove bag. The samples were then dried for approximately 10 minutes and mounted onto the XPS system specimen holder. The XPS high energy resolution photoemission spectral plots showed that the Ce^{3+} from Tee-mixer sample in clearly more than batch mixer samples (Figure 2-23). In addition, the N1s line is at 407 eV so the NH_3 was then oxidized as a nitrate.

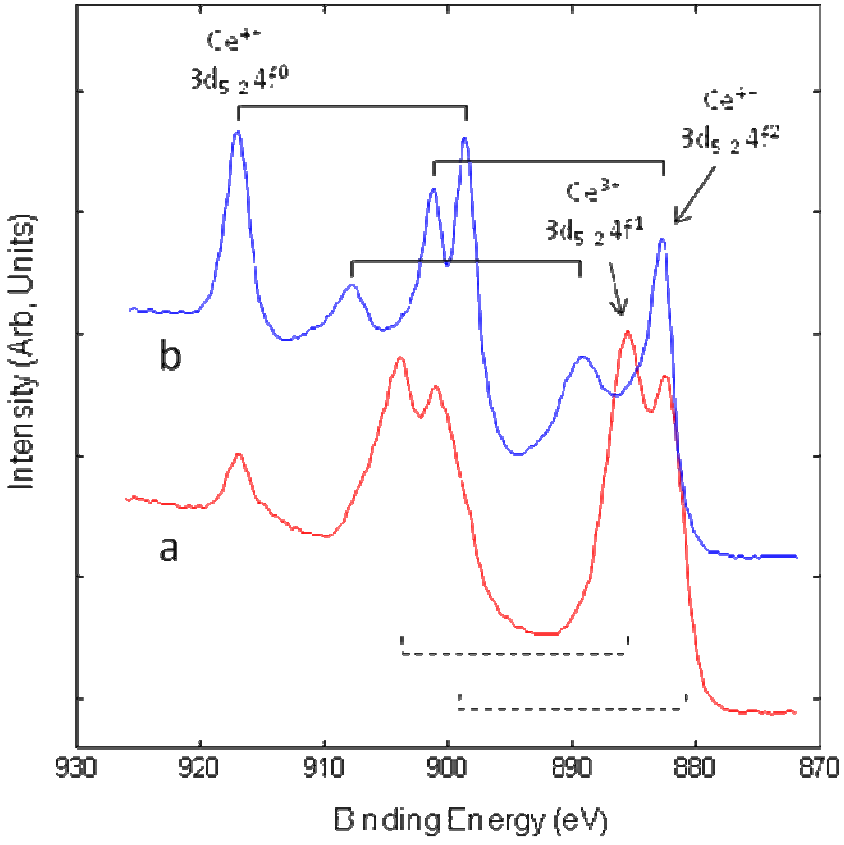

Figure 2-23. XPS high energy resolution photoemission spectra of the Ce 3d region. (a) Tee-mixer , (b) Batch mixer. The brackets in the figure 5 show the spin orbital pairs (5/2) and 3/2) for Ce^{4+} (solid lines) and Ce^{3+} (bashed lines).

2.8.6 Results Discussion

In this study, both batch mixer and Tee-mixer yielded nanorods. However, fundamental theories of the nanorods formation are still under investigation. Tang et. al., 2005 suggests that the nanorods were formed by rolling of laminar structures during precipitation process. This rolling phenomenon is similar to the formation of carbon nanotubes.

Mai et al. 2005 further tested the oxygen storage behavior with respect to different shapes of ceria. The results from nanorods and nanotubes showed better oxygen storage capacity than nanopolyhedra (which is the same as the bulk material). This indicates that high oxygen storage capacity materials might be designed and obtained by shape-selective synthetic strategy.

As for applications of nanorods, at Oregon State University, this structure allows the possibility of depositing anti-reflective/sub-wavelength structures shown in Figure 2-24. However, manufacturing monodispersed nanoparticles at industrial scale requires large quantities of flow volume. In this case, Tee-mixer will not be sufficient and need to utilize novel approaches. In the next Chapter, a different microchannel approach will be proposed and the challenges of manufacturing such devices will be discussed.

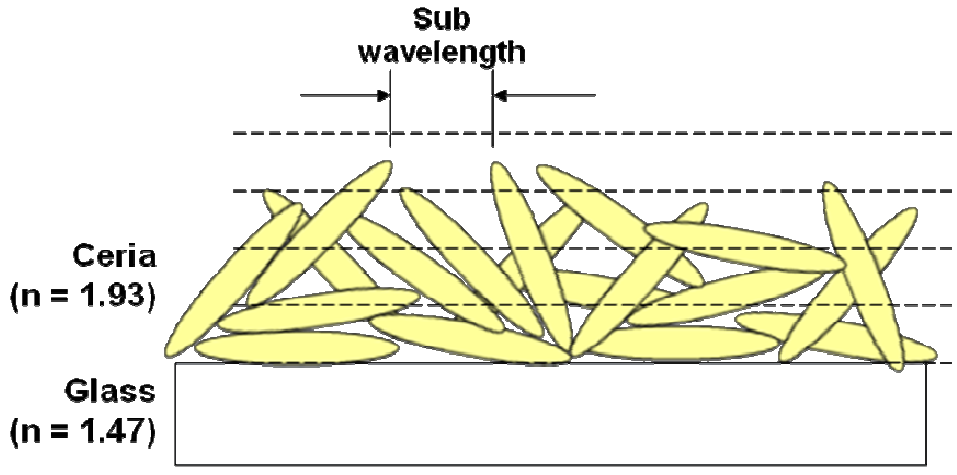

Figure 2-24. Conceptual design of the anti-reflective/sub-wavelength structure using ceria nanorods.

2.9 Summary

Despite having the same composition (XRD results), different nanoparticle morphologies were obtained by changing the mixing approach. This indicates that mixing condition is crucial in ceria precipitation process. XPS study showed that the nanoparticles synthesized using microchannel Tee-mixer yielded more Ce^{3+} molecules. This indicates that the Tee-mixer approach permitted the formation and capture of an unstable intermediate $Ce(OH)_3$ molecule by shielding the intermediate from exposure to the oxygen environment. The SEM images also showed less breakage of the nanorods when deposited.

The results also confirmed that by using the microchannel mixing approach, continuous based nanomanufacturing can be achieved. Applications such as anti-reflective coatings are currently under research.

2.10 Future Work

In this study, Tee-mixer was used to analyze the effect of mixing approaches compared to traditional batch mixing. However, as described in previous section, future work should be emphasized on using novel microchannel setups to increase the flow volume and output.

One issue that needs to be addressed in future work is to analyze the effect of clogging in microchannel devices (Marshall, 2006). Wyss et al., 2006 indicated that microchannel clogging is independent of particle flow rate and volume fraction. Instead, the average number of particles that can pass through before it clogs scales with the ratio of particle size. Future microchannel applications need to consider the size of the nanoparticle which impacts the lifetime of the device.

2.11 Reference

Abi-aad, E., Bechara, R., Grimblot J., Aboukais, A., "Preparation and characterization of ceria under an oxidizing atmosphere. Thermal analysis, XPS, and EPR study," *Chemistry of Materials*, Vol. 5, n 6, pp. 793-797, 1993

Bekyarova, E., Fornasiero, P., Kaspar, J., Graziani, M., "CO oxidation on Pd/CeO_2-ZrO_2 catalysts," *Catalysis Today*, Vol. 45, n 1-4, pp. 179-183, 1998

Chang, C.-H., Liu, S. H., Tennico, Y., Rundel, J.T., Remcho, V. T., Blackwell, E., Tseng, T. and Paul, B. K., "Progress Towards Chip-Based High-Throughput Dendrimer Synthesis," *IMRET8 – 8th International Conference on Microreaction Technology*, Atlanta, GA, pp. 887-888, 2005

Chang, H. Y., Chen H.-I., "Morphological evolution for CeO_2 nanoparticles synthesized by precipitation technique," *Journal of Crystal Growth*, Vol. 283, pp. 457-468, 2005

Chan, E. M., Mathies, R. A., Alivisato, A. P., "Size-controlled growth of CdSe nanocrystals in microfluidic reactors," *Nano Letters*, n 3, pp. 199-201, 2003

Chen, P. L., Chen, I. W., "Reactive Cerium(IV) Oxide Powders by the Homogeneous Precipitation Method," *Journal of the American Ceramic Society*, Vol. 76, n 6, pp. 1577-1583, 1993

Chu, X., Chung, W. I., Schmidt, L. D., "Sintering of sol-gel prepared submicrometer particles studied by transmission electron microscopy," *Journal of the American Ceramic Society*, Vol. 76, n 8, pp. 2115-2118, 1993

Darab, J. G., Buehler, M.F., Linehan, J.C., Matson, D.W., "Nano-crystalline powders and suspensions generated using a flow-through hydrothermal process, part I: Characterization," *Journal of Engineering and Applied Science*, Vol. 346, pp. 499-504, 1994

Darab, J. G., Buehler, M.F., Linehan, J.C., Matson, D.W., "Nano-crystalline powders and suspensions generated using a flow-through hydrothermal process, part II: Applications," *Journal of Engineering and Applied Science*, Vol. 346, pp. 505-510, 1994

Darab, J. G., Neuenschwander, G. G., Elliott, D. C., Frye, J. G., Strauss, J. T., "Production, consolidation, sintering, and stability of novel nano-crystalline zirconia catalyst support powders," *Materials Research Society Symposium – Proceedings*, Vol. 549, pp. 67-72, 1999

Djuricic, B., Pickering, S., "Nanostructured cerium oxide: preparation and properties of weakly-agglomerated powders," *Journal of the European Ceramic Society*, Vol. 19, n 11, pp. 1925-1934, 1999

Dong, X., Hong, G., Yu, D., Yu, D., "Synthesis and properties of cerium oxide nanometer powders by pyrolysis of amorphous citrate," *Journal of Materials Science and Technology*, Vol. 13, n 2, pp. 113-116, 1997

Hakuta, Y., Onai, S., Terayama, H., Adschiri, T., Arai, K., "Production of ultra-fine ceria particles by hydrothermal synthesis under supercritical conditions," *Journal of Materials Science Letters*, Vol. 17, n 14, pp. 1211-1213, 1998

Hirta, Y., Harada, A., Wang, X. H., "Wet forming and sintering behavior of nanometer-sized ceria powder," *Ceramics International*, Vol. 31, n 7, pp. 1007-1013, 2005

Hsu, W. P., Ronnquist, L., Matijevic, E., "Preparation and Properties of Monodispersed Colloidal Particles of Lanthanide Compounds. 2. Cerium(IV)," *Langmuir*, Vol. 4, n 1, pp. 31-37, 1988

Izu, N., Shin, W., Murayama, N., Kanaki, S., "Resistive oxygen gas sensors based on CeO_2 fine powder prepared using mist pyrolysis," *Sensors and Actuators, B: Chemical*, Vol. 87, n 1, pp. 95-98, 2002

Jonathan E. S., Richard D. R., Feng Z., Chan, S. W., Irving P. H., "Size-dependent properties of CeO_{2-y} nanoparticles as studied by Raman scattering," *Physical Review B*, Vol. 64, n 245407, pp. 245407-1 245407-8, 2001

Jones, A. G., *Crystallization Process Systems***,** Oxford: Butterworth-Heinemann, 2002

Kockmann, N., Kastner, J., Woias, P., "Reactive particle precipitation in liquid microchannel flow," *Chemical Engineering Journal*, Vol. 135, n SUPPL. 1, pp. S110-S116, 2007

Krishnadasan, S., Tovilla, J., Vilar, R., deMello, A. J., and deMello, J. C., "On-line analysis of CdSe nanoparticle formation in a continuous flow chip-based microreactor," *Journal of Materials Chemistry*, n 14, pp. 2655-2660, 2004

Mai, H. -X., Sun, L. –D., Zhang, Y. –W., Si, R., Feng, W., Zhang, H. –P., Liu, H. –C., Yan, C. –H., "Shape-selective synthesis and oxygen storage behavior of ceria nanopolyhedra, nanorods, and nanocubes," *Journal of Physical Chemistry B*, Vol. 109, n 51, pp. 24380-24385, 2005

Marshall, J.S., "Particulate aggregate formation and wall adhesion in microchannel flows," *Proceedings of ASME Fluids Engineering Division Summer Meeting 2006*, Vol. 1 SYMPOSIA, pp. 519-526, 2006

Masui, A., Fujiwara, N., Yamamoto, K., Takagi, M., Imanaka, T., "Characterization and catalytic properties of CeO2-ZrO2 ultrafine particles prepared by the microemulsion method," *Journal of Fermentation and Bioengineering*, Vol. 85, n 1, pp. 30-36, 1998

Mullin, J. W., *Crystallization*, 4th edition. Oxford: Butterworth-Heinemann, 2001

Makishima, A., Kubo, H., Wada, K., Kitami, Y., Shimohira, T., "Yellow Coatings Produced on Glasses and Aluminum by the Sol-Gol Process," *Journal of the American Ceramic Society*, Vol. 69, n 6, pp. c.127-c.129, 1986

Nakamura, H., Yamaguchi, Y., Miyazaki, M., Maeda, H., Uehara, M., Mulvaney, P., "Preparation of CdSe nanocrystals in a micro-flow-reactor," *Chemical Communications*, pp. 2844-2845, 2002

Schwarzer, H.-C., Peukert, W., "Tailoring particle size through nanoparticle precipitation," *Chemical Engineering Communications*, Vol. 191, n 4, p. 580-606, 2004

Tang, C., Bando, Y., Liu, B., Golberg, D., "Cerium oxide nanotubes prepared from cerium hydroxide nanotubes," *Advanced Materials*, Vol. 17, n 24, pp. 3005-3009, 2005

Masui, T., Fujiwara, K., Machida, K.-I., and Adachi, G.-Y., "Characterization of Cerium(IV) Oxide Ultrafine Particles Prepared Using Reversed Micelles," *American Chemical Society*, Vol. 9, n 10, pp. 2197-2204, 1997

Ring, T. A., *Fundamentals of Ceramic Powder Processing and Synthesis*, San Diego, CA: Academic Press, 1996.

Tang, C. C., Bando, Y., Liu, B. D., Golberg, D., "Cerium oxide nanotubes prepared from cerium hydroxide nanotubes," Advanced Materials, Vol. 17, n 24, pp. 3005-3009, 2005

Tang, C. C., Bando, Y., Golberg, D., Ma, R. Z., "Cerium phosphate nanotubes: Synthesis, valence state, and optical properties," *Angewandte Chemie - International Edition*, Vol. 44, n 4, pp. 576-579, 2005

Trovarelli, A., de Leitenburg, C., Boaro, M., Dolcetti, G., "Utilization of ceria in industrial catalysis," *Catalysis Today*, Vol. 50, n 2, pp. 353-367, 1999

Tsunekawa, S., Fukuda, T., Kasuya, A., "Blue shift in ultraviolet absorption spectra of monodisperse CeO_{2-x} nanoparticles," *Journal of Applied Physics*, Vol. 87, n 3, pp. 1318-1321, 2000

Tsunekawa, S., Ishikawa, K., Li, Z.-Q., Kawazoe, Y., Kasuya, A., "Origin of anomalous lattice expansion in oxide nanoparticles," *Physical Review Letters*, Vol. 85, n 16, pp. 3440-3443, 2000

Tsunekawa, S., Sahara, R., Kawazoe, Y., Kasuya, A., "Origin of the blue shift in ultraviolet absorption spectra of nanocrystalline CeO_{2-x} particles," *Materials Transactions, JIM*, Vol. 41, n 8, pp. 1104-1107, 2000

Uekawa, N., Ueta, M., Wu, Y. J., Kakegawa, K., "Characterization of CeO_2 fine particles prepared by the homogeneous precipitation method with a mixed solution of ethylene glycol and polyethylene glycol," *Journal of Materials Research*, Vol. 19, n 4, pp. 1087-1092, 2004

Wang, Z. L., Feng, X., "Polyhedral shapes of CeO_2 nanoparticles," *Journal of Physical Chemistry B*, Vol. 107, n 49, pp. 13563-13566, 2003

Weast R. C., *CRC Handbook of Chemistry and Physics*, Boca Raton, FL: CRC Press, Inc. 1984

Wyss, H. M., Blair, D. L., Morris, J. F., Stone, H. A., Weitz, D. A., "Mechanism for clogging of microchannels," *Physical Review E - Statistical, Nonlinear, and Soft Matter Physics*, Vol. 74, n 6, pp. 061402, 2006

Yahiro, H., Baba, Y., Eguchi, K., Arai, H., "High Temperature Fuel Cell With Ceria-Yttria Solid Electrolyte," *Journal of the Electrochemical Society*, Vol. 135, n 8, pp. 2077-2080, 1988

Yamashita, M., Kameyama, K., Yabe, S., Yoshiba, S., Fujishiro, Y., Kawai, T., Sato, T., "Synthesis and microstructure of calcia doped ceria as UV filters," *Journal of Materials Science*, Vol. 37, n 4, pp. 683-687, 2002

Yen, B. K. H., Stott, N. E., Jensen, K. F., Bawendi, M. G., "A continuous-flow microcapillary reactor for the preparation of a size series of CdSe nanocrystals," *Advanced Materials*, Vol. 15, n 21, pp. 1858-1862, 2003

Zhou, X.-D., Huebner, W., Anderson, H. U., "Room-temperature homogeneous nucleation synthesis and thermal stability of nanometer single crystal CeO_2," *Applied Physics Letters*, Vol. 80, n 20, pp. 3814, 2002

CHAPTER 3

Warpage Mechanisms of Microchannel Devices during Diffusion Bonding Process: A Review

3.1 Abstract

Micro Energy and Chemical Systems (MECS) are arrayed microfluidic systems that process mass and energy using the accelerated heat and mass transfer available in microchannels. MECS applications generally involve processing bulk mass and energy. This requires “scaling-up” microchannels thus additional headers and support structures need to be implemented. However, these structural complexities can lead to poor stress distributions during bonding within the device causing either structural failure or device leakage. This review is to categorize each defect modes and provide information to avoid such failure.

3.2 Introduction

In this Section, an arrayed microfluidic system (Micro Energy and Chemical Systems) is introduced. Detailed descriptions of the advantages and applications are then discussed. Afterwards, the scale-up concept and manufacturing approaches for MECS are summarized. Finally, the defect modes and causes during device manufacturing are listed.

3.2.1 Micro Energy and Chemical Systems (MECS)

Micro Energy and Chemical Systems (MECS) are arrayed microfluidic systems that process mass and energy using the accelerated heat and mass transfer afforded by in microchannels. In one hundred micrometer-scale channels, heat and mass transfer take place over significantly shorter diffusional distances than in macro-scale channels. The relationship between the amount of time fluid molecules need to stay in a channel to be processed (i.e. mix or react or transfer heat) and the microchannel hydraulic diameter is by a squared term (Chao et al. 2005; Ehrfeld et al., 2000). This suggests that a 10X reduction in channel diameter requires a 100X reduction in average residence time. Shorter residence time permits shorter channels effectively reducing the overall size of the system. Reduction in system dimensions enables the distributed and portable processing of mass and energy e.g. smaller heat exchangers. Microchannels in MECS devices are typically on the order of 25 to 250 micrometers (µm). Dimensional features within these microchannels may extend well below 25µm including, for example, contactor membrane pores below 5µm (Tseng and Paul, 2003), or catalyst/anti-reflective coating nanoparticles that are as small as 20 nanometers (nm) (Chan, et al., 2003; Tseng and Paul, 2007).

While internal features may extend downward, the overall size of MECS devices are on the order of 1 to 100 centimeters (cm). MECS applications involve the bulk processing of mass and energy requiring the arraying of microchannels. A typical practice to increase the output volume is to scale-up the design by numbering-up, i.e. by adding more channels. The size of the device and the number of channels differentiates MECS from other microfluidic devices such as micro total analysis systems (µ-TAS). Figure 3-1 shows the breadth of application of microfluidic devices.

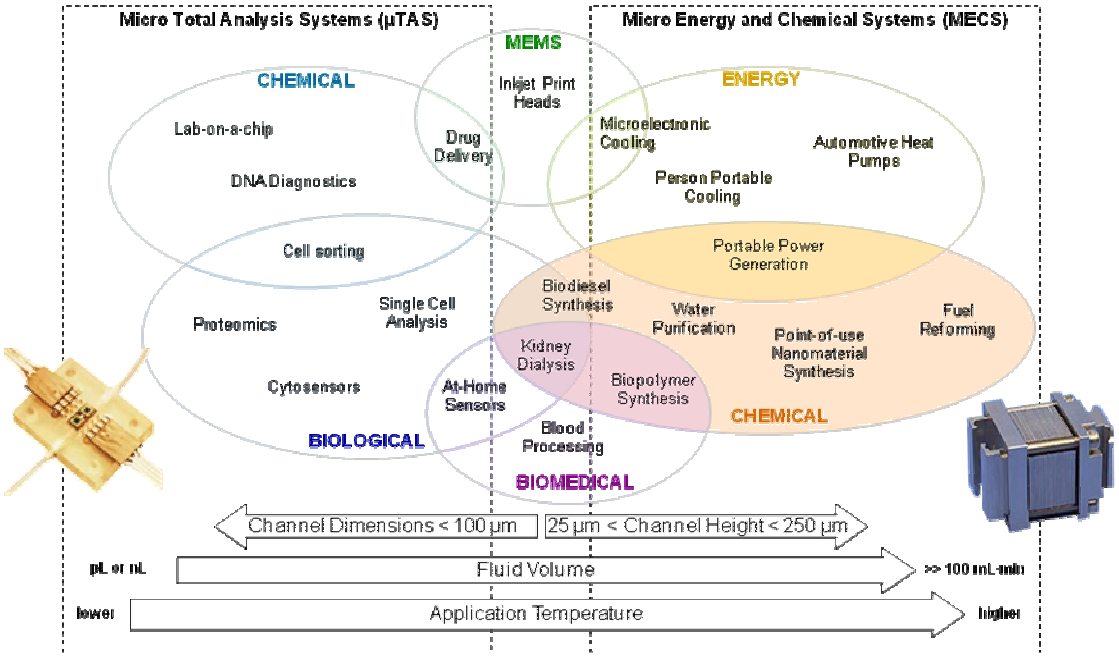

Figure 3-1. Classification of Microfluidic Devices.

Distributed MECS systems are expected to be produced in high volumes at relatively low cost following similar advancements made in manufacture of Integrated Circuits (IC) and Micro Electro-Mechanical Systems (MEMS). IC and MEMS manufacturing rely heavily on silicon-based processing where submicron features are routinely implemented in production. However, the microfluidic components in MECS generally do not require the extremely small feature sizes available by silicon bulk micromachining (although nanotechnology could be employed in the deposition of engineered catalysts on the walls of microchannels). Furthermore, for many MECS applications, silicon is not the favored base material (Peterson, 1998 and 1999). It is more expensive than most other materials and the thermal conductivity is not suitable for many energy-based applications. In addition, polysilicon wafers are brittle and may not be compatible with specific environmental conditions. In contrast, the functionality of MECS typically requires having thermal, chemical and physical properties of more traditional engineering materials such as metals and ceramics. These materials are easier to machine and can be handled without requiring a clean

room. These advantages increase the possibilities of patterning and bonding of the materials to create MECS devices.

3.2.2 Scale-up of MECS Devices

To process bulk mass and energy, MECS devices require arrays of channels. The process of scaling-up microchannel devices is called “numbering-up”. One way to number-up is illustrated in Figure 3-2. Arrays of channels can be laid out on individual layers or laminae. The laminae can then be stacked and bonded together to form devices which can be banked together to further increase the volume of fluid processed in microchannels.

One of the critical components in arrayed microchannels involves the distribution of flow between devices. Headers are plenums of fluid before and after device, laminae and channel arrays used to distribute flow. Channel headers are typically used on laminae to distribute flow between channels. These channel headers can complicate the fabrication process. Headers typically involve large channel spans requiring structural support as bonding pressure is applied. These structural complexities can lead to poor stress distributions within the stack causing either structural failure (e.g. channel warpage/deflection) due to overcompression or device leakage due to undercompression (Schubert et al., 2001). Paul et al., 2006 used finite element analysis (FEA) software and empirical data to investigate the manufacturability limits of two-fluid counter-flow heat exchanger microchannel arrays. It was demonstrated that leakage between laminae is related to the aspect-ratio of channel headers. Thus careful consideration must be made to these factors during the scale-up process to prevent structural failure.

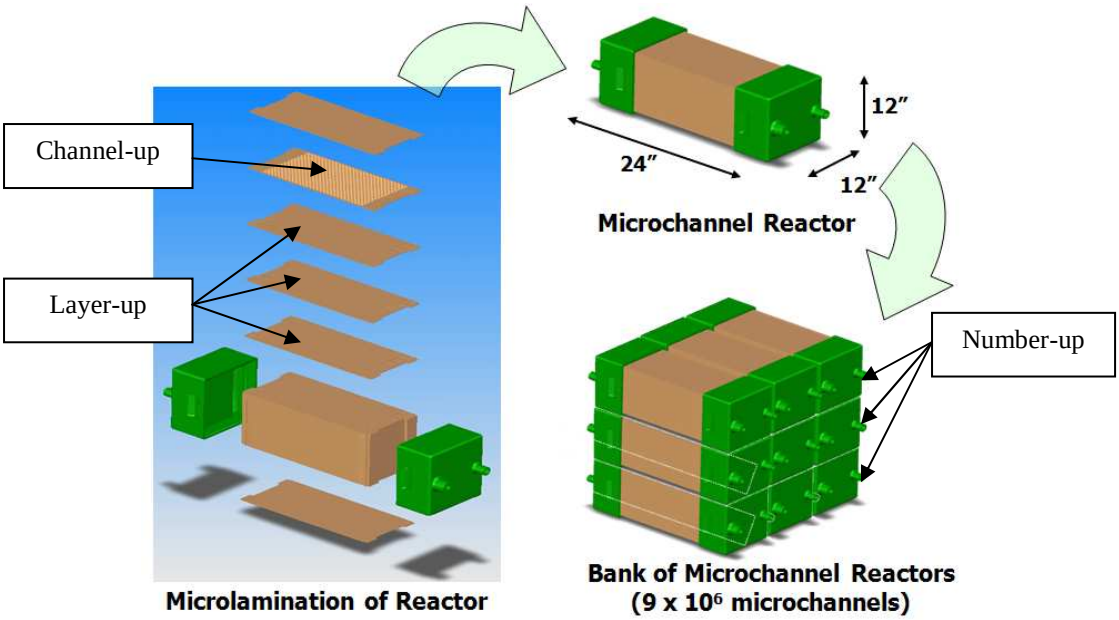

Figure 3-2. Typical scale-up procedure by layer-up, channel-up, and number-up.

3.2.3 Microlamination

Microlamination is one of the major fabrication architectures adapted for numbering-up microchannels (Martin, et al., 1999; Matson, et al., 1998; Paul, et al., 1999; Peterson, 2001). Thin layers of material, called laminae, are patterned with channel arrays and then bonded together into a monolithic device. In general, the process used for microlamination involves three major steps: 1) laminae patterning, 2) laminae registration, and 3) laminae bonding. Figure 3-3 shows an exploded view of a typical microchannel array design, which can be used for bulk heat and mass transfer applications (Ehrfeld, et al., 2001). Laminae patterning can be done by using laser micromachining, etching, lithography, etc. Laminae registration can be done by pin alignment, edge register, or thermally-enhanced edge registration (TEER) (Wattanutchariya and Paul 2004). The bonding step can be carried out by adhesive, reflow (surface mount technology), laser welding, diffusion bonding, etc. In particular, diffusion bonding is generally done in a vacuum hot press that provides uni-axial

compressive pressure under vacuum at elevated temperature to facilitate diffusion bonding. A typical bonding setup is shown in Figure 3-4. Other than benefiting from the accelerated heat and mass transfer, this microlamination approach also provides versatility of adapting different application requirements such as increasing the overall throughput.

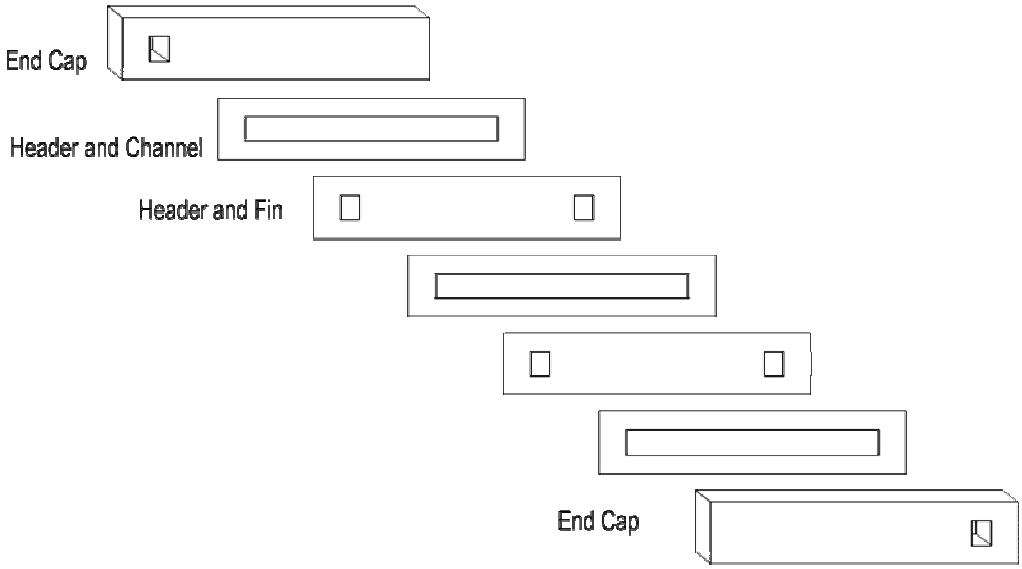

Figure 3-3. An exploded view of a MECS device design illustrating microlamination concept.

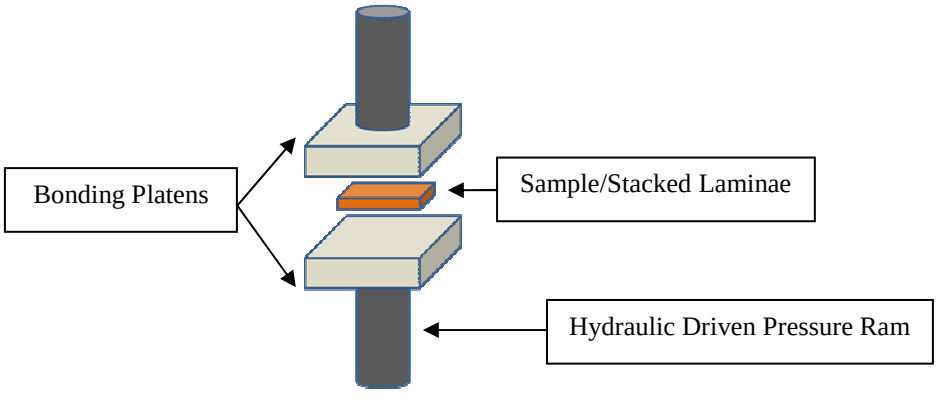

Figure 3-4. Typical diffusion bonding setup.

3.2.4 Flow Maldistribution in Microreactors

Arrayed microchannel designs are usually based on the assumption of perfect geometry so that the flow rates between individual channels/layers/devices are equivalent. However, during micromachining, microchannel dimensions sometimes deviate from design due to either tool resolution or characteristics of tool finish. These variations in channel dimension can cause maldistribution of the flow with serious degeneration of the efficiency of the microfluidic system. For example, in heat exchange applications, larger cross section channels have greater volumetric flow rates and longer conduction paths for heat transfer to or from the walls of the channel. This results in less effective heat transfer for the total surface area of the microfluidic system. Wattanutchariya and Paul, 2002 further identified that channel variation of 20% in heat exchanger channels could result in a 50% increase in the number of channels needed to process the same volumetric flow.

Currently, four main sources of flow maldistribution have been identified. The first is fouling caused by physical blockage occurring within the channel that can be caused by accumulating debris or precipitation of reactants. The second is two-phase flow in multiple phase systems that have highly inconsistent flow patterns due to high and low pressure areas associated with different phases (usually gas and liquids). The third is self-induced maldistribution that is related to changes in viscosity between channels due to heat transfer, phase changes, etc. The fourth source is mechanically induced warpage. This is typically caused by defects such as variation in channel design, fittings, channel shape, and side wall conditions (surface roughness) during manufacturing. In most cases, the first three sources can be minimized by appropriate selection of the application. The focus of this review is on the fourth category and will address mechanically induced warpage leading to maldistribution of flow.

3.2.5 Defect Modes and Causes During Device Manufacturing

As mentioned in the previous paragraphs, maldistribution of fluid flow in microchannel devices could cause a significant drop in efficiency. Mechanically induced maldistributions are typically caused by defects generated during manufacturing. In addition, design and material condition can also contribute to flow maldistribution. In the literature, causes of nonuniformity warpage can include residual stresses that are relaxed during bonding, initial curvature of shim stock, mismatch of coefficient of thermal expansion of composite material, and delamination of composite laminae. (Timoshenko, 1961; Shames, 1989; Fang et al., 1994; Gere et al., 1997; Ashby, 1999; Fang et al. 1999; Popov, 1999; Paul et al., 2000; Paul et al., 2000). These defects are listed and linked with possible causes in Table 3-1. As shown in the table, most of the causes are related to warpage. However, there were no detailed studies analyzing the relationship between each individual cause and warpage found in current literature.

Table 3-1. Defect modes and causes for microchannel devices.

		Causes							
		Design	Material Condition		Fabrication				
		Unsupported Regions	Internal Stress	Crease	Mis-registration	Thermal Gradients	Poisson's Effect	Creep	Burrs
Defect Mode	Channel Thinning	△						○	
	Warpage	○	○	○	○	○	○	△	○
	Poor Bonding	○		○					○
	Misalign				○				
	Void			○					○

* Circle represents direct cause and triangle represents indirect cause

In the subsequent sections, detailed literature review related to individual cause have been listed. In addition, some of the causes were validated through experiment.

3.3 Design: Unsupported Regions

Warpage within arrayed microchannel devices can be the result of poor stress distribution during operation and bonding. Schubert, et al., 2001 noted that the lack of structural support in microchannel designs can result in the collapse of microchannels during operation. We have observed the collapse of channels during bonding due to unsupported regions (shown in Figure 3-5). Poor stress distribution due to unsupported spans is less likely to occur in small test articles where spans are minimal. In larger devices used to scale-up arrayed microfluidic applications, complex header structures in each lamina can lead to large unsupported spans.

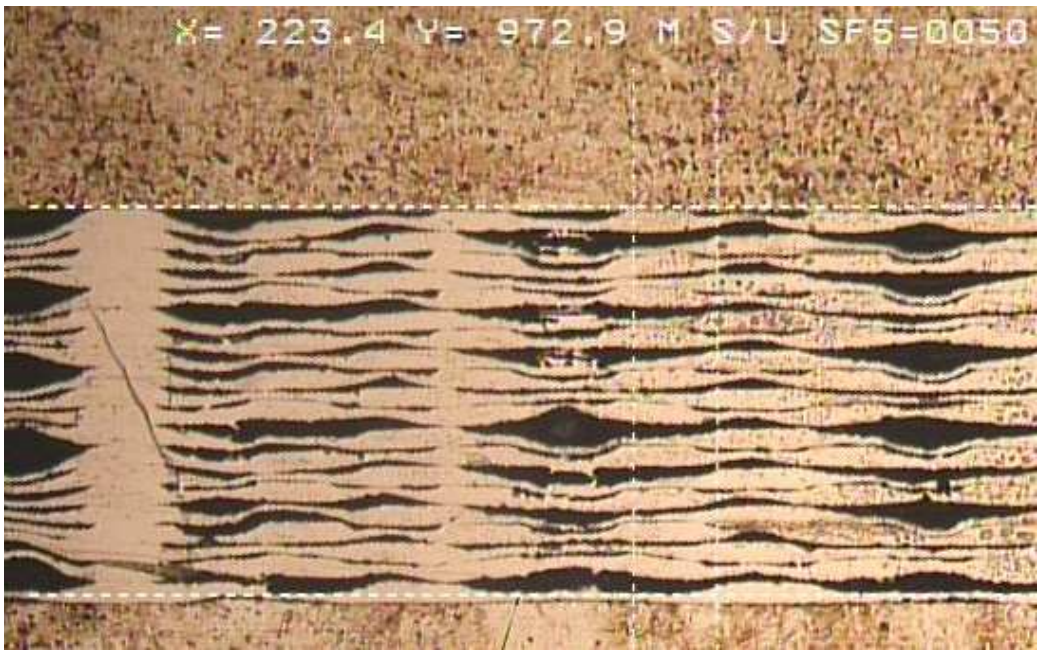

Figure 3-5. A cross-sectional view of collapsed stainless-steel microchannel structures (Tseng et al. 2008) taken from optical microscope (50X).

To aid the designer in minimizing unsupported regions, FEA software can be used to simulate the structural behavior under compressive stress during the diffusion bonding process. By using such software, Paul et al. 2006 successfully analyzed the

design limits on aspect ratios in counterflow microchannel arrays and the results were matched with empirical data. Findings showed that poor bonding regions were predicted in regions of loaded test articles where the stress distribution approached the tensile/compressive boundary. Zhou et al. 2007 also used FEA software to analyze the viscoelastic deflection and stresses of microchannel structures when subjected to internal (operating) pressure. FEA analysis can facilitate a better understanding of design limitations of arrayed microchannel components both during fabrication and operation.

3.4 Material Condition: Internal Stress

Microlamination technology relies on the patterning, registration, and bonding of thin shim stock manufactured from traditional cold rolling processes. During the cold rolling process, internal stresses can accumulate due to cold work. While machining thin shim stock, relaxation of internal stresses may cause considerable warpage. In addition, during subsequent steps of microlamination, additional residual stresses can be introduced causing similar defects. Figure 3-6 shows warpage due to thermal stresses induced by laser micromachining.

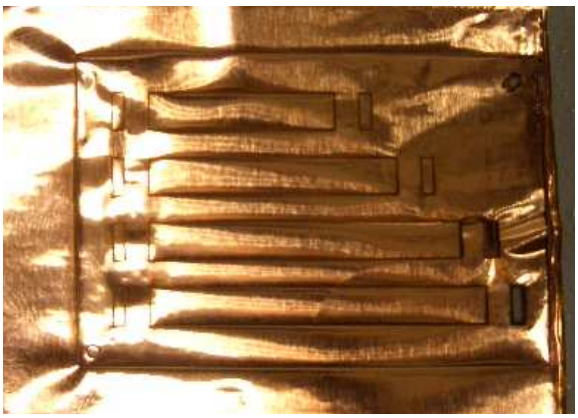

Figure 3-6. Result of induced warpage due to laser machining on copper shim stocks.

To avoid warpage due to internal stresses, it is suggested that the starting material be annealed and flattened. Annealing is a procedure in which the material is held at high temperature for sufficient time to relieve internal stresses. The cooling process is controlled to reduce thermal stresses minimizing reintroduction of internal stresses. Typical recipes for annealing different materials can be found in ASM Handbooks and Metals Handbooks (ASM Handbook v2; ASM Handbook v4; Davis, 1998). Flattening is typically done at elevated temperatures to reduce the yield strength of the material. As an example, pure coppers can be flattened with excellent results at around 450ºC.

3.5 Material Condition: Crease

Creases are permanent identations that extend through the thickness of a lamina. Creases are generally introduced during handling or patterning and may be located randomly throughout the lamina. Creases prevent intimate contact locally between laminae during diffusion bonding resulting in voids within the device. Voids on the bondline can cause leakage issues or delamination as shown in Figure 3-7.

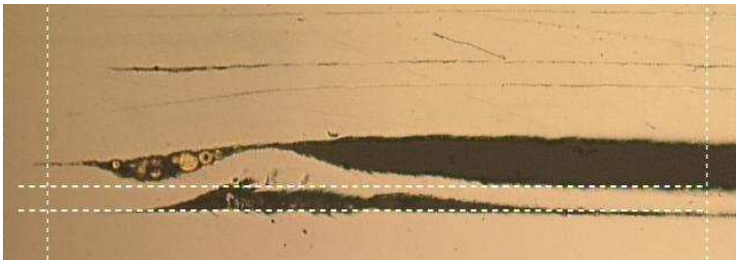

Figure 3-7. Crease induced void in microchannel structures.

To avoid this type of failure, handling procedures must be developed to minimize the occurrence of crease defects. One efficient way to improve handling is by using a vacuum wand (purchased from H-Square shown in Figure 3-8). Further, rigorous lamina inspection is needed to detect the crease before proceeding with subsequent processes.

Figure 3-8. Vacuum wand currently used at OSU (purchased from H-Square).

3.6 Fabrication: Misregistration

Registration can be a critical step in a microlamination architecture. While the reduction of contact surface area between counteflow channels due to misregistration has been found to be insignificant on the impact the effectiveness of microchannel heat exchangers (Wattanutchariya and Paul 2004), misregistration can cause deviations from the original design that reduce structural stability. For example, stress risers can develop during bonding due to the misregistration of laminae. In one of the microchannel devices designed in the lab, FEA showed that when stacked laminae were compressed under 1000 psi, the maximum von Mises[1] stress in the registered stack was 8,160 psi while a stress of 10,990 psi was observed in the misregistered stack (shown in Figure 3-9). This 34% increase of von Mises stress was induced by only 10% misregistration. According to the definition, when von Mises stress exceeds

[1] The von Mises stress is a yield criterion typically used in material mechanical studies. It predicts the stress state of materials under a particular loading condition from results of simple uniaxial tensile stresses.

the yield stress of the material, the structure would fail which would result in deformation of the microchannel structures.

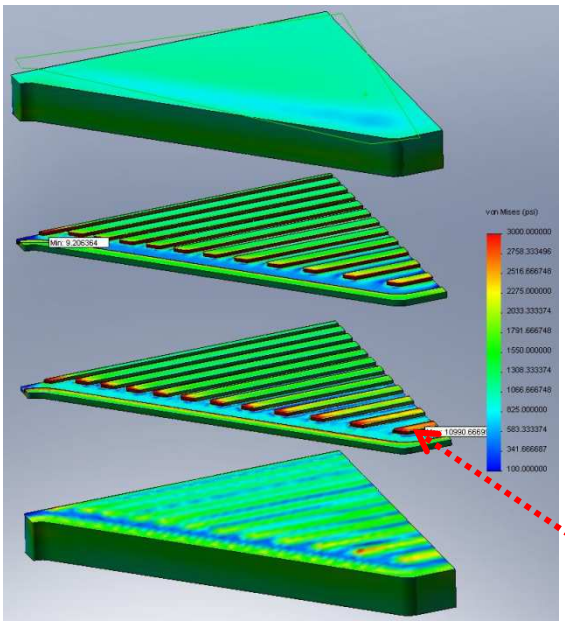

Figure 3-9. Von Mises stress model of the mis-registered laminae under compressive force.

3.6.1 Theoretical Hypothesis

To isolate the defect mode caused by mis-registration, a simple model was developed as shown in Figure 3-10 (a). When a stack is mis-registered as shown in Figure 3-10 (b), bending moments are generated due to excessive force being applied on the top and bottom lamina.

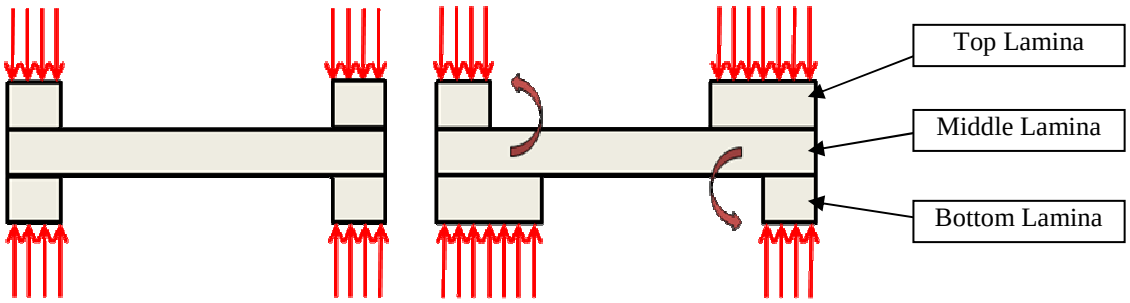

(a) (b)

Figure 3-10. Conceptual diagram of a 3 layer microchannel device design with (a) good registration and (b) mis-registration.

This model can be simplified by considering the free body diagram of only half of the structure shown in Figure 3-10 (b). The new schematic is shown in Figure 3-11.

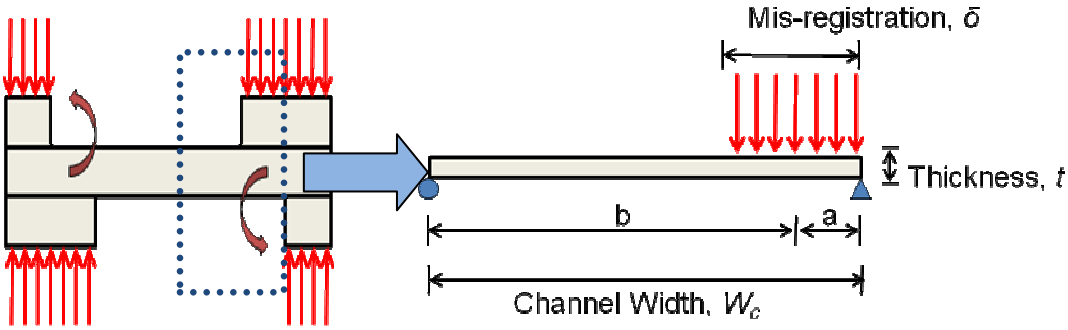

Figure 3-11. Simplified diagram of the mis-registration warpage.

Assuming the mis-registration load is uniformly distributed, loading can be converted to a point load at half the distance of the total mis-registration distance. By using the level rule (Hibbeler 2005; Ugural 2008; Hearn, 1985), the point load can be represented as

$$\frac{F \cdot b}{W_c} \tag{3-1}$$

where

F = Mis-registration force (from compressive pressure)

b = Distance from mis-registration load to the center of the channel

W_c = Width of the microchannel

Since the mis-registration force was distributed from the compressive pressure, it can be represented by

$$F = P \cdot A = P \cdot (2a \cdot L_c) \tag{3-2}$$

where

P = Compressive/Bonding pressure

A = Surface area of mis-registration load being applied

a = Distance from mis-registration load to the edge of the microchannel

L_c = Length of the microchannel

From literature, the critical bending moment for a thin plate can be represented as

$$\frac{\sigma_y \cdot L_c \cdot t^2}{6} \tag{3-3}$$

where

σ_y = Yield strangth of material

t = Thickness of the lamina

Thus by assuming $b = W_c - a$, the moment generated from the point load (caused by mis-registration) can be compared with the critical bending moment yielding:

$$\frac{P \cdot (2a \cdot L_c) \cdot (W_c - a)}{W_c} \cdot a = \frac{\sigma_y \cdot L_c \cdot t^2}{6} \tag{3-4}$$

where a is the distance from the point load to the fixed edge. The formula from (3-4) can then be rewritten as

$$2P(a)^3 - 2PW_c(a)^2 + \frac{1}{6}W_c\frac{\sigma_y}{6}t^2 = 0 \tag{3-5}$$

Since L_c is on both side of the equation, it cancels. Thus by solving the equation for a (Please see Appendix C), the distance of maximum mis-registration can be calculated with given structural geometries (W_c and t) and mechanical property (σ_y) under compressive pressure (P). Though the equation can be solved having three solutions, two of them would always be negative value leaving the last solution a positive value (which is the mis-registration distance).

3.6.2 Material

For this experiment, copper alloy 11000 (McMaster-Carr #9709K54) was selected due to its micromanufacturability and mechanical properties at room temperature. This copper alloy has relatively low yield strength (302 megapascal) allowing for good sensitivity to poor stress distributions. Also, its mechanical properties at bonding temperature are low (Davis, 1998 and Templin, et al., 1948). Consequently, if the material is subjected to thermal/mechanical stress damage during laser machining, it can be easily flattened compared with other metals such as stainless steel or nickel.

Bonding platens (described in 3.2.2) for transmitting compressive pressure during bonding were made of alumina and were purchased from CoorsTek (material number AD-995). The alumina platens were 2 inches long by 2 inches wide by 0.5 inch thick, and were double-side ground to hold flatness and parallelism to less than 12.7 µm over the whole surface. The peak-to-valley surface roughness (R_{max}) was 0.762 µm while the average surface roughness is about 0.19 µm.

3.6.3 Preliminary Test Coupon Design

To verify the mathematical model, a preliminary test coupon was designed (shown in Figure 3-12). For detailed specifications and dimensions, please refer to the engineering package in Appendix F. This test coupon consisted of three laminae. The dimension for each lamina was 2 inches long by 2 inch wide by 0.002 inch thick (actual surface area of 1.887 inch^2). The bottom lamina in this design was patterned to provide a gradient amount of misregistration from the top lamina. Each test coupon incorporates three different channel widths having 375, 500, and 750 µm. With each channel width, several different mis-registration lengths were tested (Figure 3-12b). Table 3-1 lists all the channel widths and mis-registration lengths embedded in the test coupon design.

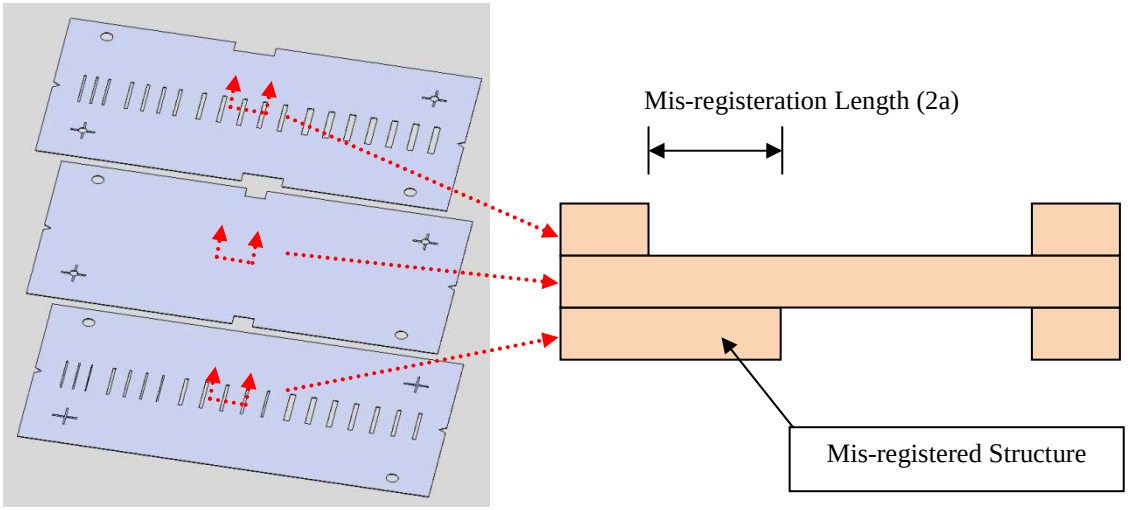

(a) (b)

Figure 3-12. Top view (a) and cross-sectional side view (b) of the test coupon design.

Table 3-2. Structural dimensions incorporated in the test coupon design.

Mechanical Property		Structural Properties			
Yield Strength (σ_y)		Channel Width (W_c)	Thickness (t)	Mis-registration Length (2a)	Mis-registration Percentage
MPa	psi	mm	mm	mm	%
14.38	2085.00	0.375	0.061	0.050	13%
		0.375	0.061	0.100	27%
		0.375	0.061	0.150	40%
		0.375	0.061	0.200	53%
		0.500	0.061	0.050	10%
		0.500	0.061	0.100	20%
		0.500	0.061	0.150	30%
		0.500	0.061	0.200	40%
		0.500	0.061	0.250	50%
		0.750	0.061	0.050	7%
		0.750	0.061	0.100	13%
		0.750	0.061	0.150	20%
		0.750	0.061	0.200	27%
		0.750	0.061	0.250	33%
		0.750	0.061	0.300	40%
		0.750	0.061	0.350	47%

Since the misregistration distance is critical in this experiment, methods were developed for measuring and controlling the registration between laminae. To register the position of the stacked test coupons, 1/16 inch registration pins were used. The registration dowel pins were purchased from McMaster-Carr (#97395A405) with both ends pre-tapered to allow easy insertion into the registration pin holes. To validate that the registration pins were properly registering the stacked laminae, fiducials were implemented that can be checked during assembly. For details of the fiducial design, please refer to Appendix G.

3.6.4 Experimental Process Plan

3.6.4.1 Patterning

To manufacture the test coupons, a laser µVia drilling machine was used (ESI model 5330). This laser system is a pulsed Nd:YAG laser which operates at 355 nm wavelength and can output > 5.7 Watts at 30 kHz. The accuracy of the laser is ± 20 µm over 533 mm by 635 mm. In addition, the maximum velocity for this laser machine is 500 mm/sec so it makes this process a fast and efficient way for prototyping samples with through cut designs (Matson, et al., 1998; Martin, et al., 1999). The parameters used for the fabrication of the test coupons were optimized to minimize thermal stress during laser machining. The consequence of using non-optimized parameters is shown in Figure 3-13. The optimized parameters are listed in Table 3-3. There are two sets of parameters listed in the table because the fiducial markings require reduction of laser power.

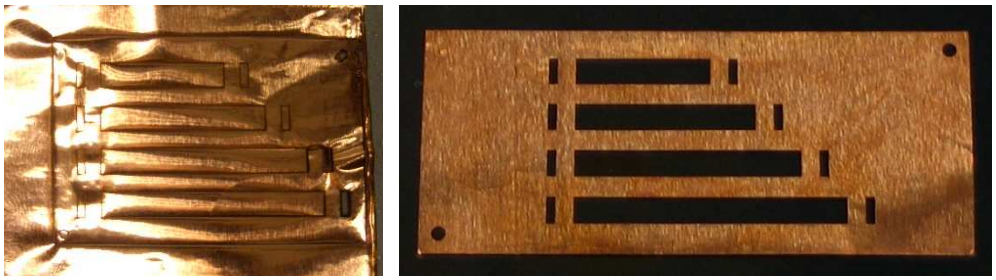

(a) (b)

Figure 3-13. Images of laser machining results using (a) non-optimized and (b) optimized parameters.

Table 3-3. Laser machining parameters for through cuts and blind cuts.

		2 mil Copper			
		Through Cut		Blind Cut	
		1st Pass	2nd Pass	1st Pass	2nd Pass
Z-offset	(mm)	-0.015	-0.025	-0.015	-0.025
Speed	(mm/sec)	90	90	90	90
Rep. Rate	(kHz)	30	30	30	30
Power	(Watts)	5.85	5.85	1.8	1.8

3.6.4.2 Flattening and Annealing

Though the optimized parameters were used, the test coupons still needed a flattening and annealing cycle. The recipe was referenced from ASTM standards (Davis, 1998 and Templin, et al., 1948). The purpose of the flattening and annealing step was to remove thermal stresses and edge burrs created during laser machining. The burrs created from laser machining are typically between 15 to 35 µm and can be flattened to below 1.5 µm (shown in Figure 3-14). This annealing step also removes any warpage caused by handling.

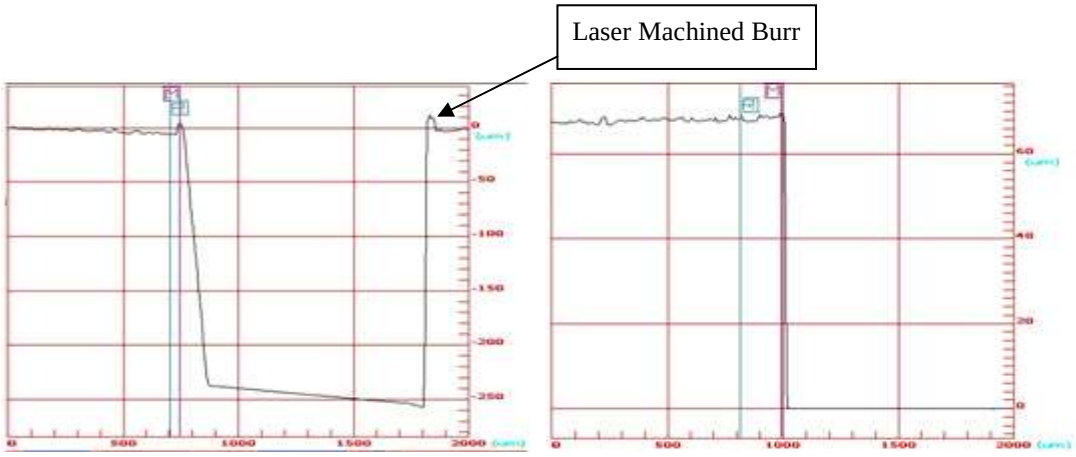

Figure 3-14. Laser machined burrs before (a) and after (b) flattening/annealing.

3.6.5 Preliminary Test Protocol

To verify the warpage due to misregistration, the test coupon was uniformly compressed in order to simulate actual process conditions during diffusion bonding. Bonding pressure was applied to platens using a hydraulic press (Pressmaster model HP30-4560 from Thermal Technologies Inc.). This press has a three inch inside diameter chamber sufficient to accommodate the test setup used. Process conditions used in this experiment mimicked diffusion bonding parameters. The test coupon was heated to 450°C and then compressed using a load of 14.38 MPa (2085 psi). The static load was continuously applied for 30 minutes. Usually the length of time for applying compressive bonding pressure is between 1 to 24 hours. However in this study, the shorter amount of time prevents the test coupon from developing creep phenomenon (which will be explained in 3.9).

After pressing, the test coupon was potted in epoxy and subjected to a standardized metallography process to inspect for the warpage of the microchannels.

3.6.6 Preliminary Results and Discussion

The cross-sectional view of the microchannel can be imaged (shown in Figure 3-15, Figure 3-16, and Figure 3-17)

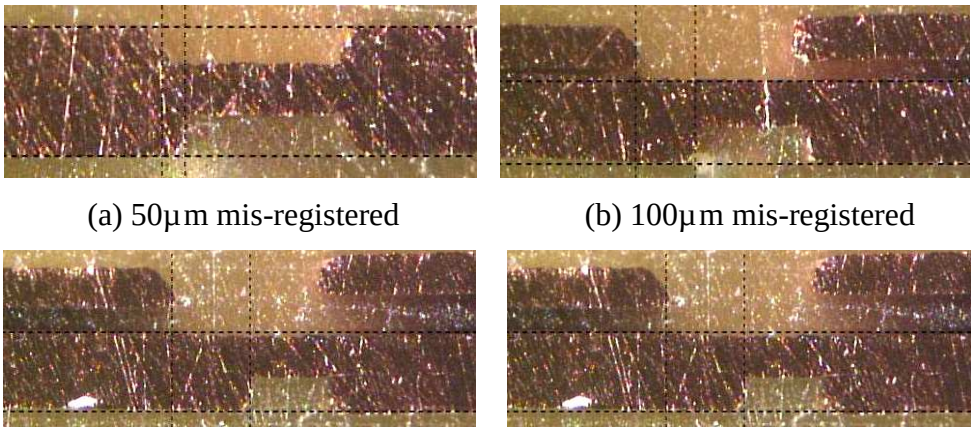

(a) 50µm mis-registered (b) 100µm mis-registered

(c) 150µm mis-registered (d) 200µm mis-registered

Figure 3-15. Cross-sectional view of mis-registered microchannels having channel width of 375µm.

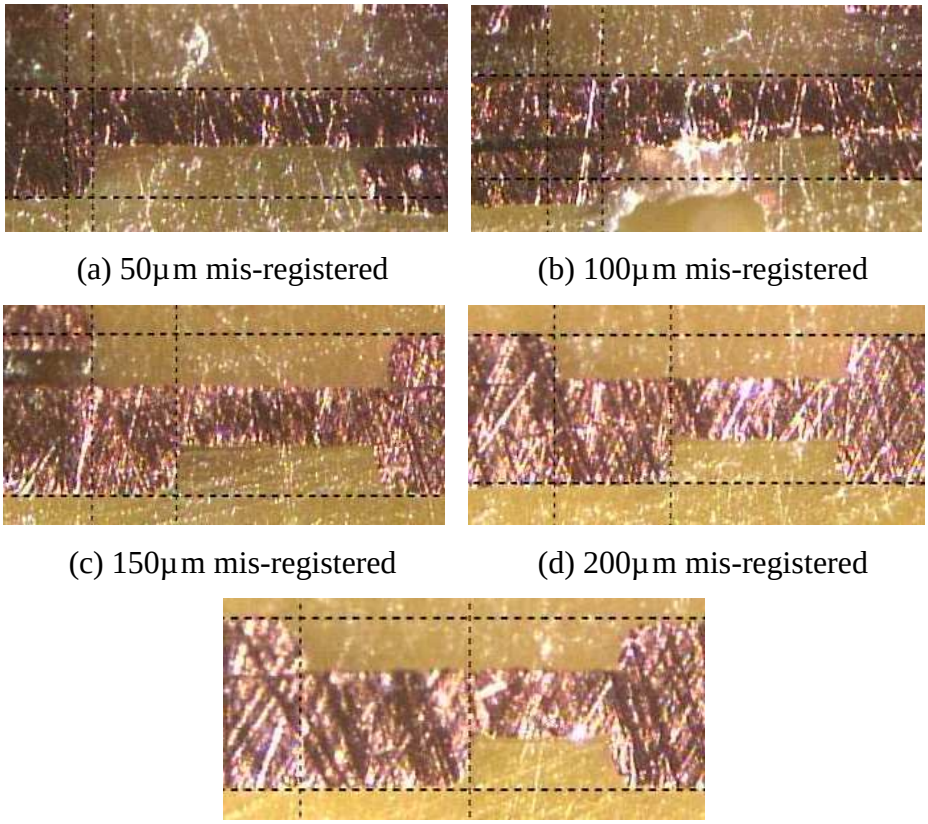

(a) 50µm mis-registered (b) 100µm mis-registered

(c) 150µm mis-registered (d) 200µm mis-registered

(e) 250µm mis-registered

Figure 3-16. Cross-sectional view of the mis-registered microchannels having channel width of 500µm.

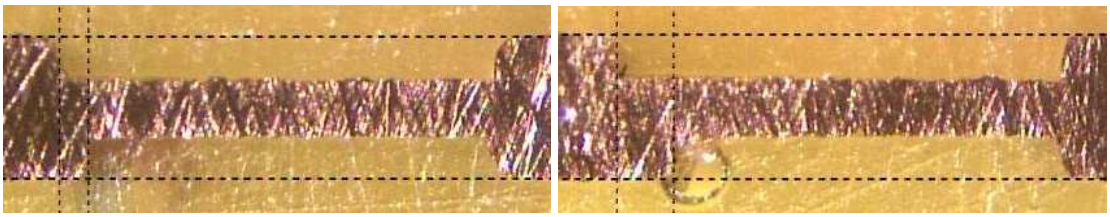

(a) 50µm mis-registered (b) 100µm mis-registered

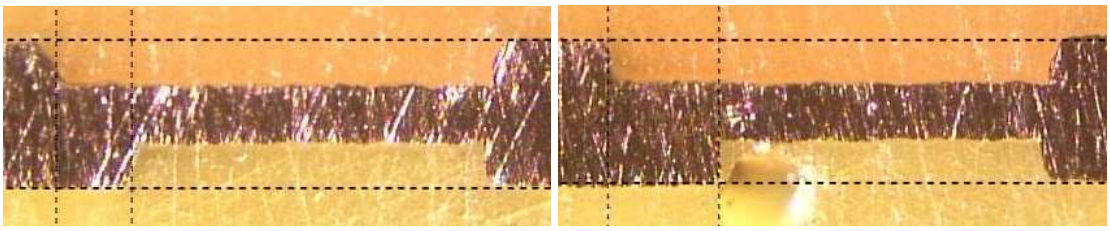

(c) 150µm mis-registered (d) 200µm mis-registered

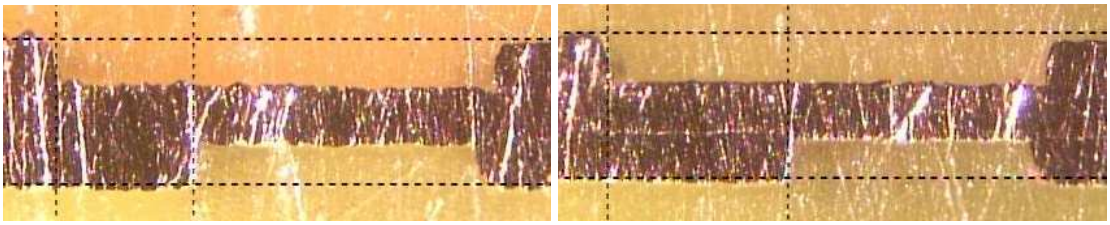

(e) 250µm mis-registered (f) 300µm mis-registered

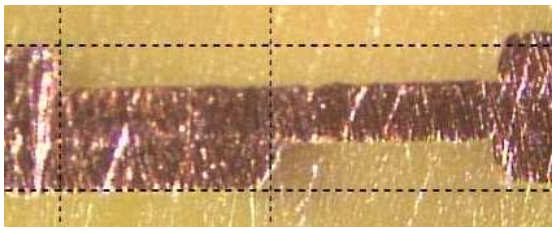

(g) 350µm mis-registered

Figure 3-17. Cross-sectional view of the mis-registered microchannels having channel width of 750µm.

The cross-sectioned samples were inspected and no visible warpage was identified. This suggests that the results do not agree with the formula derived in (3-8). Such deviation might be caused by changes of material's properties at high temperature. Some other effects such as initial curvature of the foil could also cause

issues in obtaining the data. Additional consideration and analyses needs to be done and will be discussed in section 3.6.7.

The results also show that some delaminating of laminae had occurred during the metallography process. This is mainly because of poor bonding between laminae caused by insufficient compression time at bonding temperature. This is a desirable result because this indicates that there was not enough time to induce creep.

The accuracy and repeatability of the registration procedure was also evaluated. As described previously, registration fiducial features were checked before and after the pressure applied. Figure 3-18 shows representative result images of the fiducial markings taken with an optical microscope. Since the fiducial markings line up with each other, less than 10 µm misalignments were achieved using this procedure.

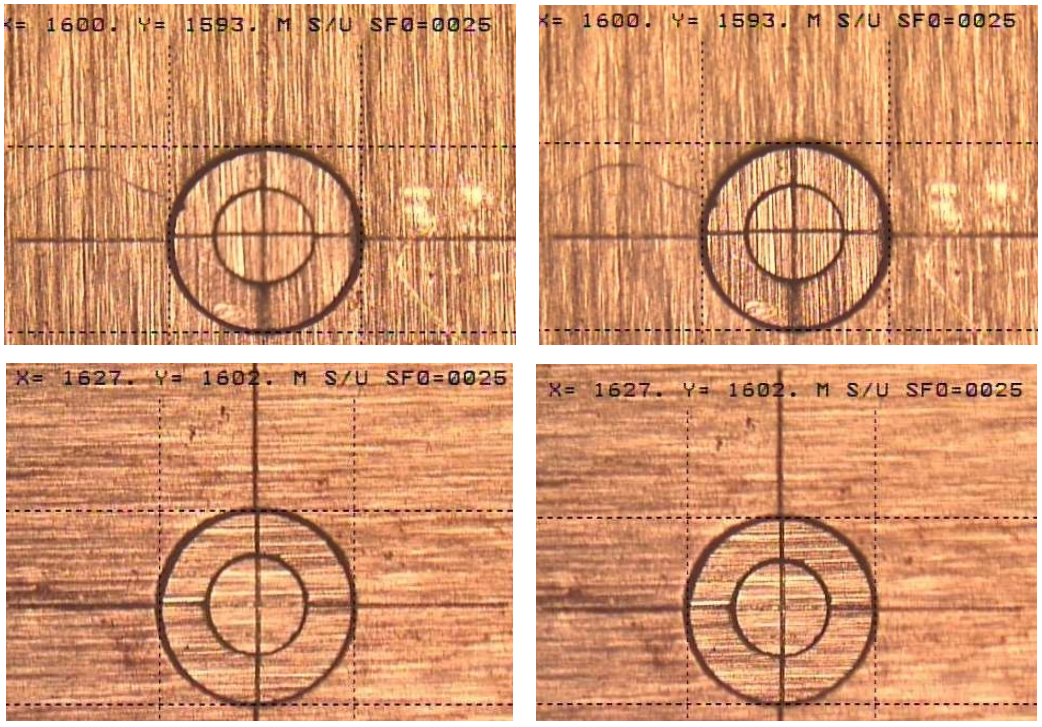

Figure 3-18. Optical images (50X) of the fiducial markings before (on the left) and after (on the right) the diffusion bonding cycle.

3.6.7 Future Work

New models need to be formulated to isolate and test mis-registration caused by warpage. FEA analysis from this study showed that mis-registration would reduce contact surfaces which increase the load (compressive stress) on support structures. When this stress exceeds the yield strength of the material, the microchannel features will be susceptible to warpage. However, actual experiment showed that even with up to 60% mis-registration, no visible warpage was detected. This indicates that the model needs to be adjusted to predict mis-registration warpage. One possible adjustment that can be tested is that instead of applying uniform pressure to the mis-registered area, a non-uniform pressure needs to be simulated. This non-uniform pressure is induced by compressive strain being applied on the stacked laminae. In addition, the distance of the non-uniform pressure load needs to be correlated with the bonding pressure and the mechanical properties of the material.

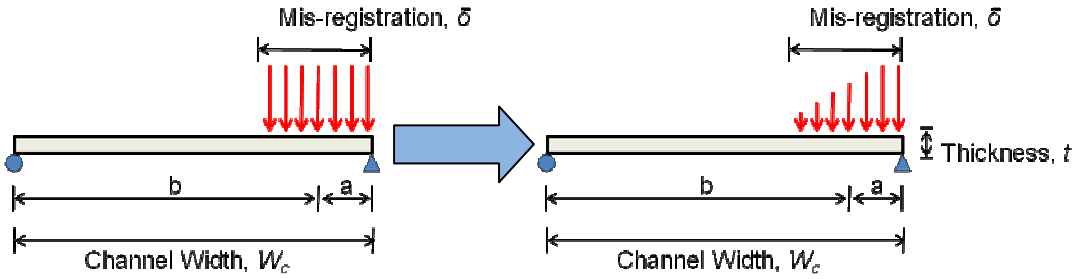

Figure 3-19. Schematics of the uniform (a) and non-uniform (b) distributed load on a mis-registered structure.

3.7 Fabrication: Thermal Gradient

The warpage caused by a thermal gradient is typically due to non-uniform thermal strain throughout the surface. This induces thermal stress and when it exceeds the flexural strength of the lamina, the lamina will be susceptible to bending/buckling. Excellent reviews were found in several sources of mechanics literature (Boley et al., 1960; Nowacki, 1962; Hetnarski, 1986; Kovalenko, 1969). However, these reviews focused mostly on macro scale structures and the boundary conditions used in those studies are not exactly the same as those used in microlamination application. Another consideration is that when the critical feature sizes of the laminae are approaching the size of the grain, the material might behave differently compared to the bulk material. To the best of the author's knowledge, the effect of these thermal gradient induced stresses have not been investigated in devices employing microchannel structures.

For microlamination, thermal gradient stresses are generally created during the last step in the process which is diffusion bonding. This process involves holding two or more components (laminae) under certain load condition at an elevated temperature usually in a protective atmosphere or vacuum. The loads used are typically below those that would cause macro-deformation of parent material(s) and temperature of 0.5 – 0.8 T_m (T_m is the melting temperature) are applied. The holding time at bonding temperature can vary from 10 to 600+ minutes depending on the material being bonded, the joint properties required and the remaining bonding parameters. This thermodynamically enabled process allows solid-state joining of the material(s). Afterwards, the sample is slowly cooled to room temperature. Figure 3-20 shows a typical diffusion bonding temperature and pressure profile. As can be seen, during temperature ramp-up and ramp-down, the laminae will be subjected to gradient thermal energy if the ramp rate are too fast.

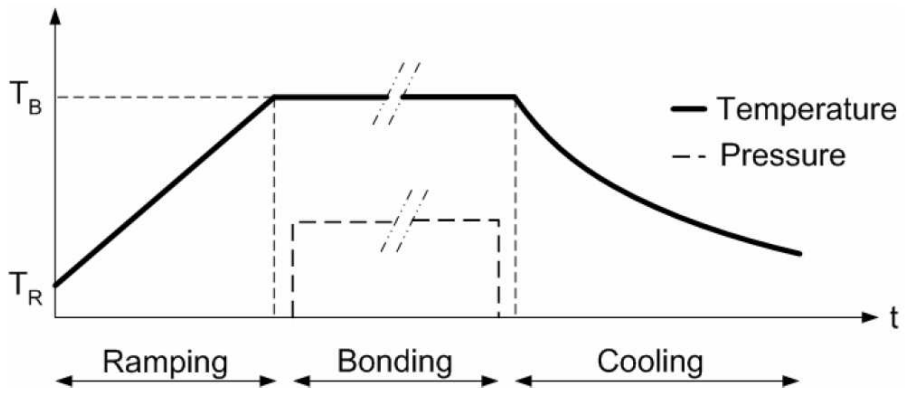

Figure 3-20. General diffusion bonding temperature and pressure profile for microlamination

The effect of thermal gradient could be considered minimum during ramp-up because the laminae are not subjected to compressive pressure and are not yet bonded. In contrast, during cooling cycle, since the laminae are already bonded and are under high vacuum, thermal energy can only be dissipated through radiation (assuming the fixtures have poor conduction properties). This would cause the laminae to start cooling from the outer edge and contract/compress into the center which is still at higher temperature. In addition, it can be observed in Figure 3-20 that the cooling curve is parabolic and asymptotic to the X-axis. In other words, the thermal gradient will be larger when cooling from higher temperatures as opposed to lower temperatures.

Gossard et al., 1952 started analyzing the mechanism of plate buckling induced by spatial temperature gradients which inspired later experiments and research publications (Tauchert, 1991 and Thornton et al., 1994). Boley et al., 1960 proposed a model which relates thermal gradient and plate buckling expressed as

$$\frac{\propto E}{2} T_{cr} = \frac{K\pi^2 E}{12(1-\nu^2)} \left(\frac{h}{b}\right)^2 \tag{3-6}$$

where

α = Coefficient of thermal expansion [µm/m K]

E = Young's modules [N/m^2]

T_{cr} = Critical buckling temperature difference [K]

K = Coefficient for plate buckling

υ = Poisson's ratio

h = plate thickness [m]

b = plate span [m]

In these studies, validation of models was performed by locally heating the center of test plates while clamping/fixing the edges. In contrast, it is expected that thermally-induced warpage of microchannels during diffusion bonding happens during cooling under different thermal and load conditions. Laminae are generally cooled from the outside inward. Diffusion bonding pressure is applied across the stack. Due to the difference in boundary conditions, the formula described in (3-6) is not valid. Below, FEA software (COSMOSWorks) is used to evaluate the thermal behavior of microlaminated stack during diffusion bonding. In addition, an experimental study is presented to confirm the effect of thermal stresses.

3.7.1 COSMOSWorks Analysis

A thermal analysis was done to evaluate the presence of thermal gradients within the microchannel geometry shown in Figure 3-21. Boundary conditions were used to simulate the condition of cooling along the edges of laminae. The cooling rate used in this FEA study was the same as data collected from previous diffusion bonding hot press processes (maximum of 30° Celsius per minute). Results in Figure 3-21 show that a difference of 8° Celsius was observed across a simple 2 inch by 1

inch sample. However, gradients as high as 70°C per centimeter were found in this particular configuration as shown in Figure 3-21 (b).

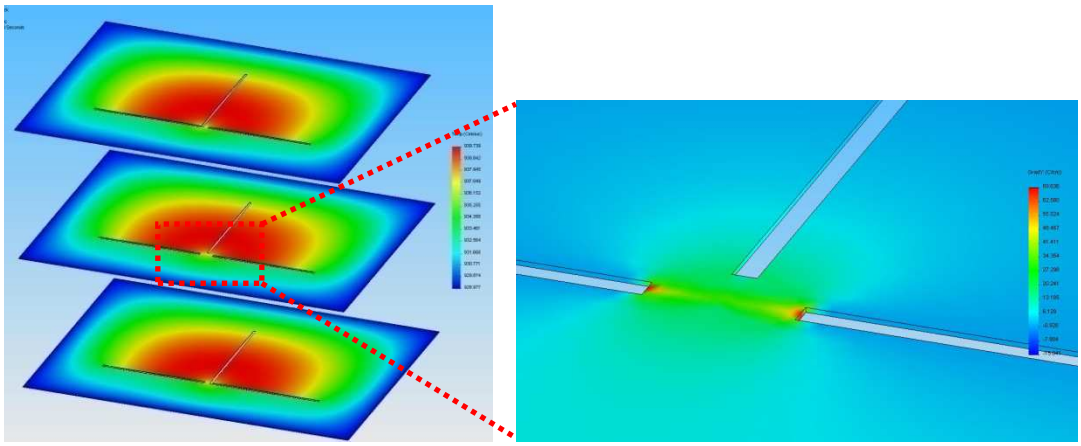

(a) (b)

Figure 3-21. FEA results of (a) temperature profile and (b) thermo gradient profile of a simple microlaminated device having microchannels

3.7.2 Experimental Approach

Bose and Paul (2008) conducted a set of experiments to compare different methods of heating and cooling microchannel devices. Two methods were used for the diffusion bonding of metal microchannel laminae in these experiments: 1) typical pressing within a vacuum hot press (VHP); and 2) an innovative internal convective heating (ICH) method. The ICH method takes advantage of the internal fluid flow paths within arrayed microfluidic devices to deliver thermal energy convectively from the internal surfaces of the device. The intent was to significantly reduce the distance over which thermal fluxes were applied in an effort to minimize thermal gradients throughout the device. The thermal loads on both approaches are 20° Celsius per minute. In addition, the bonding pressure, temperature, time, environment and surface condition was kept the same.

Figure 3-22 indicates that the VHP sample yielded mean channel warpage of 15.5 % having a standard deviation of 1.5%. Compared to the result from ICH shown in Figure 3-23, the mean channel warpage significantly reduced to 0.7 % having a standard deviation of 0.7 %. This provides evidence that thermal gradients generated during the heating and cooling cycles of diffusion bonding can lead to warpage within arrayed microchannel devices.

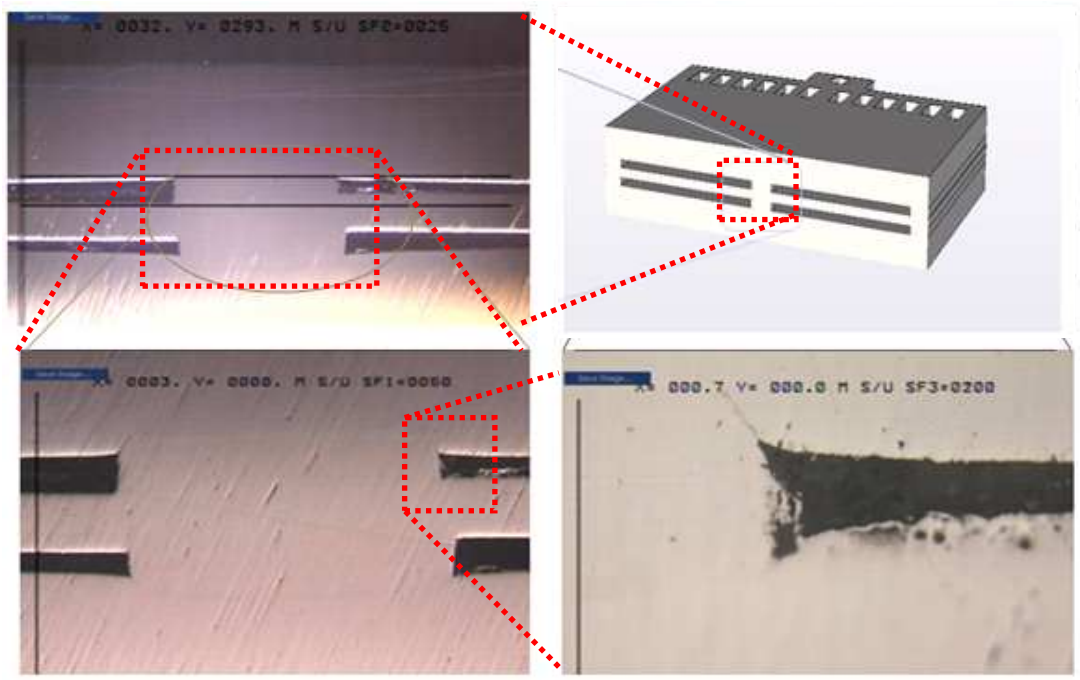

Figure 3-22. Metallography on VHP sample in channel region (Bose and Paul, 2008).

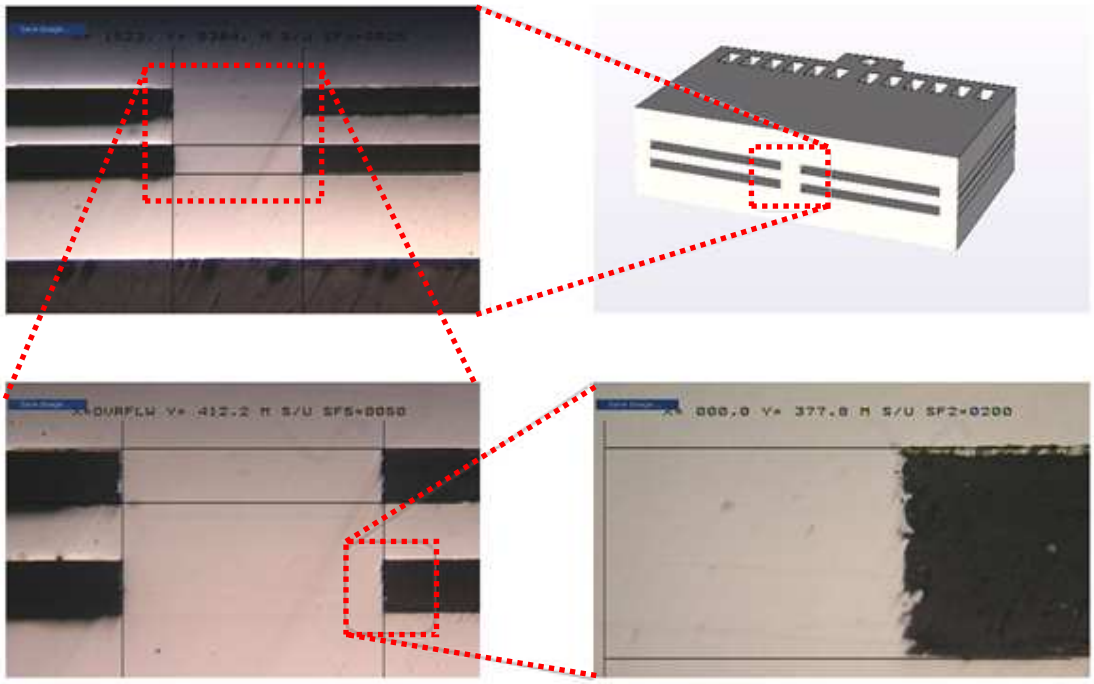

Figure 3-23. Metallography on ICH sample in the channel region (Bose and Paul, 2008).

3.7.3 Future Work

Currently in the lab, 1~2°C per minute cooling rates are being implemented. However, further studies need to be done to model the effect of thermal gradient during the heating and cooling cycle for the microlamination process. It is expected that the efficiency of the cooling cycle can be maximized by having the ability to estimate the critical thermal gradient value. This would provide improvements to the yield and reduce total diffusion bonding cycle time.

3.8 Fabrication: Poisson's Effect

Some of the warpage observed may be due to Poisson's effect. When compressive pressure is applied to the laminae during the diffusion bonding step, there could be induced stresses in lateral directions due to Poisson's effect (Hearn, 1985; Hibbeler, 2005). This induced lateral stress could translate to side loading and exceed the critical buckling load (Alfutov, 2000; Bloom et al., 2000; Ugural, 2008) of the microchannel structure resulting in warpage. This failure mode has not been reported in current literatures having microchannel applications. However, with respect to fundamental theory, Fang et al., 1994; Fang et al., 1999 published several articles regarding buckling and post-buckling behavior of micromachined beams. Carr et al., 2005 and Luo et al., 2008 further analyzed the buckling behavior of micro-scale beams using theoretical models and simulations. Martin et al., 2007 devised a detailed procedure for manufacturing micro-scale cross-sections having meso-scale spans. However, those researches use silicon wafers as base material which is usually not used in MECS applications.

In practice, the warpage induced by Poisson's effect had been observed in devices designed and fabricated in the lab (Figure 3-24). After diffusion bonding, the pressure drop across the device was found to be three times higher than predicted from computational fluid dynamics (CFD) analysis. To understand the cause of this discrepancy between the actual result and the predictive model, a metallographic analysis was carried out (refer to Zipperian, 2008 for detailed procedure). It was identified that in addition to structural creep throughout the device, there was significant warpage near the outlet (shown in Figure 3-24). However, given the fact that both inlet and outlet have the same channel and side wall dimensions, the only difference is the span of the opening. In this particular design, the inlet opening was relatively small compared to the outlet opening. This suggests that other warpage mechanisms such as Poisson's effect could be impacting the end result features of the

microreactors. Detailed model and experiments were performed and will be discussed in the subsequent Chapter.

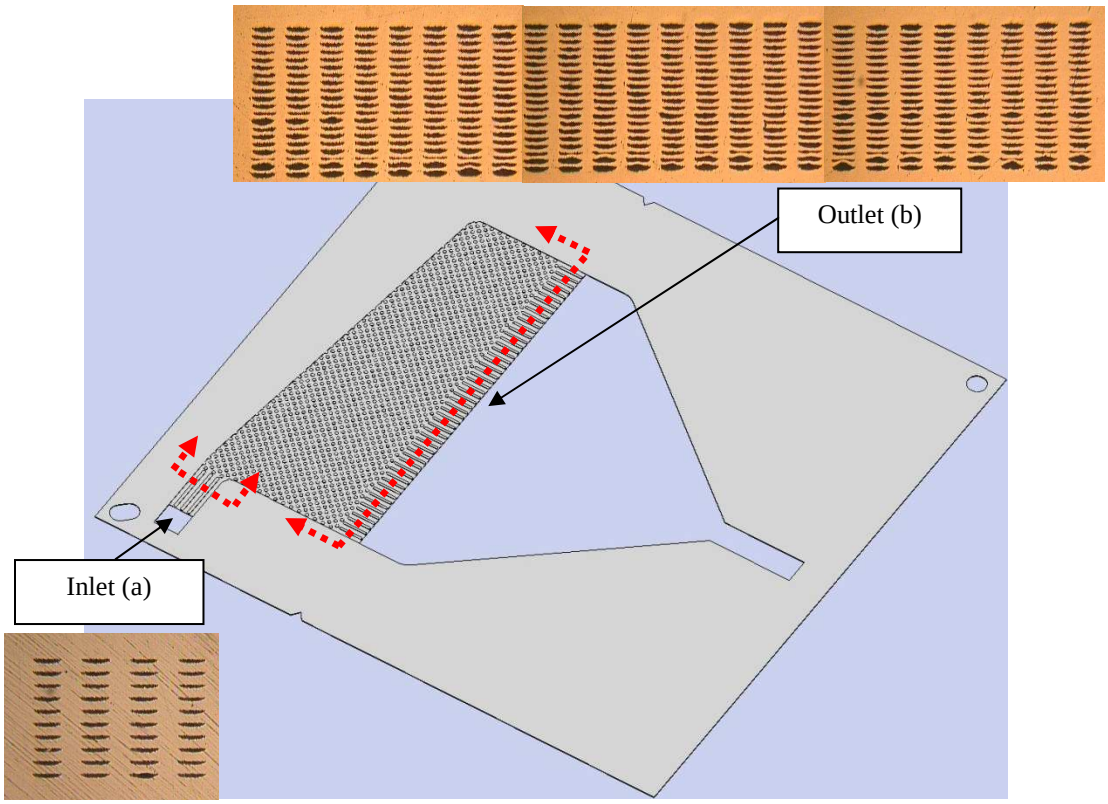

Figure 3-24. OSU designed microreactor with cross-sectional views at the mm inlet opening (a) and mm outlet opening (b)

3.9 Fabrication: Creep

Creep is defined as the increase of deformation with time without loading change (With, 2006). This rheological behavior may be explained as a combination of elastic and viscous behavior (visco-elastic deformation, recoverable), plastic and viscous behavior (visco-plastic deformation, non-recoverable) or even a combination of the three fundamental deformation types: elastic, plastic and viscous (elasto-visco-plastic behavior). The deformation rate usually decreases with time (Silva, 2006). The

creep formula can be formulated by describing the strain rate associated with the material properties and processing conditions (Silva, 2006; With, 2006). This formula can be expressed as

$$\frac{d\varepsilon}{dt} = \frac{C\sigma^m}{d^b} e^{\frac{-Q}{kT}} \tag{3-7}$$

where

ε = Creep strain

C = Constant dependent on the material and the particular creep mechanism

m and b = Exponent dependent on the creep mechanism

Q = Activation energy of the creep mechanism

σ = Applied stress

d = Grain size of the material

k = Boltzmann's constant

T = Absolute temperature

Since metals are generally used in MECS applications, the parameters for calculating creep can be found in Frost et al., 1982 and Aerospace Structural Metals Handbook.

As described in previous sections, diffusion bonding in microlamination occurs at elevated temperature which usually takes several hours to complete. During that time, compressive pressure was applied to cause macro-deformation and to provide intimate contact between the laminae. According to formula (3-7), the laminae will be subjected to creep under those conditions. The direct consequence of creep is reduction of channel height in microchannel structures. In addition, due to loss of structural support, significant warpage could be formed. Figure 3-25 shows one of the microchannel devices designed and manufacturing in the lab subjected to significant creep strain having the result of catastrophic warpage.

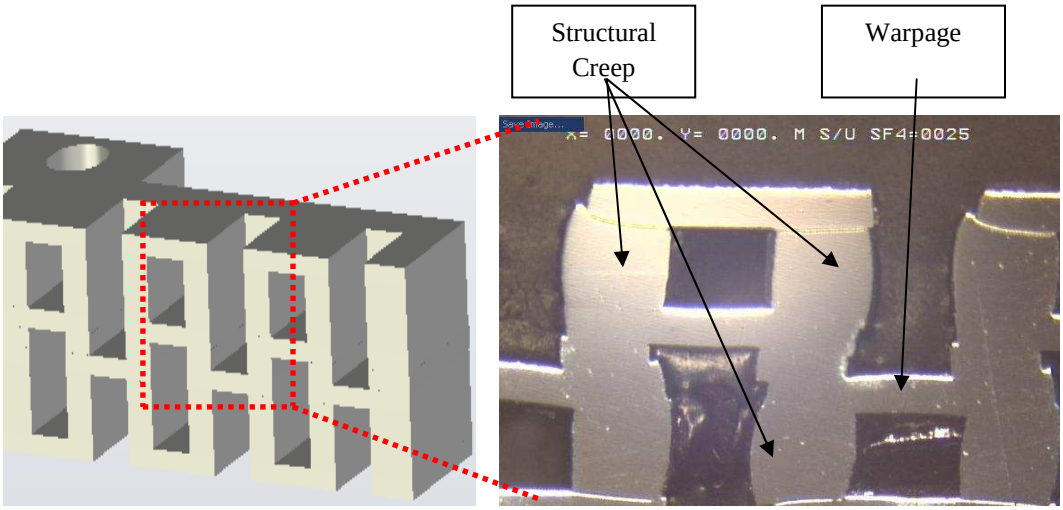

Figure 3-25. Schematic of the microchannel design (left) and actual cross-sectional view of the device

Future work needs to be done to investigate the relationship between creep and diffusion bonding time. When the laminae were subjected to excessive time during diffusion bonding, creep could potentially induce warpage. On the other hand, when not enough time allowed during bonding, delamination/leakage could form within the device.

3.10 Fabrication: Burrs

Burrs are referred as the raised edge on metal parts. Generally, burrs are unwanted material remaining after machining operations. To put this in perspective, when machining stainless steel, a traditional milling machine would create burrs on the order of a few hundred microns while laser micromachining would have tens of microns (shown in Figure 3-26).

During diffusion bonding, these burrs along the edges would prevent intimate contact between the laminae. In addition, the burrs would create high stress points

which could initiate warpage. Figure 3-27 shows the warpage created by laser micromachining burrs within a stainless steel device. Those images were taken using a non-destructive method called 3D X-ray imaging (courtesy of Xradia Inc.).

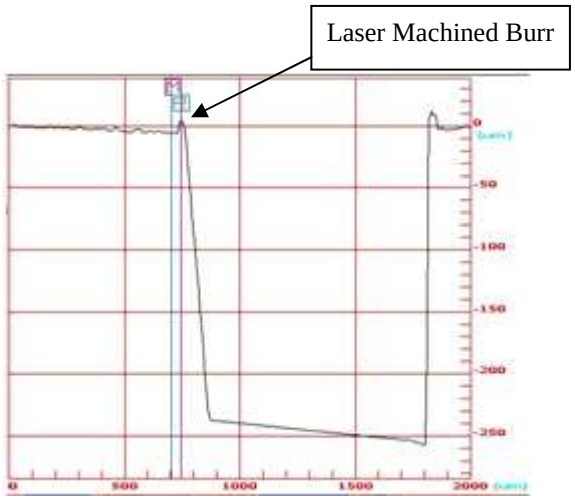

Figure 3-26. Surface profile scan of a 15µm laser machined burr

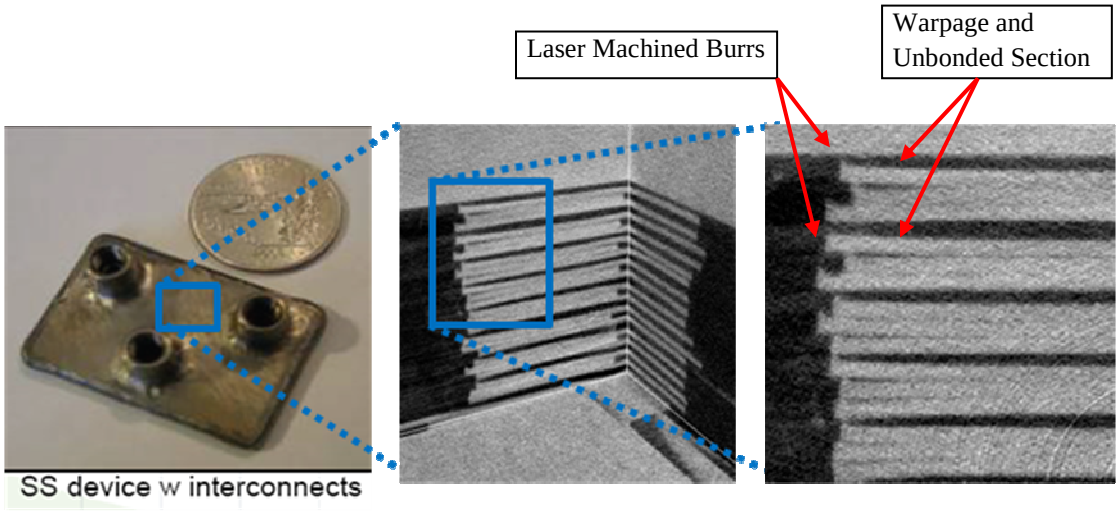

Figure 3-27. Warpage of stainless steel microchannel device caused by burrs generated from laser micromachining

To understand the effect of the burrs during diffusion bonding, a simple model can be applied using fundamental concentration based diffusion formula (Guy et al. 1974; Reed-Hill et al., 2008). This formula is expressed as

$$C = C_0\left[1 - erf\left(\frac{x}{2\sqrt{Dt}}\right)\right] \tag{3-8}$$

where C is the concentration at a distance of x centimeters below the surface after diffusion has occurred for t seconds; C_0 is the maximum (surface) concentration; $erf\left(\frac{x}{2\sqrt{Dt}}\right) = erf(y)$ is a function of the variable and $y = \frac{x}{2\sqrt{Dt}}$ is obtainable in the form of mathematical tables like logarithms and trigonometric functions; D is the diffusion coefficient which can be calculated using

$$D = Ae^{-\frac{Q}{RT}} \tag{3-9}$$

where A is the "frequency factor" which is related to the frequency of vibration of the diffusing atoms; R is the ges constant; Q is a measure of the energy barrier that tends to prevent diffusion from occurring; T is the absolute temperature being applied. Assumptions had been made that A, Q, and R are independent of temperature.

In the example of microlamination (shown in Figure 3-28), assuming both laminae have a perfectly flat surface and the atoms in top lamina needs to diffuse down to the bottom lamina across the burr height (which is distance x). By having C equal to 50% (assuming diffusion takes place in both directions) and taking values standard α-iron to α-iron constants. The relationship between diffusional distance and time is plotted in Figure 3-29. The figure showed that the required bonding time increased significantly when diffusional distance (burr height) is increased. This indicates that burrs not only create stress points within the device, but also creates diffusional barrier between the laminae which would cause leakage issues.

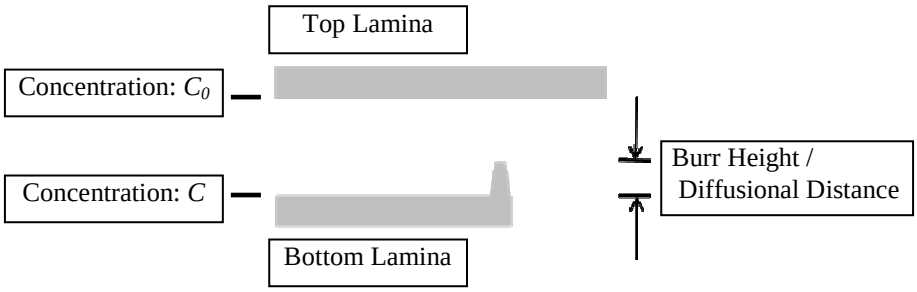

Figure 3-28. Schematic of simplified diffusion bonding condition having burred edges

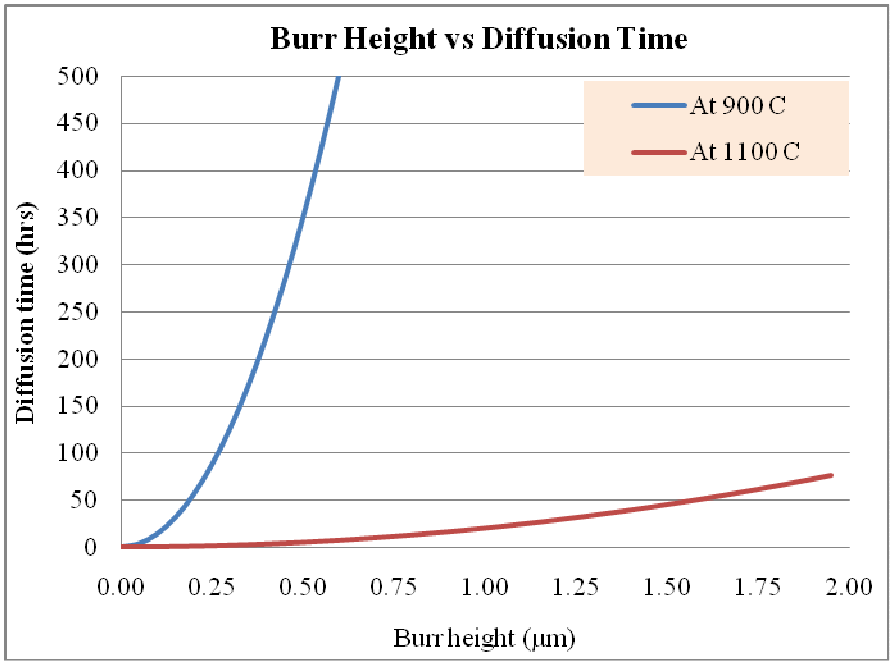

Figure 3-29. Diffusion distance verses time at 900°C and 1100°C

3.11 Summary

Improper stress distribution is a key source of microstructure warpage. This warpage mechanism leads to flow maldistribution which significantly reduces the device efficiency. Careful design and fabrication of arrayed microchannel devices can eliminate the flow maldistribution inside microchannel devices.

3.12 References

Aerospace Structural Metals Handbook, Columbus, Ohio: Mechanical Properties Data Center, Battelle Columbus Laboratories, 1970

Alfutov, N. A., translated by Evseev, E., Balmont, V. B., *Stability of Elastic Structure*s, Berlin; New York: Springer, 2000.

Ashby, M. F., *Materials selection in mechanical design*. Oxford; Boston: Butterworth-Heinemann, 1999.

ASM Handbook, Vol. 2, *Properties and Selection: Nonferrous Alloys and Special-Purpose Materials*, American Society for Metals, Cleveland, Ohio USA, 1990.

ASM Handbook, Vol. 4, *Heat Treating, Cleaning and Finishing*, American Society for Metals, Cleveland, Ohio USA, 1990.

Bloom F., Coffin, D., *Handbook of Thin Plate Buckling and Post-Buckling*, Boca Raton, FL: Chapman & Hall/CRC, 2000.

Boley, B. A., Weiner, J. H., *Theory of Thermal Stresses*, NY: Wiley Publishing, 1960

Bose, S., Paul, B. K., "An Internal Convective Heating Cycle for Diffusion Bonding Highly Parallel Microchannel Architectures," Thesis Document, Not published yet.

Carr, S. M., Lawrence, W. E., Wybourne, M. N., "Static buckling and actuation of free-standing mesoscale beams," *IEEE Transactions on Nanotechnology*, Vol. 4, n 6, pp. 655-659, 2005

Chan, E. M., Mathies, R. A., Alivisato, A. P., "Size-controlled growth of CdSe nanocrystals in microfluidic reactors," *Nano Letters*, n 3, pp. 199-201, 2003

Chang, C. –H., Paul, B. K., Remcho, V. T., Atre, S., Hutchison, J. E., "Synthesis and post-processing of nanomaterials using microreaction technology," *Journal of Nanoparticle Research*, Vol. 10, n 6, pp. 965-980, 2008

Chao, S. –H, Holl, M. R., Koschwanez, J. H., Seriburi, P., Meldrum, D. R., "Scaling for microfluidic mixing," Proceedings of the 3rd International Conference on Microchannels and Minichannels, *2005*, Vol. Part B, pp. 329-336, 2005

Davis J. R., *Metals Handbook*, Materials Park, Ohio: ASM International, 1998

Ehrfeld W., Hessel V., and Lowe H., *Microreactors: New Technology for Modern Chemistry*, Weinheim ; New York : Wiley-VCH, 2000

Fang, W. -L., Lee, C. -H. , Hu, H. -H., "On the buckling behavior of micromachined beams," *Journal of Micromechanics and Microengineering*, Vol. 9, n 3, pp. 236-244, 1999

Fang, W., Wickert, J.A., "Post-buckling of micromachined beams," *Journal of Micromechanics and Microengineering*, Vol. 4, n 3, pp. 116-122, 1994.

Frost, H. J., Ashby, M. F., *Deformation-mechanism maps : the plasticity and creep of metals and ceramics*, Oxford; New York : Pergamon Press, 1982.

Gere, J. M. and Timoshenko, S. P., *Mechanics of materials*. Boston: PWS-KENT Pub. Co., 1997.

Gossard, M. L., Seide, P., Roberts, W. M., "Thermal buckling of plates," *NACA Technical Note 2771*, Document ID# 19930083554, pp. 1-40, 1952.

Guy, A. G., Hren, J. J., *Elements of Physical Metallurgy*, Addison-Wesley Educational Publishers Inc; 3rd edition, 1974

Hearn, E. J., *Mechanics of Materials: An Introduction to the Mechanics of Elastic and Plastic Deformation of Solids and Structural Components*, Oxford, OX, England ; New York : Pergamon Press, 1985.

Hetnarski, R. B., "Basic Equations of the Theory of Thermal Stresses," in *Thermal Stresses, Vol. I*, Elsevier Science Publishers, 1986

Hibbeler, R. C., *Mechanics of Materials*, Upper Saddle River, N.J.: Pearson/Prentice Hall, 2005.

Kovalenko, A. D., *Thermoelasticity*, Wolters-Noordhoff Publishing, Groningen, 1969

Luo, C., Francis, A., Liu, X.-C., "Determination of compressive residual stress in a doubly-clamped microbeam according to its buckled shape," *Microelectronic Engineering*, Vol. 85, n 2, pp. 339-347, 2008

Martin, M. J., White, R. D., Kurabayashi, K., Boyd, I. D., "Fabrication of beam structures with micro-scale cross-sections and meso-scale spans," *Journal of Micromechanics and Microengineering*, Vol. 17, n 12, pp. 2516-2521, 2007

Martin, P.M., Matson, D.W., Bennett, W.D., "Microfabrication methods for microchannel reactors and separations systems," *Chemical Engineering Communications*, Vol. 173, pp. 245-254, 1999.

Martin, P. M., Matson, D. W., Bennett, W. D., Stewart, D. C., Lin, Y., "Laser micromachined and laminated microfluidic components for miniaturized thermal, chemical and biological systems," *Proceedings of SPIE - The International Society for Optical Engineering*, Vol. 3680, n. 2, pp. 826-833, 1999.

Matson, D. W., Martin, P. M., Tonkovich, A. Y., Roberts, G. L., "Fabrication of a stainless steel microchannel microcombustor using a lamination process," *Proceedings of SPIE - The International Society for Optical Engineering*, Vol. 3514, pp. 386-392, 1998.

Matson, D. W., Martin, P. M., Bennett, W. D., "Laser machined components for microanalytical and chemical separation devices," *Proceedings of SPIE - The International Society for Optical Engineering*, Vol. 3519, pp. 200-207, 1998.

Nowacki, W., *Thermoelasticity*, Oxford, U.K.: Pergamon Press, 1962

Popov, E. P., *Engineering mechanics of solids*. Upper Saddle River, N.J.: Prentice Hall, 1999.

Paul, B. K., Dewey, T., Alman, D., and Wilson, R. D., "Intermetallic Microlamination for High-Temperature Reactors," presented at *4th International Conference on Microreaction Technology*, Atlanta, GA, 2000.

Paul, B. K., Dewey, T., Alman, D., and Wilson, R. D., "An evaluation of two methods for producing intermetallic microchannels," *American Society of Mechanical Engineers, Micro-Electromechanical Systems Division Publication (MEMS)*, pp. 261-266, 2002.

Paul, B. K., Kwon, P., Subramanian, R., "Understanding limits on fin aspect ratios in counterflow microchannel arrays produced by diffusion bonding," *Journal of Manufacturing Science and Engineering, Transactions of the ASME*, Vol. 128, n. 4, pp. 977-983, 2006.

Paul, B. K. and Peterson, R. B., "Microlamination for Microtechnology-based Energy, Chemical, and Biological System," Presented at *ASME IMECE*, Nashville, Tennessee, 1999.

Reed-Hill, R. E., Abbaschian, R., *Physical Metallurgy Principles*, Cengage-Engineering; 4th edition, 2008

Schubert, K., Brandner, J., Fichtner, M., Linder, G., Schygulla, U., and Wenka, A., "Microstructure devices for applications in thermal and chemical process engineering," *Microscale Thermophysical Engineering*, v 5, n 1, pp. 17-39, 2001

Shames, I. H., *Introduction to Solid Mechanics*. Englewood Cliffs, NJ: Prentice Hall, 1999.

Silva, V. D., *Mechanics and Strength of Materials*, Berlin ; London : Springer, c2006.

Tauchert, T. R., "Thermally induced flexure, buckling, and vibration of plates," *Applied Mechanics Reviews*, Vol. 44, n 8, pp. 347, 1991.

Templin, R. L. et al., *Properties of Metals in Materials Engineering***,** Cleveland, 1948

Thornton, E. A., Coyle, M. F., McLeod, R. N., "Experimental study of plate buckling induced by spatial temperature gradients," *Journal of Thermal Stresses*, Vol. 17, n 2, pp. 191-210, 1994.

Timoshenko, S., *Theory of Elastic Stability*. New York, Toronto, London: McGraw-HILL Book Company, 1961.

Tseng, C. H.,Paul, B. K., "A Comparison of the Mass Transfer Performance of Conventional and Micromanufactured Porous Membranes," *Proceedings of the American Society for Precision Engineering*, 2003

Tseng, C. H.,Paul, B. K., "Comparison of mixing approaches in the synthesis and deposition of ceria nanoparticles," Proceedings of the ASME International Manufacturing Science and Engineering Conference 2007, pp. 635-641, 2007

Tseng, C. H.,Paul, B. K., "Comparison of batch mixing and micromixing approaches in the synthesis and deposition of ceria nanoparticles," Transactions of the North American Manufacturing Research Institute of SME, pp. 231-238, 2007

Ugural, A. C., *Mechanics of Materials*, Hoboken, N.J. : Wiley ; Chichester : John Wiley [distributor], 2008.

Upthegrove, C. and Burghoff, H. L., *Elevated-Temperature Properties of Coppers and Copper-Base Alloys*, ASTM Special Technical Publication No. 181, ASTM, Philadelphia, PA

Wattanutchariya, W., Paul, B. K., "Bonding fixture tolerances for high-volume metal microlamination based on fin buckling and laminae misalignment behavior," *Precision Engineering*, Vol. 28, n 2, pp. 117-128, 2004

Wattanutchariya, W., Paul, B. K., "Effect of fixture compliance on Thermally Enhanced Edge Registration in microlamination," *Journal of Manufacturing Science and Engineering, Transactions of the ASME*, Vol. 126, n 4, pp. 845-848, 2004

With, G. De., *Structure, Deformation, and Integrity of Materials: v. 2. Plasticity, Visco-Elasticity, and Fracture*, Weinheim ; Great Britain : Wiley-VCH, 2006.

Zhou, G. –Y., Tu, S. –T., "Viscoelastic analysis of rectangular passage of microchanneled plates subjected to internal pressure," *International Journal of Solids and Structures*, Vol. 44, n. 21, pp. 6791-6804, 2007

Zipperian, D. C., *Metallographic Specimen Preparation Basics*, Pace Technologies, http://www.metallographic.com/Technical/Basics.pdf

CHAPTER 4

Buckling of Microchannel Fin Structures Due to Poisson's Effect during Diffusion Bonding

4.1 Abstract

Diffusion based operations have been proven to be much more effective and efficient in devices fabricated in microchannel structures. These devices are generally constructed of several layers of thin laminae to generate individual microchannels. Fabricating microscale devices depend on consistent spacing between channels to define diffusional distances. Warpage or deformation in these channels can lead to variations of channel dimensions which reduce the efficiency of the system. In previous chapters, causes of channel warpage were identified and reviewed. In this chapter, one of the causes, Poisson's effect, is isolated and analyzed to investigate how compressive pressure applied during diffusion bonding effects the channel dimensions.

4.2 Introduction

Based on the review on Chapter 3, several mechanically induced warpage mechanisms were summarized. In this Chapter, mechanically induced warpage due to Poisson's effect is discussed.

4.2.1 Mechanically Induced Warpage during Diffusion Bonding

In the bonding step of the microlamination process, laminae are put under compression between bonding fixtures normally made from refractory materials (graphite, ceramic, or high-temp alloys) placed in thermal vacuum pressure chamber. During this step, due to several mechanically induced warpage mechanisms previously indentified and categorized in Chapter 3, the laminae can deform. Nonuniform flow channels between the warpage fins (described in 3.2.4) can result as shown in Figure 4-1.

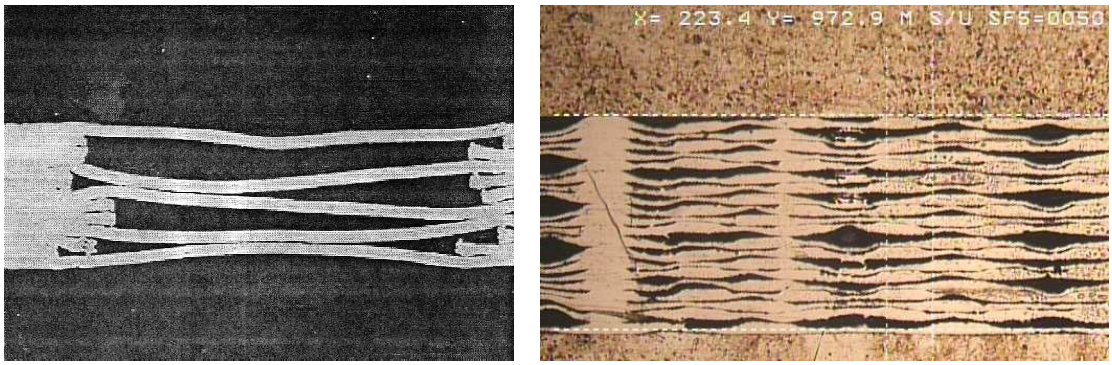

Paul et al. 2000 Tseng and Paul, 2008 (not published)

Figure 4-1. Optical microscope images of stainless-steel microchannel structures (a) and (b) with nonuniform flow channels.

4.3 Investigation of Mechanically Induced Warpage Due to Poisson's Effect

Compressive pressure applied to the laminae during diffusion bonding step could induce stresses in lateral directions due to Poisson's effect (Hearn, 1985; Alfutov, 2000; Budynas and Young, 2001). This induced lateral stress could translate to side loading and exceed the critical buckling load (Alfutov, 2000; Bloom et al., 2000; Ugural, 2008) of the microchannel structure resulting in warpage. This failure

mode has not been reported in the current literature describing microchannel applications. However, with respect to fundamental theory, Fang et al., 1994; Fang et al., 1999 published several articles regarding buckling and post-buckling behavior of micromachined beams. Carr et al., 2005 and Luo et al., 2008 further analyzed the buckling behavior of micro-scale beams using theoretical models and simulations. Martin et al., 2007 devised a detailed procedure for manufacturing micro-scale cross-sections having meso-scale spans. However, those reserchers use silicon wafers as base material which is usually not used in MECS applications.

Figure 4-2 shows a microlaminated device developed at OSU. After bonding, a metallographic analysis was carried out (refer to Zipperian, 2008 for detailed procedure). It was identified that in addition to structural creep throughout the device, there was significant warpage near the bottom of the outlet (shown in Figure 4-2). However, given the fact that both inlet and outlet have similar channel and side wall dimensions, the major difference is that the outlet is adjacent to a much larger plenum allowing for concentration of stress. This suggests the possibility that a stress induced deformation such as Poisson's effect could be the cause.

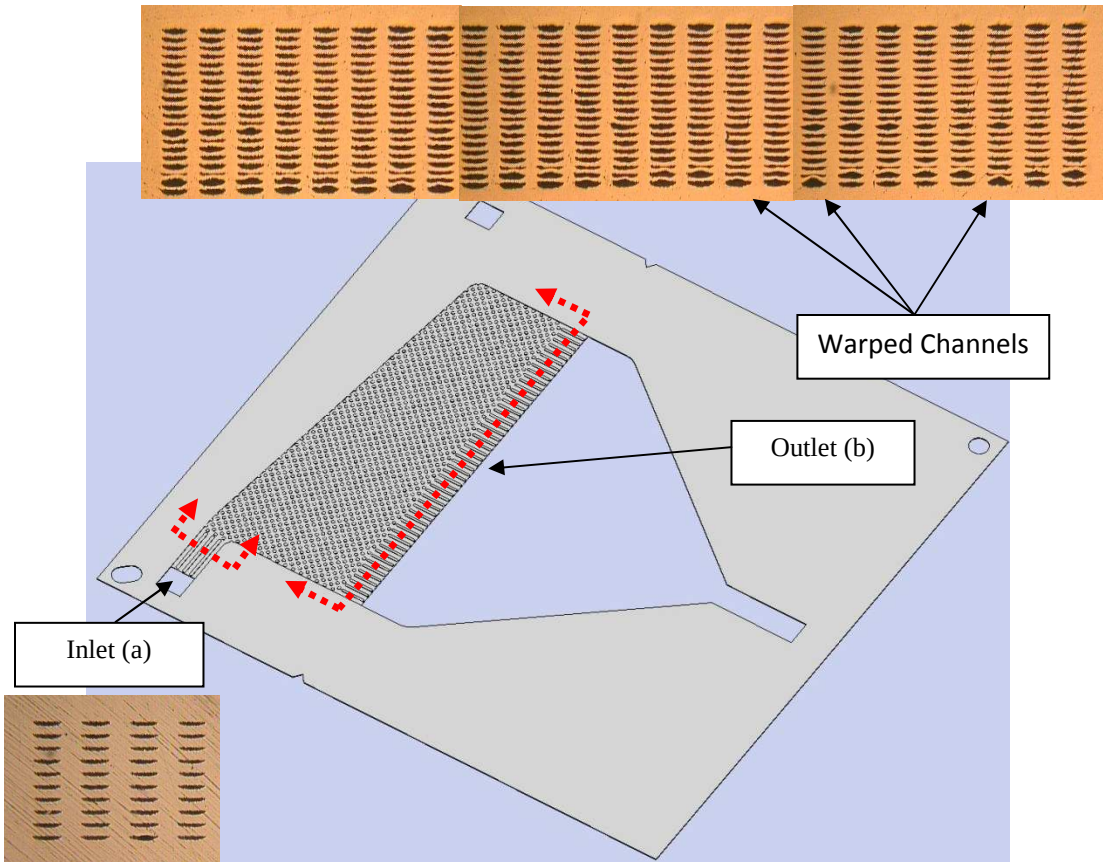

Figure 4-2. OSU designed microreactor with cross-sectional views at the mm inlet opening (a) and mm outlet opening (b).

4.4 Objectives

The goal of this research is to identify and isolate one of the mechanisms of the mechanically induced warpage. Once the mechanism is isolated, theoretical model can be proposed then tested. The following are detailed descriptions of the objectives:

1) Define a mathematical model which combines the parameters of Poisson's ratio and the traditional critical buckling load
2) Develop a FEA model to verify that uniform pressure is being applied throughout the surface of the test sample

3) Perform preliminary experiments using test coupons
4) Validate the mathematical model by varying individual parameters and compare with actual test data
5) Summarize the results and critique of the model for use in selecting future design criteria

4.5 Theoretical Model

Compressive longitudinal pressure during bonding process translates to lateral stress using Poisson's ratio. This lateral stress being applied on the microchannel structure can then be compared with the critical buckling load. In theory, if the lateral stress exceeds the critical buckling load limit, the structure will buckle resulting in microchannel warpage.

4.5.1 Poisson's Ratio

Poisson's Ratio is the ratio of the relative contraction strain (lateral strain normal to the applied load) divided by the relative extension strain (longitudinal strain) in the direction of the applied load (Hearn, 1985; Alfutov, 2000; Budynas and Young, 2001). This ratio can be expressed as:

$$\upsilon = \frac{\varepsilon_{lat}}{\varepsilon_{long}} \tag{4-1}$$

where

υ = Poisson's ratio

ε_{lat} = Lateral strain

ε_{long} = Longitudinal strain

4.5.2 Young's Modulus

In solid mechanics, Young's modulus (E) is a measure of the stiffness of an isotropic elastic material. It is also known as modulus of elasticity, elastic modulus or tensile modulus. It is defined as the ratio of the uniaxial stress over the uniaxial strain in the range of stress in which Hooke's Law holds. This modulus can be calculated by dividing the tensile stress by the tensile strain:

$$E = \frac{\sigma}{\varepsilon} \tag{4-2}$$

where

E = Young's modulus [N/m^2]

σ = uniaxial stress [N/m^2]

ε = uniaxial strain

4.5.3 Lateral Stress Induced by Poisson's Ratio

By combining equation 4-1 and 4-2, assuming in the range of stress which Hooke's Law holds, the equation can be expressed by using lateral and longitudinal stresses and be rewritten as:

$$\upsilon = \frac{\varepsilon_{lat}}{\varepsilon_{long}} = \frac{\frac{\sigma_{lat}}{E}}{\frac{\sigma_{long}}{E}} = \frac{\sigma_{lat}}{\sigma_{long}} \tag{4-3}$$

where

σ_{lat} = lateral stress induced by Poisson's ratio [N/m^2]

σ_{long} = uniaxial stress/compressive bonding pressure [N/m^2]

During diffusion bonding (described in 4.2.2), the longitudinal stress is the compressive bonding pressure being applied to the sample. Thus from formula 4-3, the lateral stress induced by Poisson's ratio can be expressed as:

$$\sigma_{lat} = \upsilon \cdot \sigma_{long} \tag{4-4}$$

This can be represented by a simple model shown in Figure 4-3.

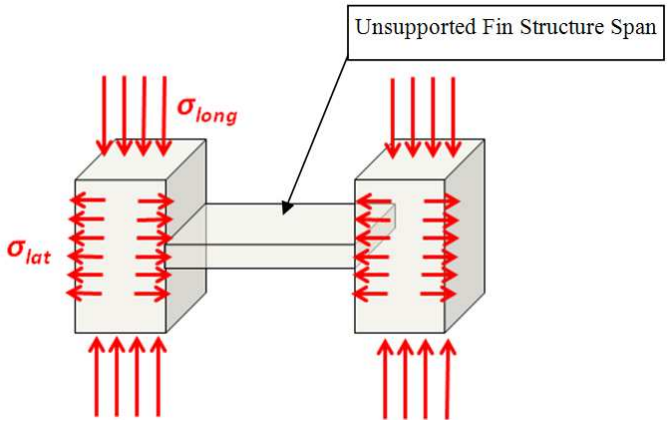

Figure 4-3. Schematic of the lateral stress induced by longitudinal stress (Poisson's ratio).

4.5.4 Critical Buckling Load

Buckling is a failure mode characterized by a sudden failure of a structural member subjected to high compressive stress, where the actual compressive stress at the point of failure is less than the ultimate compressive stresses that the material is capable of withstanding. This mode of failure is also described as failure due to elastic instability.

In 1757, mathematician Leonhard Euler derived a formula that gives the maximum axial load that a long, slender, ideal column can carry without buckling. The maximum axial load, or the critical buckling load, causes the column to be in a state of unstable equilibrium; that is, any increase of load, or the introduction of the slightest lateral force, will cause the column to fail by buckling. The Euler formula for columns is:

$$F_{critical} = K\frac{\pi^2 EI}{(b)^2} \tag{4-5}$$

where

$F_{critical}$ = maximum or critical buckling force [N]

I = area moment of inertia [m^4]

b = unsupported structure span [m]

K = column effective length factor

Using the formula, additional formulas had been derived and researched (Alfutov, 2000). In order to adapt with microchannel applications as shown in Figure 4-4 (a) discussed in previous sections, the critical buckling load formula for rectangular plates was implemented. Schematics of such model have been plotted in Figure 4-4 (b). The microchannel plate structure (subjected to buckling) is only supported along the two long edges have the other two edges free. Thus the microchannel length is denoted as l while the span is denoted as b. Thus the critical buckling stress ($\sigma_{critical}$) can be determined as:

$$\sigma_{critical} = K\frac{\pi^2 D}{b^2} \tag{4-6}$$

where

D = bending stiffness/moment parameter of the plate [Pa·m]

The bending stiffness parameter of a plate relates the applied bending moment to the resulting deflection. It is the product of the elastic modulus (E) and the area moment of inertia (I) which can be represented as:

$$D = \frac{Et^3}{12(1-\nu^2)} \tag{4-7}$$

where

t = plate thickness [m]

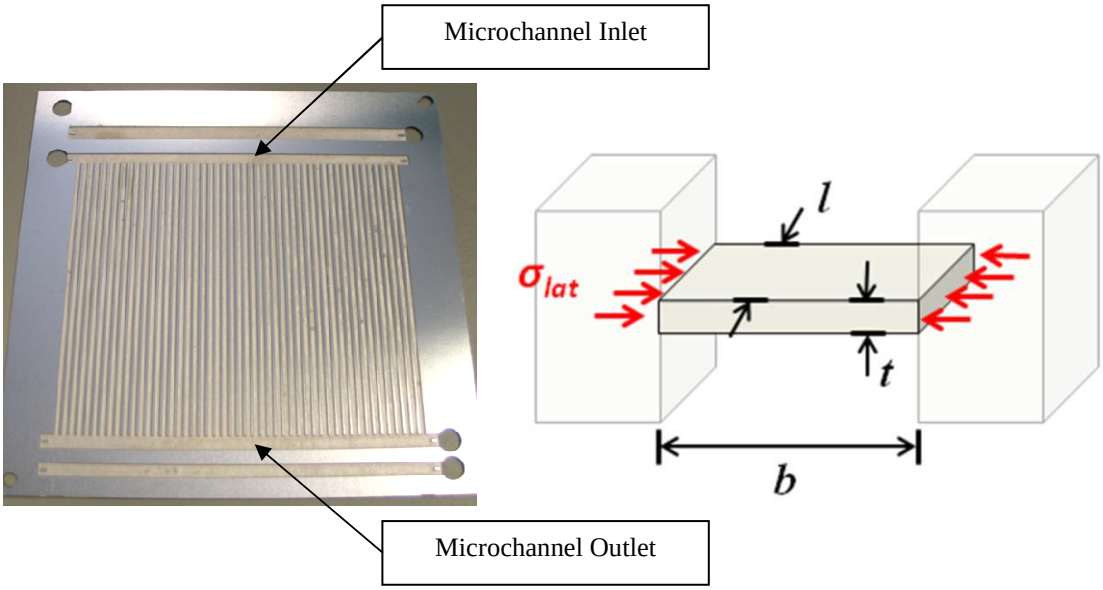

Figure 4-4. Actual microchannel design (a) and simplified schematics of the microchannel fin structure used in critical buckling stress calculation.

Applying (4-6) and (4-7), assuming both side of the plate structure are fixed (K = 4), a equation of critical compressive stress for plate structure can be derived as (Alfutov, 2000)

$$\sigma_{critical} = \frac{\pi^2 E}{3(1-\nu^2)}\left(\frac{t}{b}\right)^2 \tag{4-8}$$

Note that in this formula, the length of the microchannel (l) had been cancelled out thus does not any effect to the model. However, this is an assumption that should be investigated in the future.

By comparing the critical buckling stress described in formula (4-8) with the induced Poisson's stress described in formula (4-4), the formula can be rewritten as:

$$\sigma_{long} = \left(\frac{\pi^2}{3}\right)\frac{E}{\nu\cdot(1-\nu^2)}\left(\frac{t}{b}\right)^2 \tag{4-9}$$

The formula relates the compressive bonding pressure (σ_{long}) to the material's mechanical properties (E and ν) and the structural dimensions (t and b). For example, copper alloy 11000 shimstock can be used to manufacture microreactors. By having the mechanical and structural properties of:

E = 1.15 x 10^{11} [N/m^2] (at room temperature)

ν = 0.343 (at room temperature)

t = 2.5 x 10^{-5} [m]

b = 2.0 x 10^{-2} [m]

According to the formula, any bonding pressure greater than 1,953,264 N/m^2 (about 283 psi) would result in buckling at room temperature. To put in perspective, typical bonding pressures used in microlamination are generally between 800 to 3000 psi at elevated temperature. This indicates that the example given above will have

concerns of buckling warpage due to Poisson's effect. To investigate this hypothesis and the mathematical model, further experiments are needed.

4.6 Preliminary Experiment

4.6.1 Material

For this experimental design, copper alloy 11000 (McMaster-Carr #9709K54) was selected due to the manufacturability discussed below and mechanical properties at room temperature. This copper alloy has relatively low Young's modulus (115 GPa) and melting temperature (liquidus temperature: 1085°C; solidus temperature: 1065°C) (Davis, 1998 and Templin, et al., 1948). This allows performing experiments at room temperature. In addition, during material patterning, if the copper sample was burred or had suffered from thermal/mechanical stress damage, it can be annealed and flattened through an annealing cycle (ASM Handbook Vol. 2; ASM Handbook Vol. 4) Other metals such as stainless steel and nickel were also considered. However, both materials could generate burrs during patterning and cannot be annealed easily. This would create variations in the features of the test coupon.

The bonding fixture (described in 4.2.2) which provides the compressive pressure is made of 95% alumina and was purchased from CoorsTek (material number AD-995). The alumina fixture is 2 inches by 2 inches by 0.5 inch and was double-side grund to hold flatness and parallelism to less than 12.7 µm over the whole surface. The maximum surface roughness (R_{max}) is 0.762 µm while the average surface roughness is about 0.19 µm.

4.6.2 Preliminary Test Coupon Design

To verify the mathematical model, a preliminary test coupon was designed (shown in Figure 4-5). For detailed specifications and dimensions, please refer to the engineering package in Appendix H. In this preliminary test, four test coupons were manufactured and tested. Each preliminary test coupon has three laminae as shown in Figure 4-5 (a) and the dimension for each lamina was 1 inch by 2 inches (actual surface area of 1.526 inch^2). Each test coupon is designed so that the fin structure in middle lamina is unsupported as the unsupported column depicted in Figure 4-5. As shown in Figure 4-5 (a), each middle lamina incorporates four different fins structure lengths having 15, 20, 25, and 30 mm. The length of the fin has been set according to the mathematical model and the material properties at room temperature.

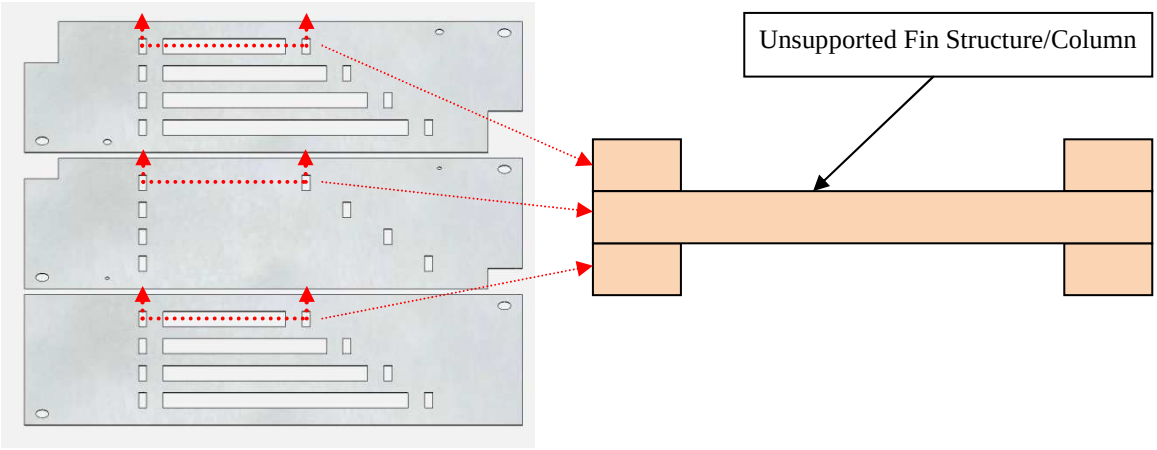

(a) (b)

Figure 4-5. Top view (a) and cross-sectional side view (b) of the preliminary test coupon design.

Other than the fin structures, the test coupon also incorporates registration pin holes and fiducial on diagonal corners. To register the position of the stacked test coupons, 1/16 inch registration pins were used. The dowel pins were purchased from McMaster-Carr (#97395A405) with both ends pre-tapered to allow easy insertion to

the registration pin holes. The manufacture suggested size for the pin holes ranges between 0.0620” to 0.0625”. To validate if the registration pins are registering the stacked test coupons, fiducial had been implemented and can be checked. For details of the fiducial design, please refer to Appendix G.

4.6.3 Experimental Process Plan

4.6.3.1 Patterning

To manufacture the test coupons, a laser µVia drilling machine was used (ESI model 5330). This laser system is a pulsed Nd:YAG laser which operates at 355 nm wavelength and can output > 5.7 Watts at 30 kHz. The accuracy of the laser is ± 20 µm over 533 mm by 635 mm. In addition, the maximum velocity for this laser machine is 500 mm/sec so it makes this process a fast and efficient way for prototyping samples with through cut designs (Matson et al, 1998; Martin et al. 1999). The parameters used for the fabrication of the test coupons were optimized to minimize thermal stress during laser machining. The consequence of using non-optimized parameters is shown in Figure 4-6. There are two sets of parameters listed in the table because the fiducial markings are not a through cut features.

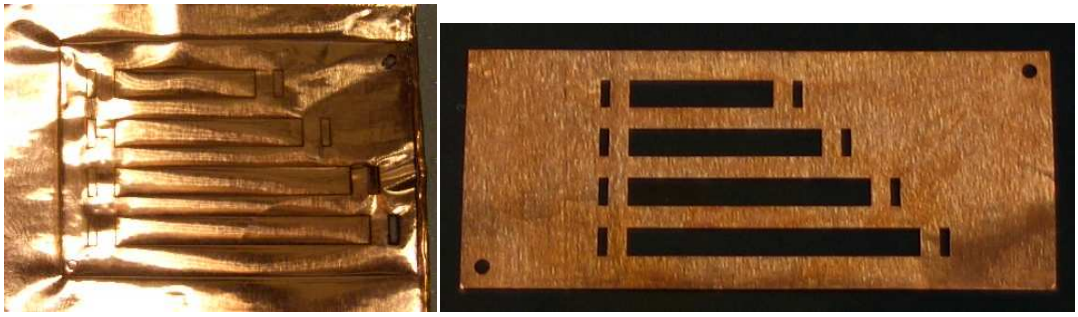

(a) (b)

Figure 4-6. Images of laser machining results using (a) non-optimized and (b) optimized parameters.

4.6.3.2 Flattening and Annealing

Though the optimized parameters were used, the test coupons still needed to go through flattening and annealing cycle. The recipe was referenced from ASTM standards (Davis, 1998 and Templin, et al., 1948). This additional procedure is to remove any thermal stresses and edge burrs created during laser machining. The burrs created from laser machining are typically between 15 to 35 µm and can be flattened to below 1.5 µm (shown in Figure 4-7). In addition, this also removes any warpage caused by shipping and handling.

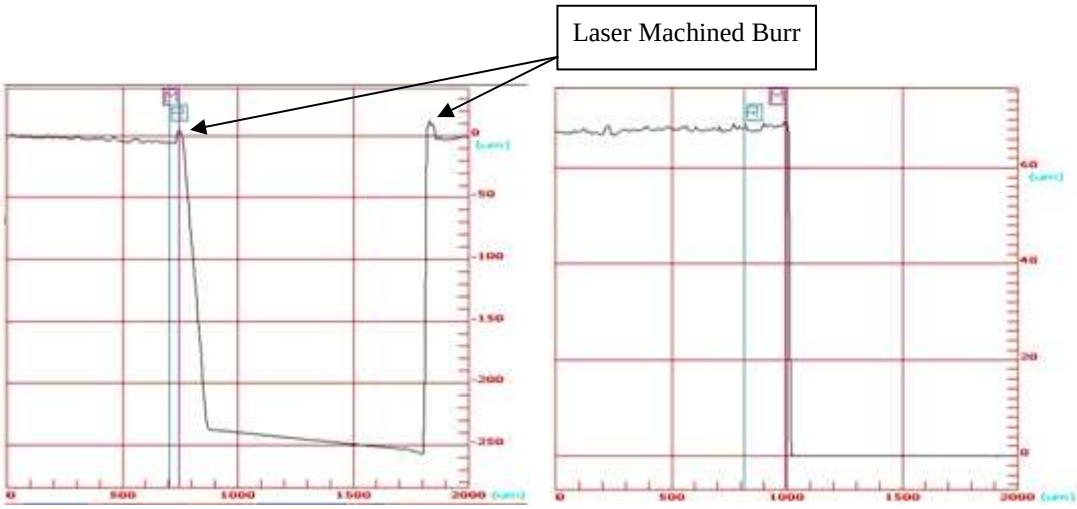

Figure 4-7. Laser machined burrs before (a) and burrs after (b) flattening/annealing.

4.6.4 Preliminary Test Protocol

As mentioned before in 4.4.2, the test coupon needs to be uniformly compressed in order to simulate actual process conditions during diffusion bonding. To provide uniform compressive pressure, ceramic blocks were used (Shown in Figure 4-8) as bonding fixtures. The whole structure was then compressed using a hydraulic press (Pressmaster model HP30-4560 from Thermal Technologies Inc.) which has a three inch diameter chamber thus can accommodate the test setup.

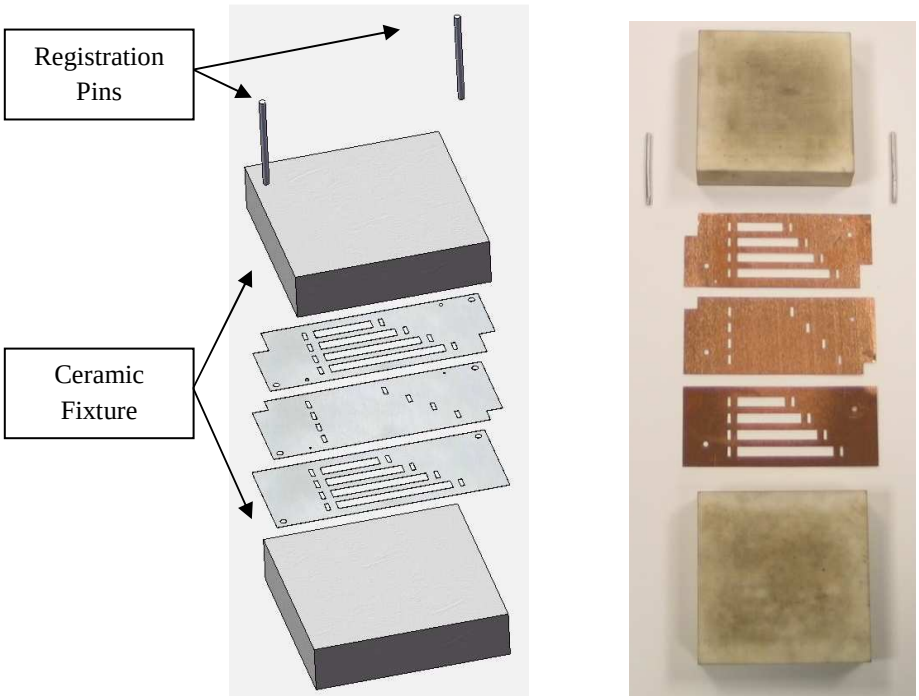

(a) (b)

Figure 4-8. SolidWorks rendered model of the test setup (a) and the actual setup (b).

As mentioned before, four test coupons (S1, S2, S3, and S4) were generated. Each coupon was applied under different static loads to simulate different diffusion bonding conditions. The static loads used in this experiment are 500, 1100, 2400, and 3800 pounds (lbs). During testing, the load was continuously applied for 15 minutes. Based on the coupon design which has actual surface area of 1.526 inch^2, this would translate to Poisson's lateral stresses of 111, 245, 535, and 847 pounds per square inch (psi). This generates four data points for each fin structure length for which results will be plotted.

In addition, to further validate if the pressure was uniformly distributed on the actual test coupon surface, finite element software (COSMOSWorks) was used. The software uses the test geometry imported from SolidWorks (3D model software) and can calculate response stress when the model is under compressive pressure at the surface. The result was then validated by using Fuji pressure sensor films (Low

Pressure LW film which operates between 363 and 1450 psi). The Fuji film is a two-sheet type pressure film which intensifies color change when subjected to higher pressure.

To quantify the buckling before and after being subjected to pressure, all four fin structures in each middle lamina were scanned three times using a surface scanning profilometer (see Appendix D for measuring equipment summaries). A surface profilometer would give surface height data along a scanning path. The buckling can be quantified by measuring the peak-to-valley distance of the data. Figure 4-9 shows the scan paths for one of the fin structures in middle lamina. After the test coupon was subjected to compressive pressure, each of the fin structures were scanned three times again. The registration features were also checked again to verify that the sample had not been misaligned during the experiment.

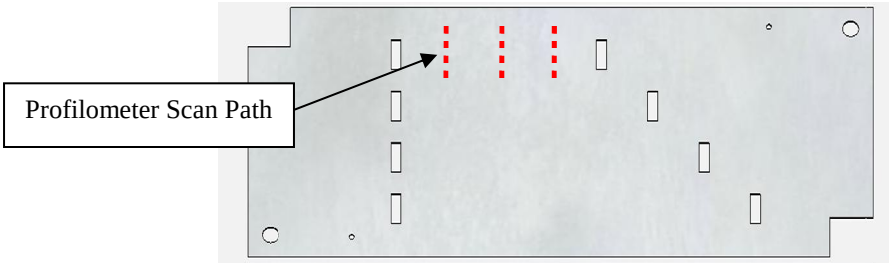

Figure 4-9. The profilometer scan paths for one of the fin structures.

4.6.5 Preliminary Results and Discussion

As mentioned before, each of the test coupons were manufactured and evaluated under different loads. The results from the surface profilometer scans are listed in Table 4-1. Each peak-to-valley value was averaged from the three scans before and after applying the pressure.

Table 4-1. Surface profilometer results from preliminary test coupons

	Applied Load (lbs)	Pressure (psi)	Poisson's effect (psi)	15 mm Fin P to V (µm)		20 mm Fin P to V (µm)		25 mm Fin P to V (µm)		30 mm Fin P to V (µm)	
				Before	After	Before	After	Before	After	Before	After
S1	604.26	396	136	**3.66**	**4.16**	**2.56**	**3.29**	**2.64**	**2.65**	**2.87**	**3.10**
S2	2261.10	1482	508	**2.86**	**3.56**	**3.30**	**2.58**	**2.49**	**3.78**	**3.65**	**4.40**
S3	5850.92	3834	1315	**3.40**	**5.46**	**2.91**	**5.23**	**2.79**	**4.50**	**2.51**	**6.17**
S4	9716.88	6367	2184	**2.99**	**5.65**	**2.70**	**9.47**	**2.40**	**6.04**	**2.87**	**9.15**

To understand how the results agree with the mathematical model, each fin structure length was separately plotted (shown in Figure 4-10). The horizontal markings represent peak-to-valley values before applying pressure while the triangle markings represent after pressure application. Since each value was averaged using three separate readings, the standard deviation was calculated accordingly. The vertical line represents the maximum theoretical pressure limit calculated from the mathematical model using formula 4-8. If the results plotted are on the right side of the limit, this indicates that the pressure applied has exceeded the critical buckling limit. By identifying the deviation of the peak-to-valley value before and after the application of pressure, the mathematical model can be validated. Based on the results plotted in Figure 4-10, the averaged peak-to-valley values appear to start deviating when exceeding the critical buckling limit. This indicates that the actual results agree with the mathematical model.

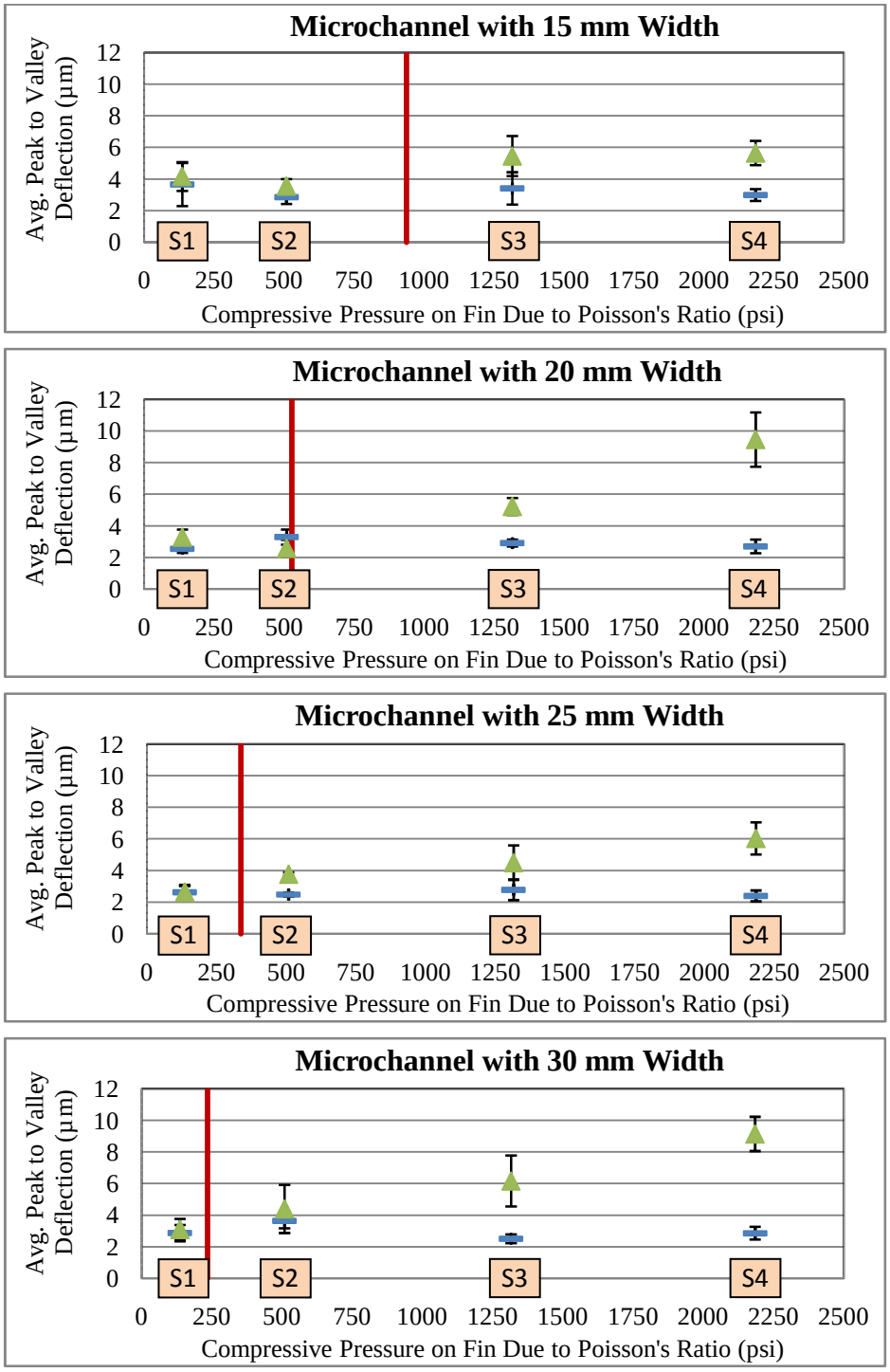

Figure 4-10. Preliminary test results plotted against 15, 20, 25, and 30 mm fin structures. The red line indicates maximum theoretical pressure limit.

To verify the results from preliminary data, the test coupon design was imported to COSMOSWorks and analyzed. The result from the analysis show that the fin structures in the middle lamina had stresses in lateral direction (Figure 4-11). The highest stresses were distributed along the long edges of the fin structure. In addition, the pressured surface of the support columns had uniform pressure distribution (Figure 4-12). This indicates that the lateral stresses are generated by Poisson's effect instead of structural non-uniform pressure distribution. However, from the same analysis, the maximum displacement/deflection value for the fin structure was around 10 nanometers (Figure 4-13) which is well below the values obtained from actual experiment. This could be possibly due to the inability of the software in recognizing the buckling caused by induced lateral stress.

Though the results from actual data and FEA show that the warpage was caused by exceeding critical buckling load, however, the averaged deviation from all the results was only about 2 μm. Comparing this value with the lamina thickness, the deviation was only about 3.2%. If the fin structure was buckling, the deviation should be catastrophic. After close examination of the test coupon design, it was clear that due to the middle shim design shown in Figure 4-14 (a), the warpage was restricted along the length of the fin structure. This restriction prevents the fin from buckling and thus explains the high stress distribution in the FEA results. In future testing, to isolate the Poisson's effect, modifications to the test coupons will be required.

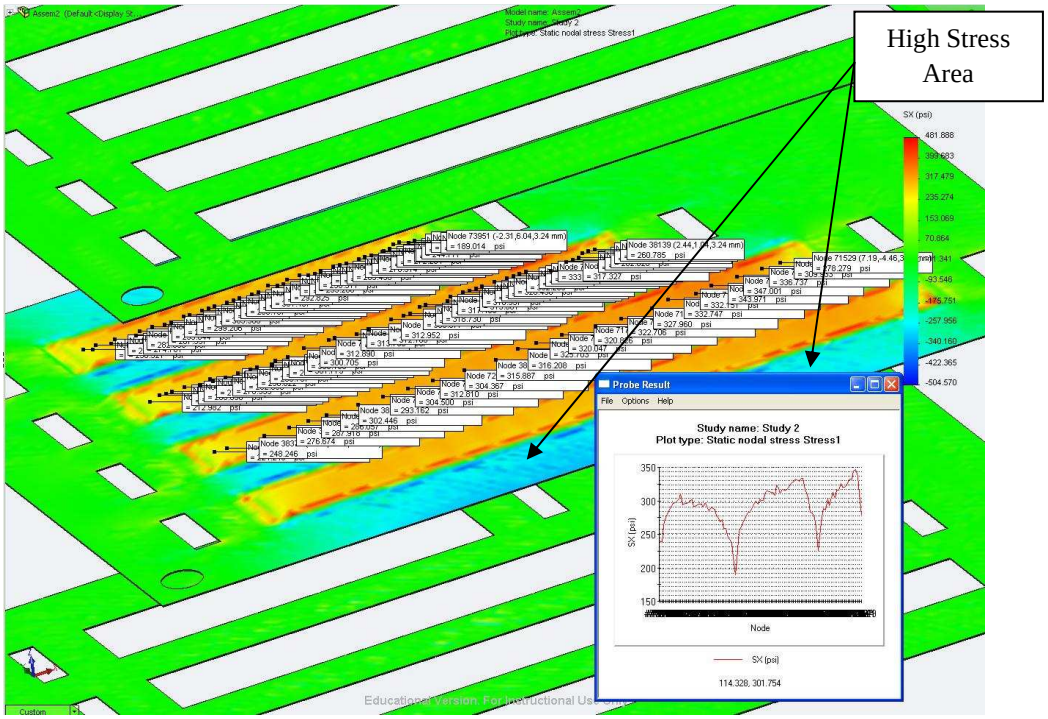

Figure 4-11. Lateral stress distribution when 1000 psi load was applied.

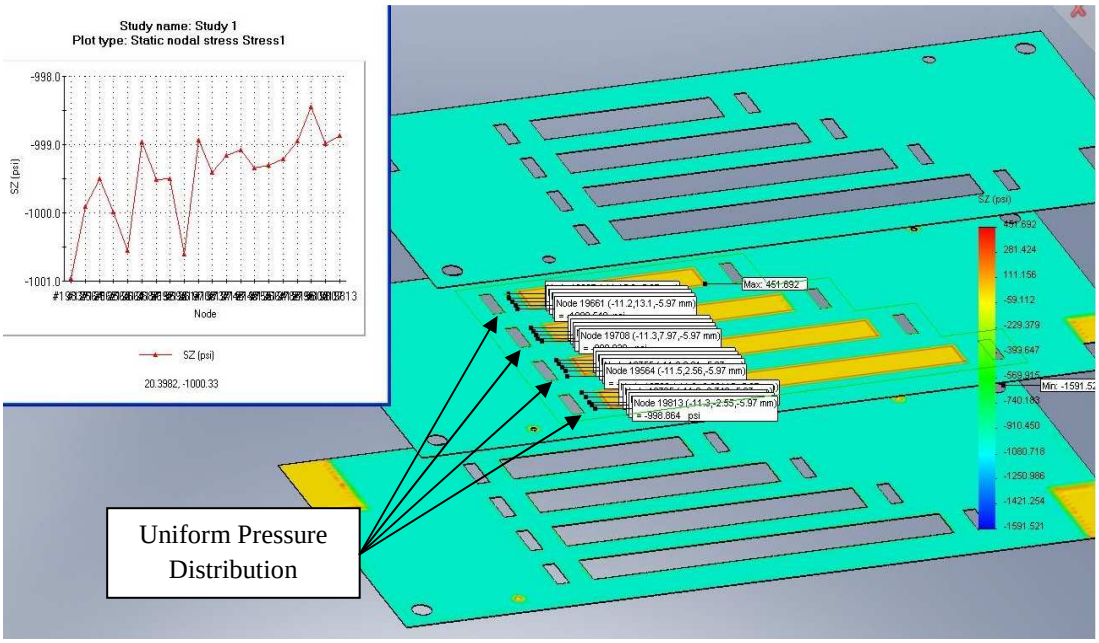

Figure 4-12. Longitudinal stress measurement at the pressured surface on one side of the unsupported column when 1000 psi load was applied.

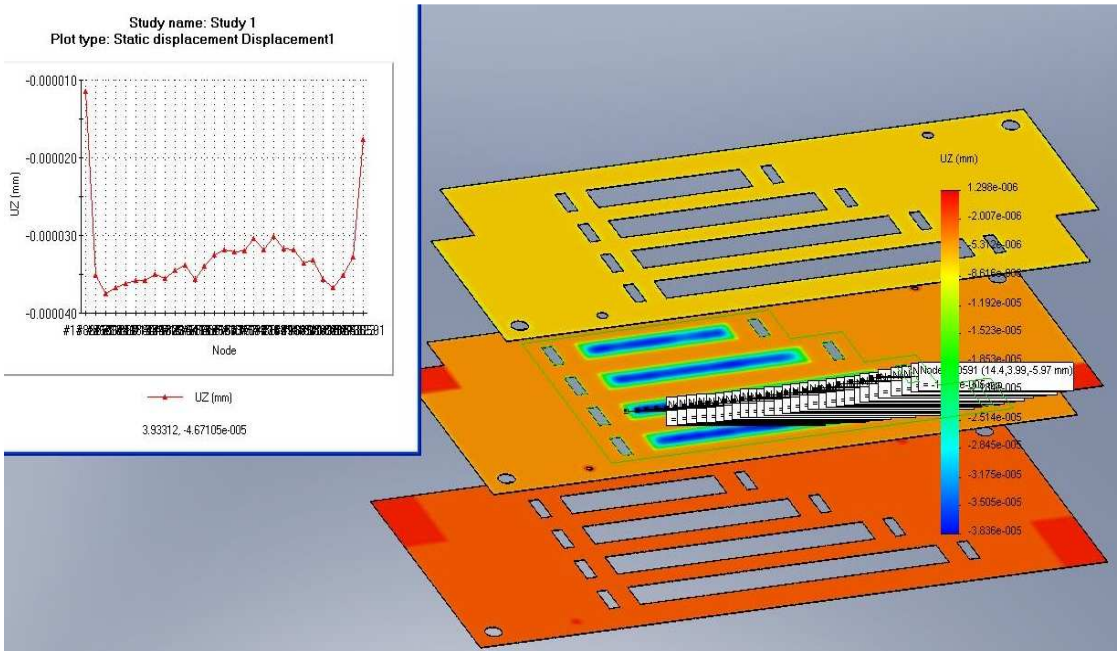

Figure 4-13. Measured displacement in Z-direction when 1000 psi load was applied.

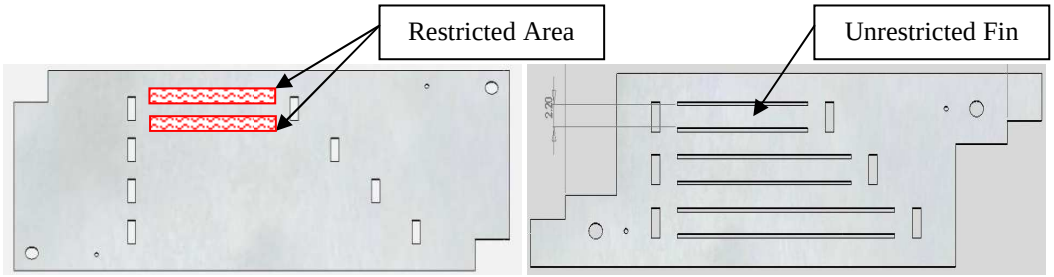

(a) (b)

Figure 4-14. Middle shim design before (a) and after (b) modification.

In addition to the results from the profilometer and FEA, the accuracy and repeatability of the registration procedure was also evaluated. As described previously, registration fiducial features were checked before and pressure applied. Figure 4-15 shows representative result images of the fiducial markings taken by optical microscope for test coupon S2. Since the fiducial markings line width were measured

to be about 20 to 24 µm, according to the results, less than 10 µm misalignments can be achieved using this procedure.

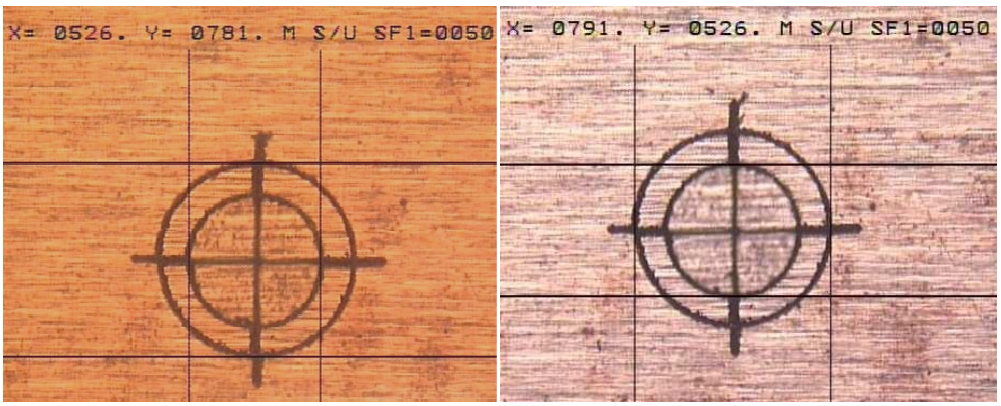

Figure 4-15. Optical images (50X) of the registration features before (a) and after (b) applying pressure (test coupon S2).

4.7 Experimental Approach

Building on the results from the preliminary study, the objective of this step was to validate the mathematical model. Each parameter in the model must be tested individually. According to formula 4-8, the parameters can be separated into two categories. The first category is the materials mechanical properties (*E* and *v*) and the second is the structural properties (*t* and *b*). The mechanical properties can only varied by either switching to another material set or by changing the temperature. In this dissertation, due to manufacturability issues described before in 4.6.1, temperature was used as a parameter to vary the mechanical properties. As for the structural parameters, the length is varied in each test coupon. According to the formula, since the thickness is a squared term, there would be dramatic design change when switching to 25µm (1 mil) or 75µm (3 mil) shim stock. Thus in this dissertation, nitric acid was used to etch the standard shim stock (measured to be 60 µm in thickness) to the thickness of around 50 µm.

To carry out the experiment, the material and the process plan were the same as the preliminary experiment. However, the experimental design and protocol was modified according to the results from the preliminary findings.

4.7.1 Experimental Design Plan

The experimental test plan is listed in Table 4-2. It was separated into two major categories. One was designed to test mechanical parameters and the other was to test structural properties. The reason for separating the design was due to different predicted channel widths when mechanical properties reduced dramatically at elevated temperatures. The test coupons for mechanical tests incorporated five different channel widths while the test coupons for structural tests had three. Both designs incorporates the same registration pin holes and fiducial markings that were successfully implemented in the preliminary design. These features are located on diagonal corners for both horizontal and vertical alignment.

Table 4-2. Experimental test plan

	Sample Number	Test Conditions					Structural Properties						
		Temperature		Pressure (σ_{long})		Pressure Duration	Length (l)	Thickness (t)	Channel Span (b)				
									C1	C2	C3	C4	C5
		°C	°F	MPa	psi	min	mm	mm	mm				
Elastic Modulus & Poisson's Ratio	E1	200.0	392.0	14.38	2085.27	15	2.2	0.061	2.0	4.0	6.0	8.0	10.0
	E2	200.0	392.0	14.38	2085.27	15	2.2	0.061	12.0	13.5	15.0	16.5	18.0
	E3	375.0	707.0	14.38	2085.27	15	2.2	0.061	2.0	4.0	6.0	8.0	10.0
	E4	375.0	707.0	14.38	2085.27	15	2.2	0.061	12.0	13.5	15.0	16.5	18.0
	E5	425.0	797.0	14.38	2085.27	15	2.2	0.061	2.0	4.0	6.0	8.0	10.0
	E6	425.0	797.0	14.38	2085.27	15	2.2	0.061	12.0	13.5	15.0	16.5	18.0
Thickness	T0	21.0	69.8	3.15	456.55	15	2.2	0.050	15.0	20.0	25.0		
	T1	21.0	69.8	5.68	823.77	15	2.2	0.050	15.0	20.0	25.0		
	T2	21.0	69.8	16.89	2449.49	15	2.2	0.050	15.0	20.0	25.0		
	T3	21.0	69.8	28.10	4075.21	15	2.2	0.050	15.0	20.0	25.0		
	T4	21.0	69.8	39.31	5700.94	15	2.2	0.050	15.0	20.0	25.0		
Width	S1	21.0	69.8	3.15	456.55	15	2.2	0.061	15.0	20.0	25.0		
	S2	21.0	69.8	5.68	823.77	15	2.2	0.061	15.0	20.0	25.0		
	S3	21.0	69.8	16.89	2449.49	15	2.2	0.061	15.0	20.0	25.0		
	S4	21.0	69.8	28.10	4075.21	15	2.2	0.061	15.0	20.0	25.0		
	S5	21.0	69.8	39.31	5700.94	15	2.2	0.061	15.0	20.0	25.0		
	S6	21.0	69.8	50.52	7326.66	15	2.2	0.061	15.0	20.0	25.0		
	S7	21.0	69.8	61.72	8952.39	15	2.2	0.061	15.0	20.0	25.0		

4.7.1.1 Design for Mechanical Parameters (E and v)

The mechanical properties of copper alloys decrease dramatically when subjected to high temperatures (see Table 4-3). Due to this reason, according to formula 4-8, the width of the fin structures needs to be reduced substantially. After searching through the literature and materials handbooks, the mechanical data for copper alloy C11000 when subjected to elevated temperature could not be found. Thus the elastic modulus values used in this experiment were extrapolated using empirical results reported for copper alloy C10200 (Upthegrove and Burghoff, 1956). Both alloys have more than 99.9% copper composition (weight) thus it is assumed that the

mechanical properties would behave similar to C11000 when subjected to elevated temperature.

Because of the uncertainty of the mechanical properties of the test articles, a wide range of fin lengths were used. The detailed specifications and dimensions are listed in the engineering drawings (Appendix J). The dimensions of the test coupons were 1.4 inches by 2.3 inches and had an actual area of 1.746 inch^2. Each test coupon incorporates five different fin structure lengths. Sample E1, E3, and E5 have fin length of 2, 4, 6, 8, and 10 mm. Sample E2, E4, E6 have fin length of 12, 13.5, 15, 16.5, and 18 mm. All samples were subjected to same compressive pressure (2085.27 psi) in order to evaluate the effect of mechanical parameters. Different mechanical parameters were generated using three different process temperatures (200, 375, and 425°C). Under those temperatures, the corresponding elastic modulus values were calculated to be 98.69, 13.92, and 2.00 GPa, respectively. Shown in Figure 4-16, the test coupon design still incorporates the same registration pin holes and fiducial markings in diagonal corners as the preliminary test coupon design.

Table 4-3. Empirical data reported from Upthegrove and Burghoff, 1956.

C12200 at Elevated Temperature		
Test Temperature		Elastic Modulus
°C	°F	(GPa)
24	75	114
60	140	109
100	212	119
149	300	108
204	400	102
288	550	103
371	700	74
454	850	55

C10200 at Elevated Temperature		
Test Temperature		Elastic Modulus
°C	°F	(GPa)
24	75	116
100	212	117
204	400	98

4.7.1.2 Design for Structural Parameters (b and t)

Shown in Figure 4-16, the test coupon design for fin length tests was modified based on the results from preliminary study. For detailed specifications and dimensions, please refer to the engineering package in Appendix I. The test coupon dimension is 0.75 inch by 2.31 inches and has an actual surface area of 0.968 inch^2. Each test coupon incorporates three different fin structures having length of 15, 20, and 25 mm. The length of the fin is based on the mathematical model (formula 4-8) and the material properties at room temperature. The major design change is added through cut features along the side of the middle lamina fin structure to allow buckling to progress.

For fin thickness tests, same test coupon design was used. However, the thickness of the middle lamina was reduced from 61 µm to 50 µm. According to formula 4-8, this 20% reduction in thickness would reduce the critical buckling load limit by 36%.

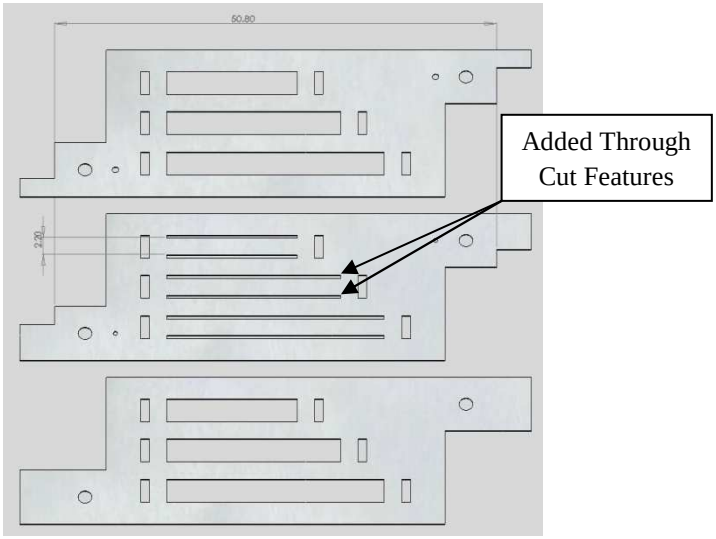

Figure 4-16. Design of test coupon for structural properties testing

4.7.2 Experimental Test Protocol

Each test coupon was stacked then registered using the registration pins. The sample was taped on both ends to prevent any movement which might cause mis-registration. The pins were then removed so the sample can fit between the ceramic fixtures shown in Figure 4-17. Afterward, the fiducial markings were checked using optical microscope. If the fiducial markings were not connected, the sample was logged as mis-registered and discarded. Once the sample passed the initial inspection, the test coupon was then pressed using a hydraulic press. To ensure the force readout on the hydraulic pressure was calibrated, a stainless steel compression load cell (OMEGA part number LC304-5K) was used. The range for the load cell is 0-5000 lbs with accuracy (linearity, hysteresis, repeatability combined) of ± 25 lbs. Measurements were taken right when the hydraulic press was turned on, and then measured again after running for 60 minutes. This was to ensure the hydraulic oil is warmed up thus prevent fluctuations of pressure during actual testing.

After applying pressure, the fiducial markings were then re-checked to ensure the test sample was still aligned. The sample was then moved to the profilometer station to scan for warpage. Each fin structure was scanned three times and the peak-to-valley distance was recorded (shown in Figure 4-18). Since each parameter of the mathematical model was evaluated separately, additional test procedures were required. These additional protocols are described in the following paragraphs.

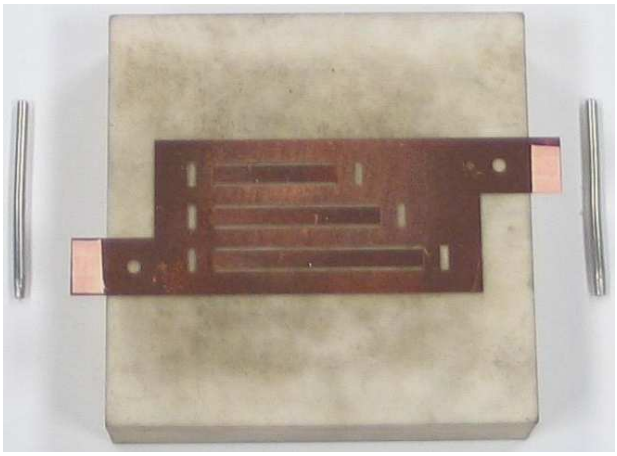

Figure 4-17. Actual image of the test coupon after registration and taping.

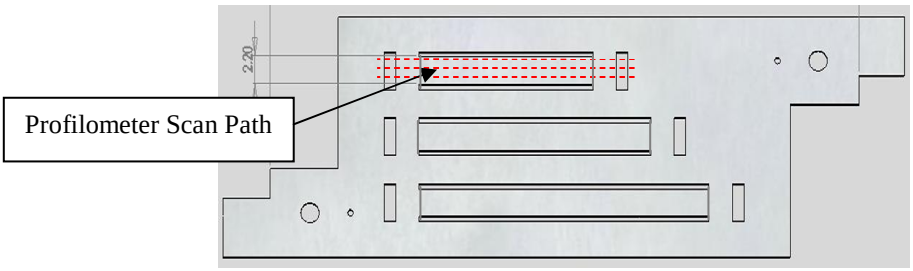

Figure 4-18. The profilometer scan paths for one of the fin structures.

4.7.2.1 Protocol for Testing Structural Parameter: Width (b)

Since the width of the fin structure is critical in these tests, additional scan length for surface profilometer was implemented. After each scan, the width of the fin structure can be confirmed. Figure 4-19 shows one of the profile scanned result and location of the width measurement.

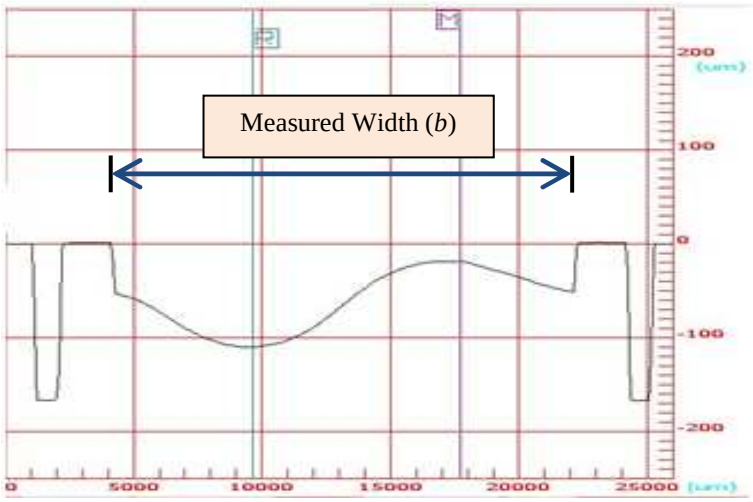

Figure 4-19. Microchannel width measured using surface profilometer results.

To validate the length parameter in the formula, seven samples were generated. Each sample was applied under different loads to simulate different diffusion bonding conditions. The loads used in this experiment are 442, 797, 2371, 3946, 5520, 7094, and 8668 pounds (lbs). During testing, the load was continuously applied for 15 minutes. The induced Poisson's lateral stresses are 157, 283, 840, 1398, 1955, 2513 and 3071 pounds per square inch (psi) which would generate seven data points for each microchannel width. Though preliminary results show uniform pressure distribution throughout the surface, Fuji pressure sensor films (Low Pressure LW film which operates between 363 and 1450 psi) were again used to confirm.

4.7.2.2 Protocol for Testing Structural Parameter: Thickness (t)

To reduce the thickness by 20%, the shim stock material was etched using diluted nitric acid. To estimate the thickness reduction, the weight of the shim stock was measured before and after laser patterning. In this experiment, twelve pieces of shim stock were etched then three of them were laser machined with the design

described previously. Total of five sets of test coupons were manufactured. Each sample was exposed to the same loads that were applied from structural width study. In this case, the loads used are 442, 798, 2372, 3946, and 5520 pounds (lbs). During testing, the load was continuously applied for 15 minutes. The induced Poisson's lateral stresses were 157, 283, 840, 1398, and 1955 pounds per square inch (psi). This generates four additional data points to be plotted with the result from length testing.

Since the thickness of the fin structure was critical in these tests, additional measurement was implemented. By utilizing the surface profilometer, the thickness of the laminae can be estimated. In addition, traditional micrometers were used to validate the results obtained from surface profilometer (shown in Figure 4-20).

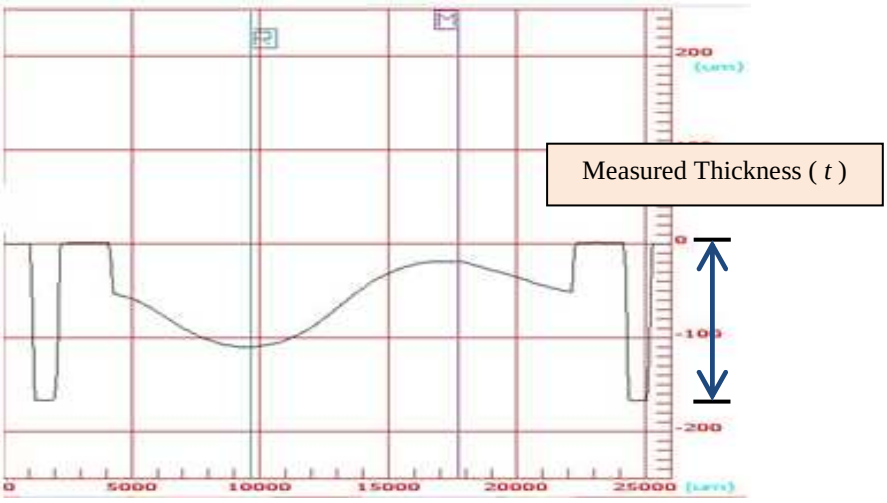

Figure 4-20. Thickness of the test coupon measured from surface profilometer result.

4.7.2.3 Calibration of pressure distribution.

To ensure uniform compressive pressure was applied on the test coupons, an additional test coupon was tested using the Fuji film. The results show uniform pressure distribution throughout the test coupon (shown in Figure 4-21).

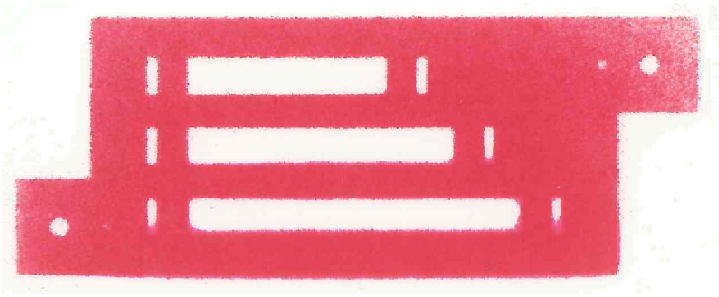

Figure 4-21. Fuji film pressure distribution result

4.8 Results and Discussion

The results for structural and mechanical parameters are explained in the subsequent paragraphs.

4.8.1 Results from Structural Parameter: Channel Width (*b*)

Profilometry results for room temperature studies are plotted in Figure 4-22. The rectangular markers indicate the parallelism of the test article fin measured before being subjected to compressive pressure while the triangle markers indicate the parallelism after applying pressure. The vertical indicates maximum theoretical pressure limit calculated using formula (4-9). In general, the figures show overall agreement with the model suggesting that buckling due to Poisson ratio effects is

possible. The results for the 15 mm channel widths show deviations from the model for S3, S5 and S6.

Samples S5 and S6 suggest that little deformation occurred within the fins even when the buckling force exceeded the critical limit for buckling. However, investigation of the surface profiles for these samples suggest a multimode buckling behavior that would reduce the measurable deflection. (shown in Figure 4-23). Sample S3 suggests that significant buckling occurred below the critical buckling force. Investigations are being made to determine if this is due to grain size effects.

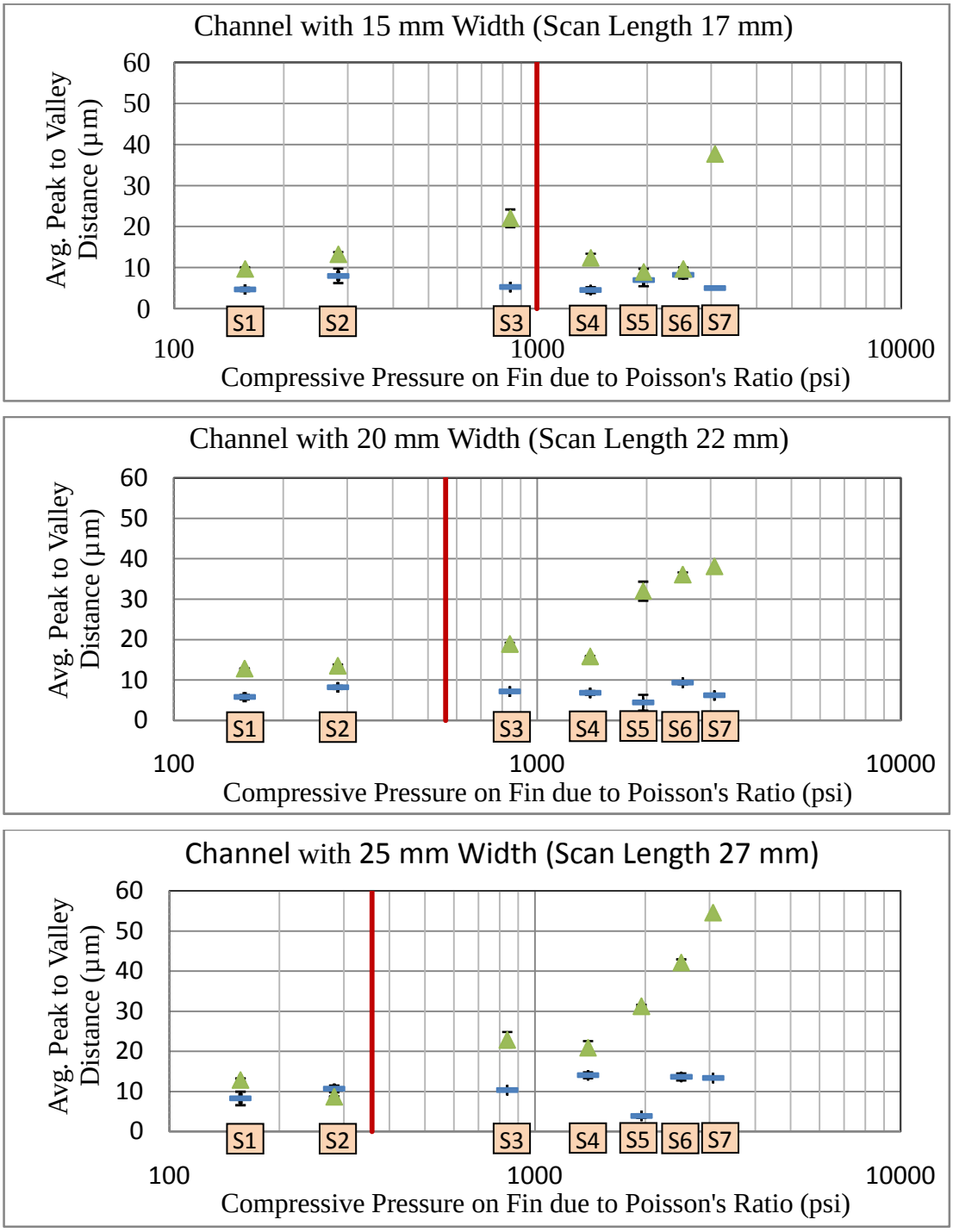

Figure 4-22. Test results plotted against 15 (top), 20 (middle), and 25 mm (bottom) channel width. The red line indicates maximum theoretical pressure limit.

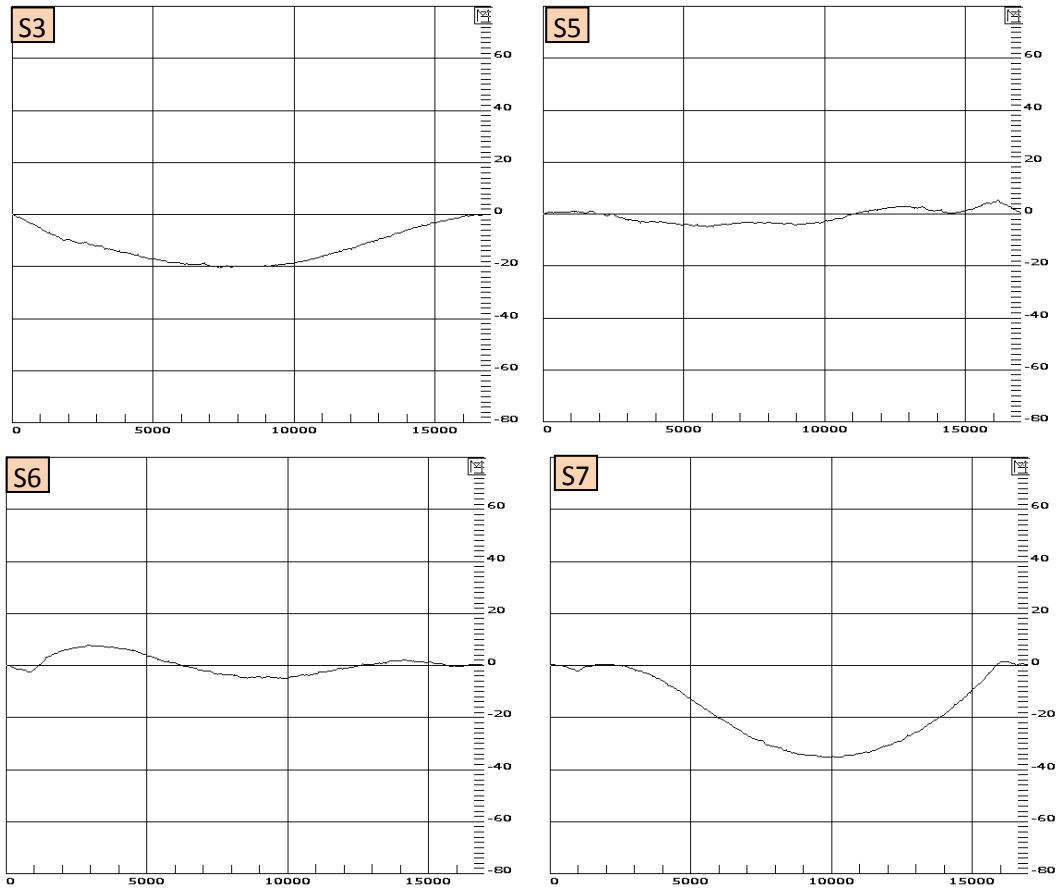

Figure 4-23. Results of surface profile for S3, S5, S6, and S7 after subjected to compressive pressure.

4.8.2 Results from Structural Parameter: Thickness (*t*)

Profilometry results for room temperature studies of foils reduced in thickness by etching are plotted in Figure 4-24. The hollow rectangular markers indicate the parallelism of the fin measured before it was subjected to compressive pressure while the hollow triangle markers indicate the parallelism after pressure. The red line indicates maximum theoretical pressure limit calculated using formula (4-9). From the figures, all samples except T1 were buckled after applying compressive pressure suggesting poor alignment between empirical and theoretical results. Upon further

investigation, the centerline average surface roughness (see Appendix E) for samples used in the previous section was found to be 0.18 µm. Samples used in this section were etched to allow for a reduction in thickness. Consequently, the centerline average roughness of etched samples was found to be 1.19µm (shown in Figure 4-25). This suggests average peak-to-valley surface variation on the order of 4.5 µm for the etched samples. This variation of surface roughness on both sides could provide as much as 18% variation in thickness across the foil. According to formula (3-9), the thickness of the fin has squared impact on the critical bonding stress. Furthermore, it is likely that such pronounced roughness acted as notches in fins reducing the buckling resistance of the foil.

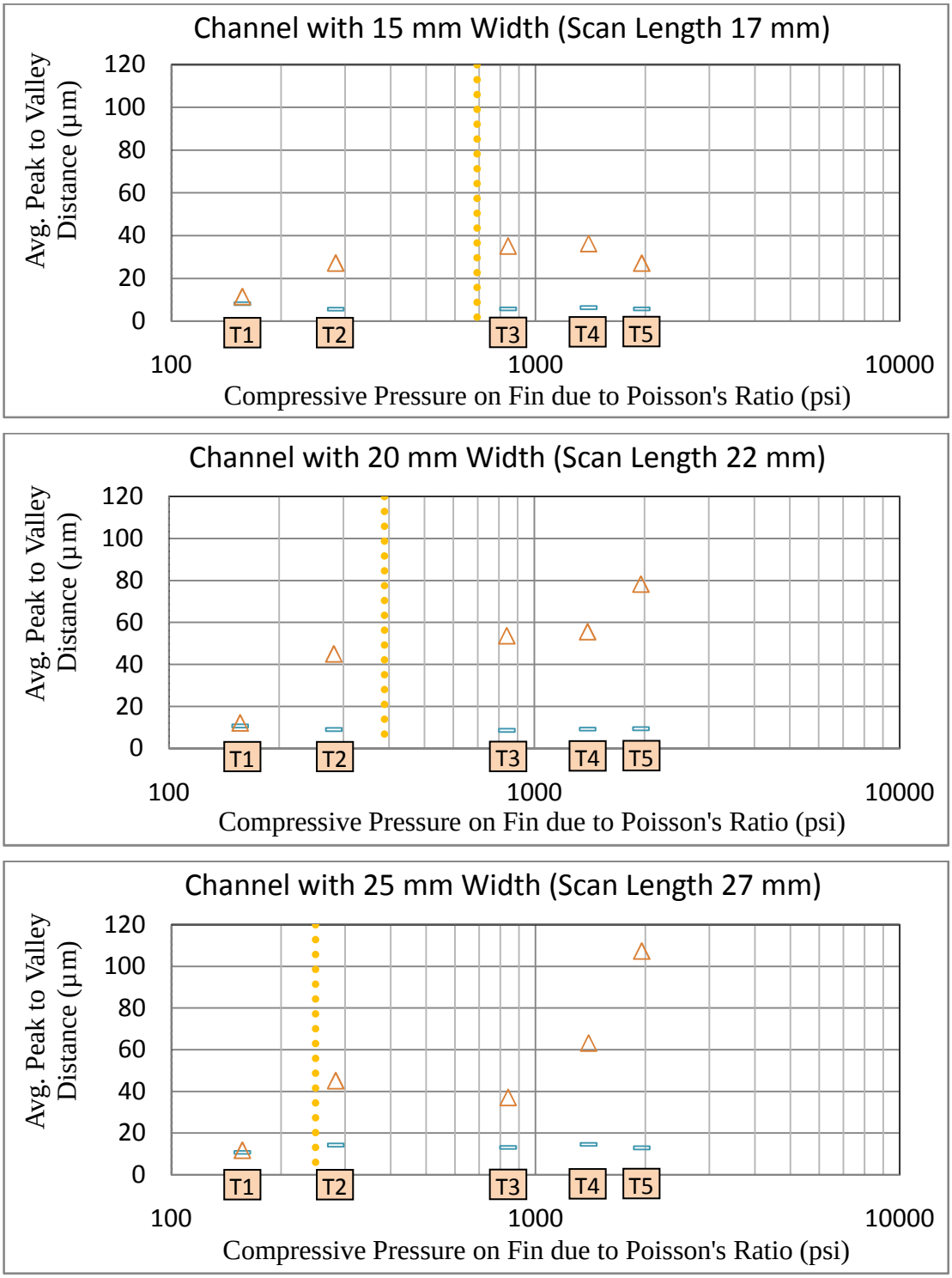

Figure 4-24. Test results plotted against 15, 20, and 25 mm fin structures. The red line indicates maximum theoretical pressure limit from the formula

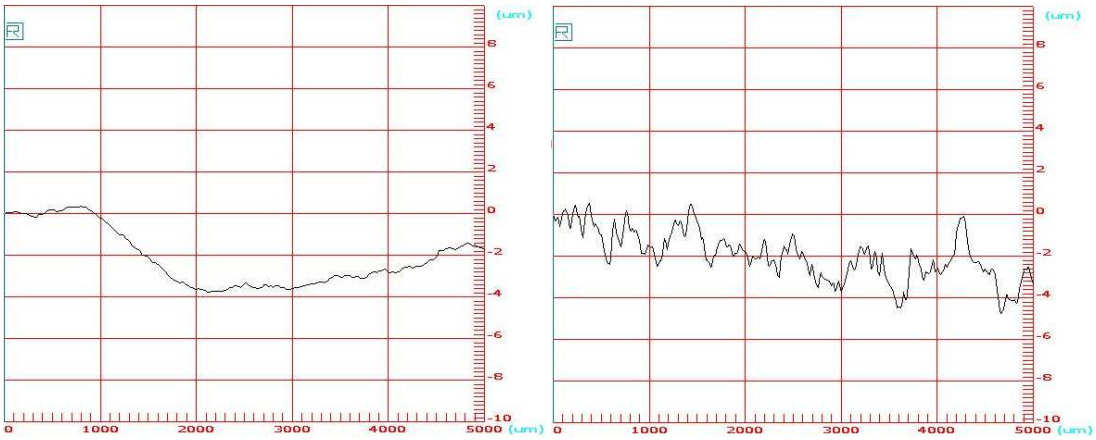

Figure 4-25. Surface profile taken from flattened (left) and etched (right) sample.

4.8.3 Results from Mechanical Parameters: Elastic Modulus (*E*) and Poisson's Ratio (*ν*)

Profilometry results for studies above room temperature are plotted in Figure 4-26. The parallelism of foils in this experiment was plotted against the width of the channel since the compressive pressure and the fin thickness were fixed. The rectangular markers indicate the parallelism of the fin measured before it was subjected to compressive pressure while the X markers indicate the parallelism after pressure. Red lines indicate maximum theoretical channel widths calculated using formula (4-9).

The results for the 375°C and 425°C conditions show within 20% error from the model. However, results for the 200°C samples (E1 and E2) show departure from the model. Calculations for the critical limit had around 50% error. These errors might be due to the poor estimation of the elastic modulus value using empirical data. In the future, micro-tensile testing would be needed to validate the actual mechanical properties at elevated temperatures.

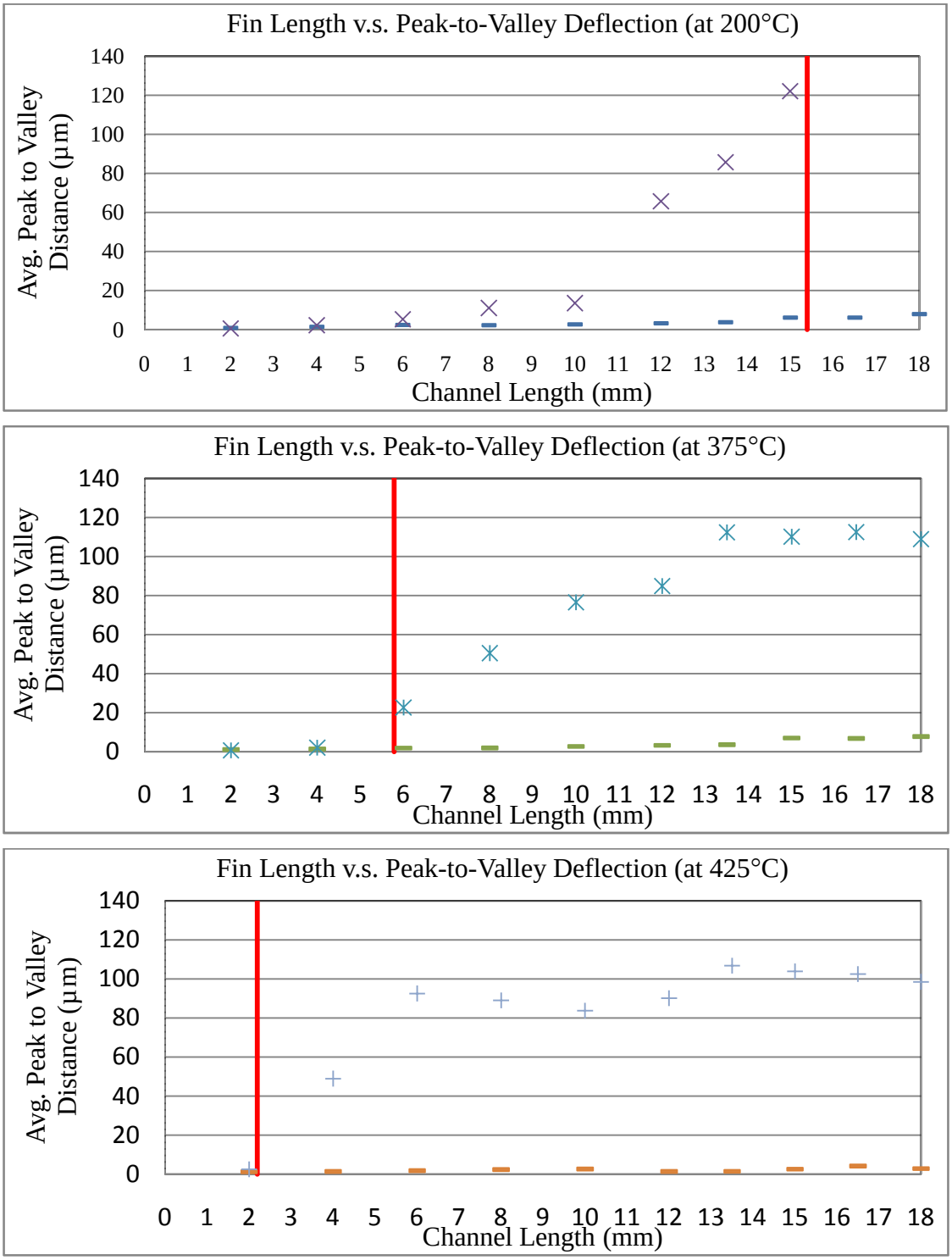

Figure 4-26. Test results plotted using 200 (top), 375 (middle), and 425°C (bottom). The red line indicates maximum theoretical channel width from the formula

4.9 Result Implications

The results from the experiment data show good agreement with the theoretical model. To further validate the theoretical model, experimental results from previous publication were used (Pluess and Paul, 2007). Detailed test coupon design is shown in Appendix K. From the publication, critical parameters are as follows:

$E = 1.00 \times 10^{9}$ [N/m^2] (at 800°C)

$v = 0.343$ (at room temperature)

$t = 2.03 \times 10^{-4}$ [m]

$\sigma_{long} = 6.00 \times 10^{6}$ [N/m^2]

By applying the theoretical model derived in this study, the theoretical buckling length is calculated to be 8.12 mm. Since the channel span used in the publication was 4mm, it is expected that the channel would not buckle after diffusion bonding (as shown in Figure 4-27)

Figure 4-27. Metallography results from Pluess's publication (Pluess and Paul, 2007).

The theoretical model was also applied on the actual device described in 4.3. From Figure 4-2, the structural data were obtained. In addition, the process parameter was obtained from Aerospace Structural Metals Handbook. At diffusion bonding temperature, the Young's modulus was 1.03×10^{6} N/m^2 and the Poisson's ratio was 0.28. Given that the bonding pressure was 1.38×10^{7} N/m^2, the critical buckling length was calculated to be around 11 mm. Comparing this value with the inlet and outlet

channel span (Figure 4-2), it was found that the results agrees with the model having no warpage at the inlet (3.3 mm span) while showing warpage at the outlet (37 mm span).

From the discussion above, it is expected that the theoretical model is capable of predicting warpage due to Poisson's ratio. However, the Young's modulus data must be obtained at respective temperature.

4.10 Summary

The identification of warpage mechanisms within arrayed microchannel structures is important to prevent flow maldistribution. A new warpage mechanism has been identified caused by the buckling of channel fins due to lateral stresses induced via Poisson's ratio. A critical compressive stress limit formula had been developed. Empirical results show generally good agreement. The critical limit can be predicted based on key mechanical properties (elastic modulus and Poisson's ratio) and dimensions (channel width and thickness). The implication of this formula for typical arrayed microchannel fabrication is that the critical channel span needs to be identified when transitioning from the header to microchannels and vice versa.

4.11 References

Aerospace Structural Metals Handbook, Columbus, Ohio: Mechanical Properties Data Center, Battelle Columbus Laboratories, 1970

Alfutov, N. A., translated by Evseev, E., Balmont, V. B., *Stability of Elastic Structure*s, Berlin; New York: Springer, 2000.

Bloom F., Coffin, D., *Handbook of Thin Plate Buckling and Post-Buckling*, Boca Raton, FL: Chapman & Hall/CRC, 2000.

Budynas, R. G., Young, W. C., *Roark's formulas for stress and strain*, McGraw-Hill Professional; 7th edition, 2001

Carr, S. M., Lawrence, W. E., Wybourne, M. N., "Static buckling and actuation of free-standing mesoscale beams," *IEEE Transactions on Nanotechnology*, Vol. 4, n 6, pp. 655-659, 2005

Davis J. R., *Metals Handbook*, Materials Park, Ohio : ASM International, 1998

Ehrfeld W., Hessel V., and Lowe H., *Microreactors: New Technology for Modern Chemistry*, Weinheim ; New York : Wiley-VCH, 2000

Fang, W., Wickert, J.A., "Post-buckling of micromachined beams," *Journal of Micromechanics and Microengineering*, Vol. 4, n 3, pp. 116-122, 1994.

Fang, W. -L., Lee, C. -H. , Hu, H. -H., "On the buckling behavior of micromachined beams," *Journal of Micromechanics and Microengineering*, Vol. 9, n 3, pp. 236-244, 1999

Hearn, E. J., *Mechanics of Materials: An Introduction to the Mechanics of Elastic and Plastic Deformation of Solids and Structural Components*, Oxford, OX, England ; New York : Pergamon Press, 1985.

Luo, C., Francis, A., Liu, X.-C., "Determination of compressive residual stress in a doubly-clamped microbeam according to its buckled shape," *Microelectronic Engineering*, Vol. 85, n 2, pp. 339-347, 2008

Martin, P. M., Matson, D. W., Bennett, W. D., Stewart, D. C., Lin, Y., "Laser micromachined and laminated microfluidic components for miniaturized thermal, chemical and biological systems," *Proceedings of SPIE - The International Society for Optical Engineering*, Vol. 3680, n. 2, pp. 826-833, 1999.

Martin, M. J., White, R. D., Kurabayashi, K., Boyd, I. D., "Fabrication of beam structures with micro-scale cross-sections and meso-scale spans," *Journal of Micromechanics and Microengineering*, Vol. 17, n 12, pp. 2516-2521, 2007

Matson, D. W., Martin, P. M., Bennett, W. D., "Laser machined components for microanalytical and chemical separation devices," *Proceedings of SPIE - The International Society for Optical Engineering*, Vol. 3519, pp. 200-207, 1998.

Paul, B. K., Dewey, T., Alman, D., and Wilson, R. D., "Intermetallic Microlamination for High-Temperature Reactors," presented at *4th International Conference on Microreaction Technology*, Atlanta, GA, 2000.

Pluess, C., Paul, B. K., "Application of controlled thermal expansion in microlamination for the economical production of bulk microchannel systems," *Chemical Engineering Communications*, Vol. 194, n 9, pp. 1259-1270, 2007

Templin, R. L. et al., *Properties of Metals in Materials Engineering*, Cleveland, 1948

Ugural, A. C., *Mechanics of Materials*, Hoboken, N.J. : Wiley ; Chichester : John Wiley [distributor], 2008.

Upthegrove, C. and Burghoff, H. L., *Elevated-Temperature Properties of Coppers and Copper-Base Alloys*, ASTM Special Technical Publication No. 181, ASTM, Philadelphia, PA

Zipperian, D. C., *Metallographic Specimen Preparation Basics*, Pace Technologies, http://www.metallographic.com/Technical/Basics.pdf

CHAPTER 5

Conclusions

Microchannel technologies have much to offer to the field of nanomanufacturing. In ceria synthesis, microchannel mixers yielded different nanoparticle morphologies. XPS study showed that the nanoparticles synthesized using microchannel Tee-mixer yielded more Ce^{3+} molecules. This indicates that the Tee-mixer approach permitted the formation and capture of an unstable intermediate $Ce(OH)_3$ molecule by shielding the intermediate from exposure to the oxygen environment. Applications such as anti-reflective coatings are currently under research.

In second part of this study, main sources of mechanically induced warpage/flow maldistribution were summarized. To avoid unsupported regions within the microchannel structure, FEA software can be facilitated. Annealed materials need to be selected to minimize build-in internal stresses. In addition, careful considerations must be taken to prevent introduction of stresses during machining. According to preliminary study, the load on mis-registration model needs to be modified as non-uniform pressure. Thermal gradient would affect the microchannel structure. However, it can be minimized by reducing the ramping rate. Finally, machining burrs needs to be removed in order to efficiently diffusion bond the laminae and to prevent device leakage.

In the last part of this study, a new warpage mechanism has been identified caused by the buckling of channel fins due to lateral stresses induced via Poisson's ratio. A critical compressive stress limit formula had been developed. Empirical results show generally good agreement. The critical limit can be predicted based on key mechanical properties (elastic modulus and Poisson's ratio) and dimensions (channel width and thickness). This formula was also compared to previous publications and devices

designed and manufacturing in the lab. The implication of this formula for typical arrayed microchannel fabrication is that the critical channel span needs to be identified when transitioning from the headers to the microchannels and vice versa.

APPENDICES

APPENDIX A

EDS Results of Batch Mixer from Experiment (i)

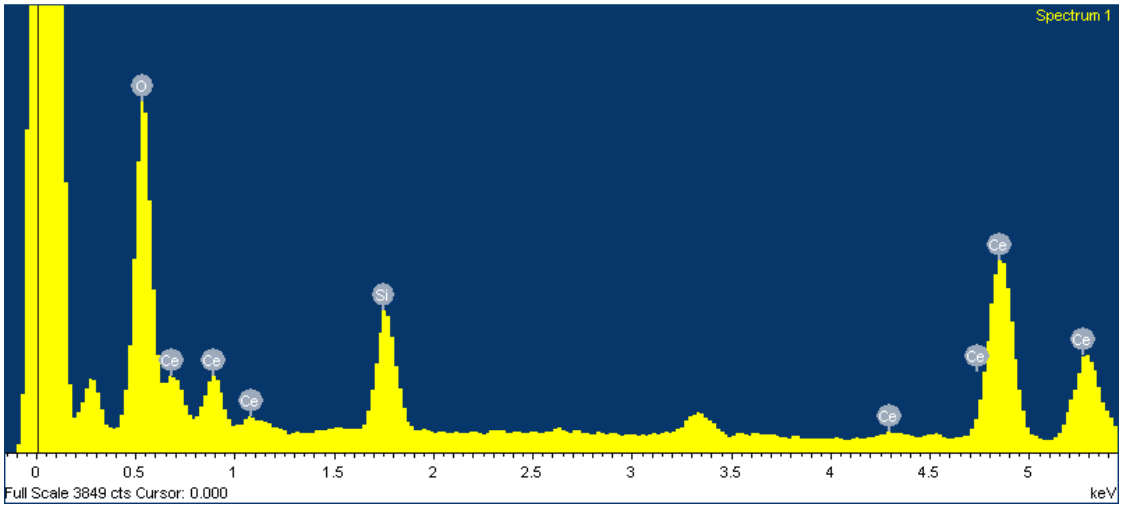

Spectrum processing :
Peaks possibly omitted : 3.325, 8.626, 11.640 keV

Processing option : All elements analyzed (Normalised)
Number of iterations = 3

Standard :
O SiO2 1-Jun-1999 12:00 AM
Si SiO2 1-Jun-1999 12:00 AM
Ce CeO2 1-Jun-1999 12:00 AM

Element	App Conc.	Intensity Corrn.	Weight%	Weight% Sigma	Atomic%
O K	27.39	1.7188	25.18	0.43	68.53
Si K	3.27	0.7791	6.64	0.20	10.29
Ce L	40.10	0.9294	68.18	0.46	21.18
Totals			100.00		

EDS Results of Batch Mixer from Experiment (ii)

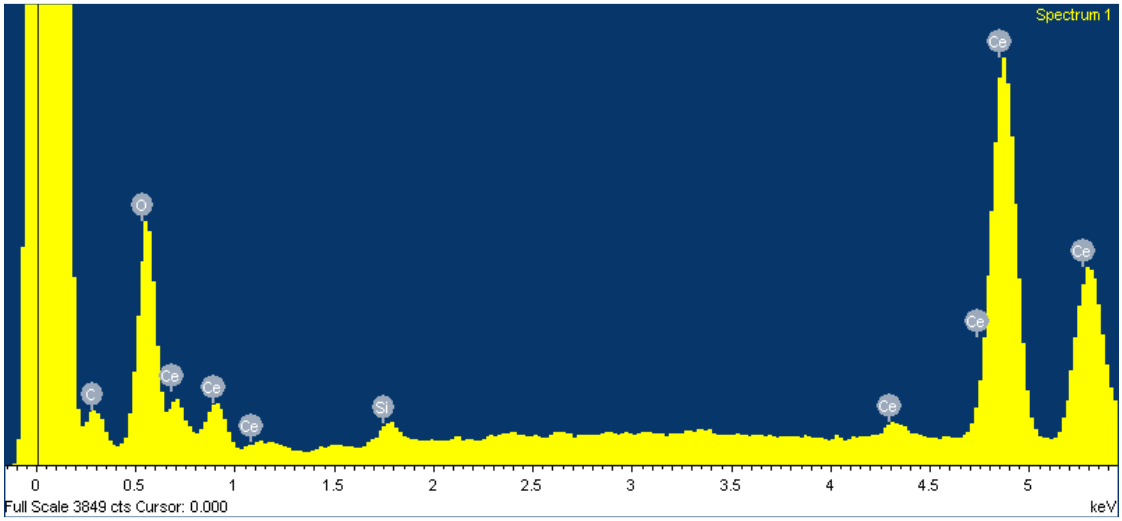

Spectrum processing :
No peaks omitted

Processing option : All elements analyzed (Normalised)
Number of iterations = 3

Standard :
C CaCO3 1-Jun-1999 12:00 AM
O SiO2 1-Jun-1999 12:00 AM
Si SiO2 1-Jun-1999 12:00 AM
Ce CeO2 1-Jun-1999 12:00 AM

Element	App Conc.	Intensity Corrn.	Weight%	Weight% Sigma	Atomic
C K	-1.13	0.8332	-2.14	0.49	-15.73
O K	10.86	1.6957	10.12	0.28	55.79
Si K	0.38	0.7390	0.81	0.10	2.53
Ce L	58.99	1.0225	91.22	0.53	57.41
Totals			100.00		

EDS Results of Tee-mixer from Experiment (i)

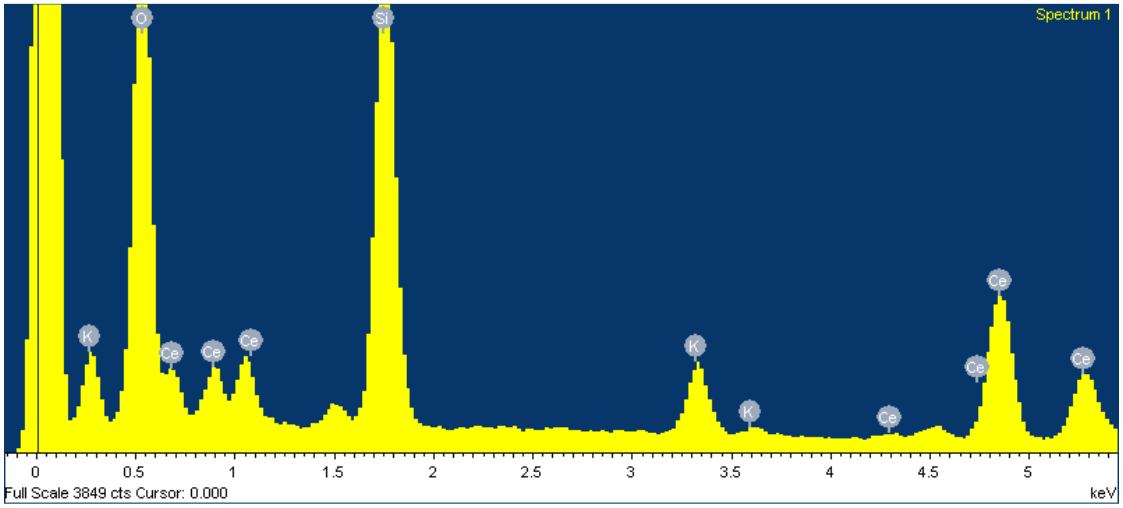

Spectrum processing :
Peak possibly omitted : 8.619 keV

Processing option : All elements analyzed (Normalised)
Number of iterations = 3

Standard :
O SiO2 1-Jun-1999 12:00 AM
Si SiO2 1-Jun-1999 12:00 AM
K MAD-10 Feldspar 1-Jun-1999 12:00 AM
Ce CeO2 1-Jun-1999 12:00 AM

Element	App Conc.	Intensity Corrn.	Weight%	Weight% Sigma	Atomic
O K	37.59	1.4620	37.07	0.39	69.10
Si K	10.84	0.8556	18.28	0.23	19.41
K K	2.83	1.1301	3.61	0.13	2.75
Ce L	23.84	0.8376	41.04	0.44	8.74
Totals			100.00		

EDS Results of Tee-mixer from Experiment (ii)

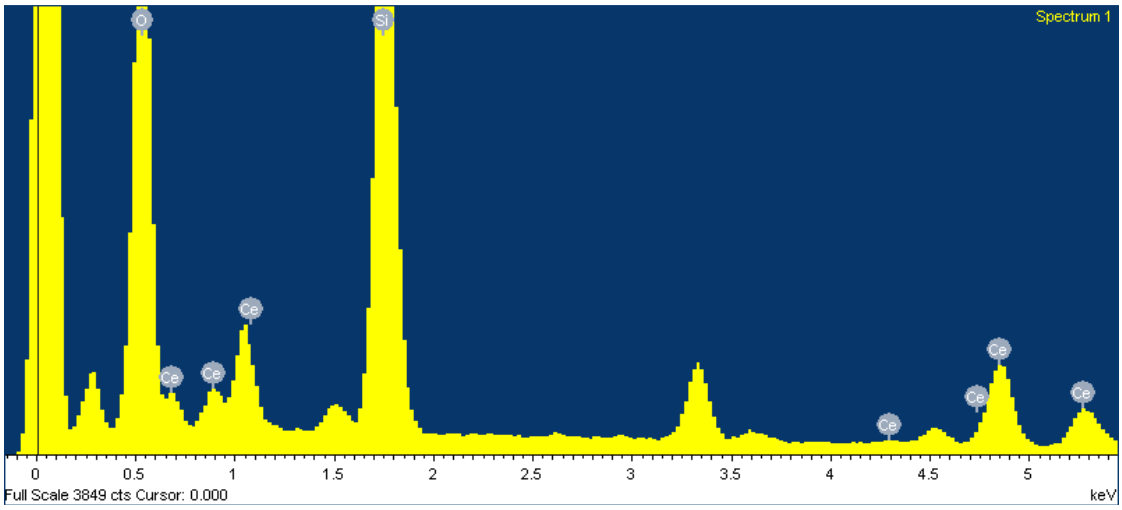

Spectrum processing :
Peaks possibly omitted : 3.320, 3.607, 8.638, 9.598 keV

Processing option : All elements analyzed (Normalised)
Number of iterations = 3

Standard :
O SiO2 1-Jun-1999 12:00 AM
Si SiO2 1-Jun-1999 12:00 AM
Ce CeO2 1-Jun-1999 12:00 AM

Element	App Conc.	Intensity Corrn.	Weight%	Weight% Sigma	Atomic%
O K	44.43	1.5259	45.47	0.42	71.11
Si K	15.52	0.9011	26.89	0.29	23.96
Ce L	14.13	0.7984	27.63	0.48	4.93
Totals			100.00		

APPENDIX B

EDX Results of Batch Mixer

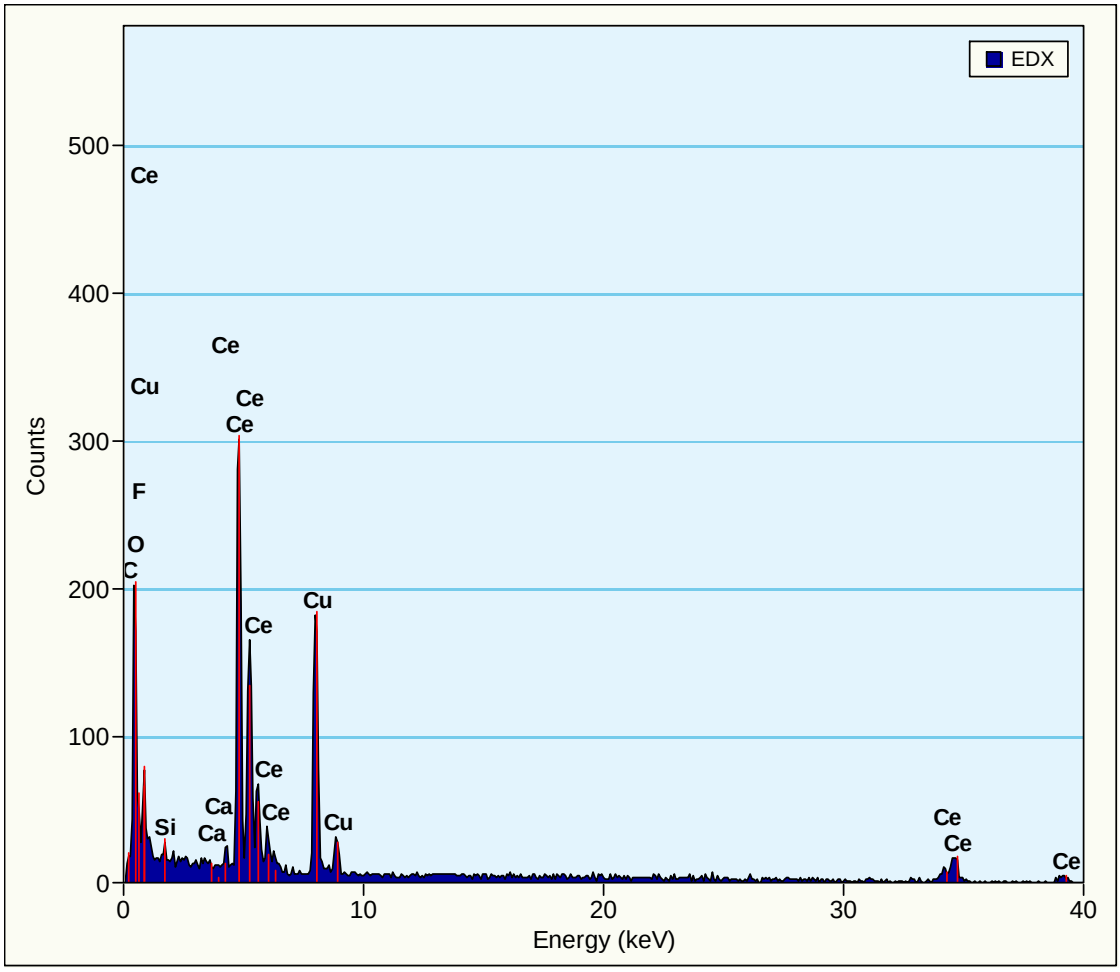

EDX Results of Tee-Mixer

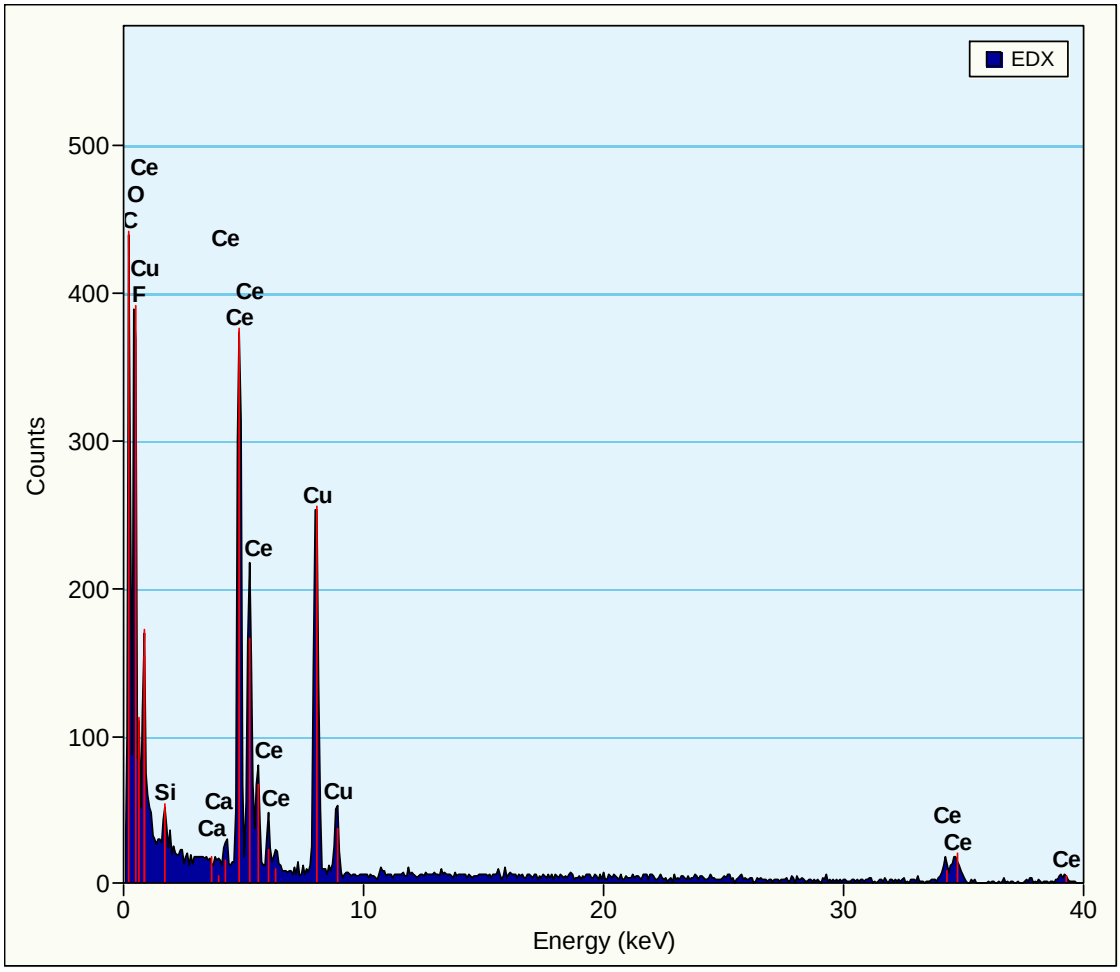

APPENDIX C

Numerical Solution for Mis-registration (a)

$$2P(a)^3 - 2PW_c(a)^2 + \frac{1}{6}W_c\frac{\sigma_y}{6}t^2 = 0$$

Assume

A = $2P$

B = $-2P \cdot W_c$

C = $\frac{1}{6}W_c\frac{\sigma_y}{6}t^2$

Solution 1 = 1/6/A*(-108*C*A^2+8*B^3+12*3^(1/2)*(C*(27*C*A^2-4*B^3))^(1/2)*A)^(1/3)+2/3*B^2/A/(-108*C*A^2+8*B^3+12*3^(1/2)*(C*(27*C*A^2-4*B^3))^(1/2)*A)^(1/3)+1/3*B/A

Solution 2 = -1/12/A*(-108*C*A^2+8*B^3+12*3^(1/2)*(C*(27*C*A^2-4*B^3))^(1/2)*A)^(1/3)-1/3*B^2/A/(-108*C*A^2+8*B^3+12*3^(1/2)*(C*(27*C*A^2-4*B^3))^(1/2)*A)^(1/3)+1/3*B/A+1/2*i*3^(1/2)*(1/6/A*(-108*C*A^2+8*B^3+12*3^(1/2)*(C*(27*C*A^2-4*B^3))^(1/2)*A)^(1/3)-2/3*B^2/A/(-108*C*A^2+8*B^3+12*3^(1/2)*(C*(27*C*A^2-4*B^3))^(1/2)*A)^(1/3))

Solution 3 = -1/12/A*(-108*C*A^2+8*B^3+12*3^(1/2)*(C*(27*C*A^2-4*B^3))^(1/2)*A)^(1/3)-1/3*B^2/A/(-108*C*A^2+8*B^3+12*3^(1/2)*(C*(27*C*A^2-4*B^3))^(1/2)*A)^(1/3)+1/3*B/A-1/2*i*3^(1/2)*(1/6/A*(-108*C*A^2+8*B^3+12*3^(1/2)*(C*(27*C*A^2-4*B^3))^(1/2)*A)^(1/3)-2/3*B^2/A/(-108*C*A^2+8*B^3+12*3^(1/2)*(C*(27*C*A^2-4*B^3))^(1/2)*A)^(1/3))

APPENDIX D

Measuring Equipment Summaries

Optical Microscope and Video Measurement Systems

Misalignment and fin geometry were measured by a LEICA DML microscope and a video measurement system (VIA-100). The entire system provides flexibility and accuracy for specimen's dimensional inspection because its features include X, Y or point to point measurement, an easy calibration procedure, and 50X to 2000X magnification within submicron scale resolution. In addition, the video measurement system was connected to a computer and capable of capturing digital images of specimen using a FlashBus FBG program.

The optical microscope is mainly used for direct visual observation, or preliminary observation for final characterization. In conjunction with a measurement system, this device provides the capability for two-dimension measurement within micron resolution. It is an accessible and affordable device for a typical laboratory. However, it still has many limitations within the range of measurement or resolution, including limited magnification, lack in three-dimensional analysis or surface topography. Hence, other measurement techniques, such as an electron microscope or surface-measuring device, are necessary to facilitate the micro-scale characterization.

Surface Contact Profilometer

This device applies a contact measurement technique to inpect the surface profile of the microstructure. The instrument uses a probe or a stylus to run along the surface of interest to evaluate the surface profile and projects on the device's monitor or plots on a graph-sketching machine. Some profilometer uses special tools such as diamonds to identify the characteristics of that profile within nanometer resolution. In general, profilometer uses a transducer inside the system to convert the traced result into numerical data or graph on the monitor or other output devices.

The contact profilometer that was used to verify the experimental result in this study is the DEKTAK 3 Surface Profiler from VEECO Metrology Group, Inc. Pictures below show the DEKTAK 3 system currently used in Nano Micro Fabrication facility at Oregon Nanoscience and Microtechnology Institute.

DEKTAK 3 profiler is capable of vertical measurements up to 2 mm with a 1nm, 1-sigma step height repeatability. The DEKTEK 3 consists of two parts: the stylus profiler unit, and the computer to control the machine. The profiler unit is used to measure the vertical surface profile of a sample. A diamond-tipped stylus is lowered onto the sample, and the stage is slowly translated, causing the stylus to move up and down vertically as it moves along the surface. The vertical motion of the stylus is measured electrically and converted to a digital format. The profile can be viewed on

the screen and saved to disk to be printed. With this capability, topography of fin laminae before and after pressure applied can be accurately verified.

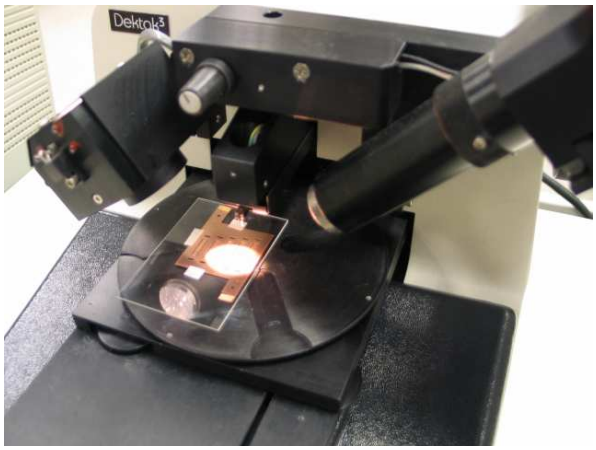

Vernier Micrometer

The Vernier micrometer was used for measuring the thickness of the laminae. Micrometer is commonly used in industry for securing small measurements. Its purpose is to measure objects with high accuracy of 0.0001 inch. The Vernier micrometer consists of three parts: spindle, sleeve, and thimble. The readings from the micrometer were validated with the surface contact profilometer.

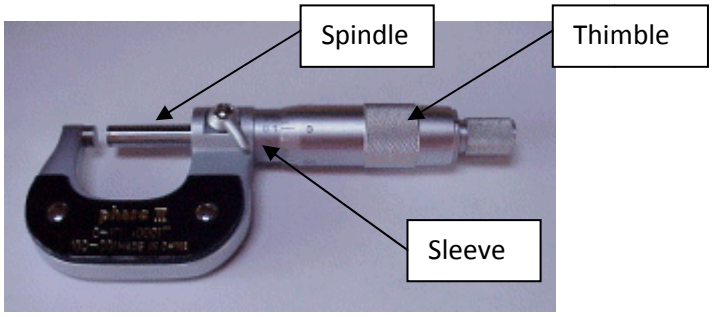

APPENDIX E

Surface Roughness

Surface roughness is commonly specified as either arithmetic average (center line average roughness) or root mean square average roughness. The arithmetic average, denoted in ISO 4287 as R_a, is the average deviation of the surface from a mean line or centerline. The arithmetical average deviation from the mean line is

$$R_a = \frac{1}{l}\int_0^l |y| dl$$

where

R_a = arithmetical average deviation from the mean line
y = ordinate of curve of profile
l = length over which average is taken

An approximate of average roughness may be obtained by adding the y increments, as shown in the Figure below, and dividing the sum by the number of increments taken:

$$R_a = \frac{\sum_{x=1}^{x=n}(y_x)}{n}$$

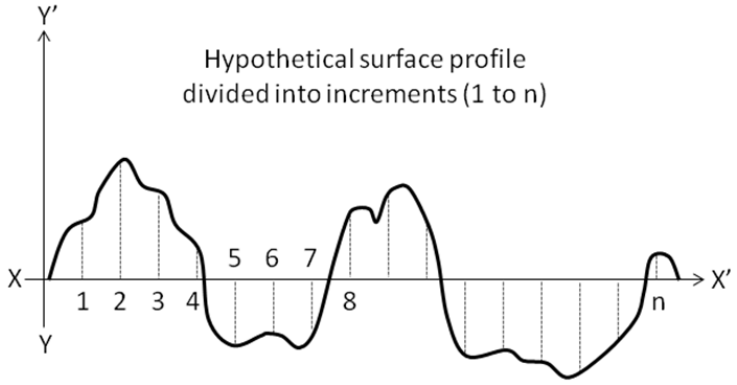

The root mean square average roughness, denoted in ISO 4287 by R_q, is calculated by taking a series of measurements of deviations from the center line and taking their root mean square. It is defined mathematically as:

$$R_q = \left[\frac{1}{l}\int_0^l y^2 dl\right]^{1/2}$$

An approximation of the root mean square average roughness may be obtained by adding the square of the y increments, shown in Figure above, dividing the sum by the number of increments taken, and extracting the square root:

$$R_q = \left[\frac{\sum_{x=1}^{x=n}(y_x{}^2)}{n}\right]^{1/2}$$

R_q is more sensitive to occasional high and low peaks, and gives more weight to higher peaks. Other important specifications include maximum peak to valley roughness height and ten point height. Maximum peak to valley roughness is denoted in ISO 4287 as R_t and is the distance between two lines parallel to the center line that contacts the extreme upper and lower points on the profile within the sampling length. (Dallas, 1976[1]; ISO 4287, 1997[2])

Roughness sampling length is the distance between the successive data points being record in a scan whereas the evaluation length is basically the length of the scan being taken to measure the surface roughness. The following table (taken from ISO 4288, specifies the roughness sampling length and roughness evaluation length for a given center line average roughness (ISO 4288, 1996[3]).

R_a range	Roughness sampling length	Roughness evaluation length
µm	mm	mm
$(0.006) < R_a \leq 0.02$	0.08	0.40
$0.02 < R_a \leq 0.1$	0.25	1.25
$0.1 < R_a \leq 2$	0.80	4.00
$2 < R_a \leq 10$	2.50	12.50
$10 < R_a \leq 80$	8.00	40.00

[1] Dallas, D. B. (Editor-in-Chief), *Tool and Manufacturing Engineers Handbook, Third Edition*, Society of Manufacturing Engineer, McGraw-Hill Book Company, New York, USA, 1976

[2] ISO 4287, "Geometric Product Specification (GPS) – Surface Texture: Profile Method – Terms, Definitions and Surface Texture Parameters," *International Organization for Standardization*, Geneve, Switzerland, 1997

[3] ISO 4288, "Geometric Product Specification (GPS) – Surface Texture: Profile Method – Rules and Procedures for the Assessment of Surface Texture," *International Organization for Standardization*, Geneve, Switzerland, 1996

APPENDIX F

Test Coupon Design for Mis-registration Experiment

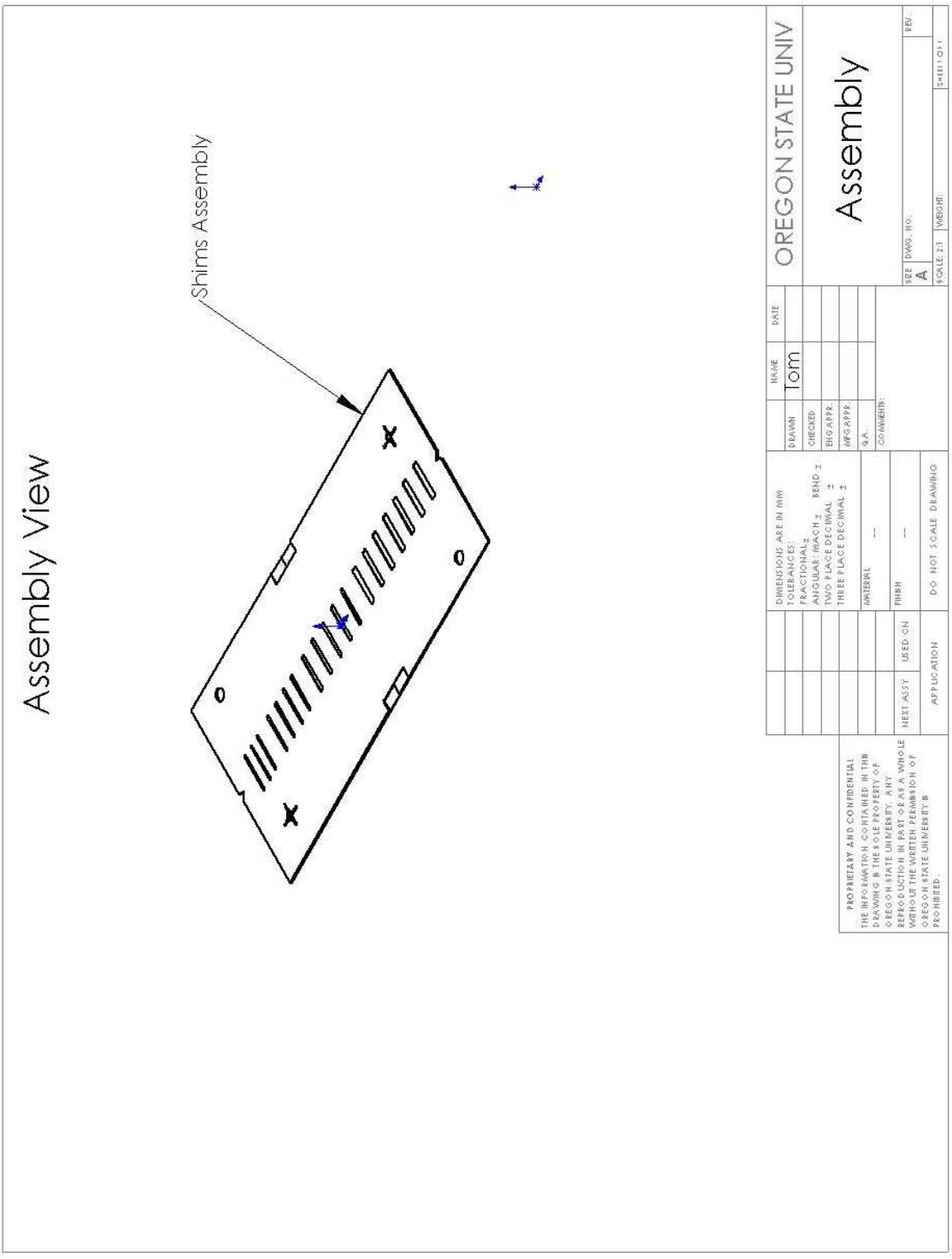

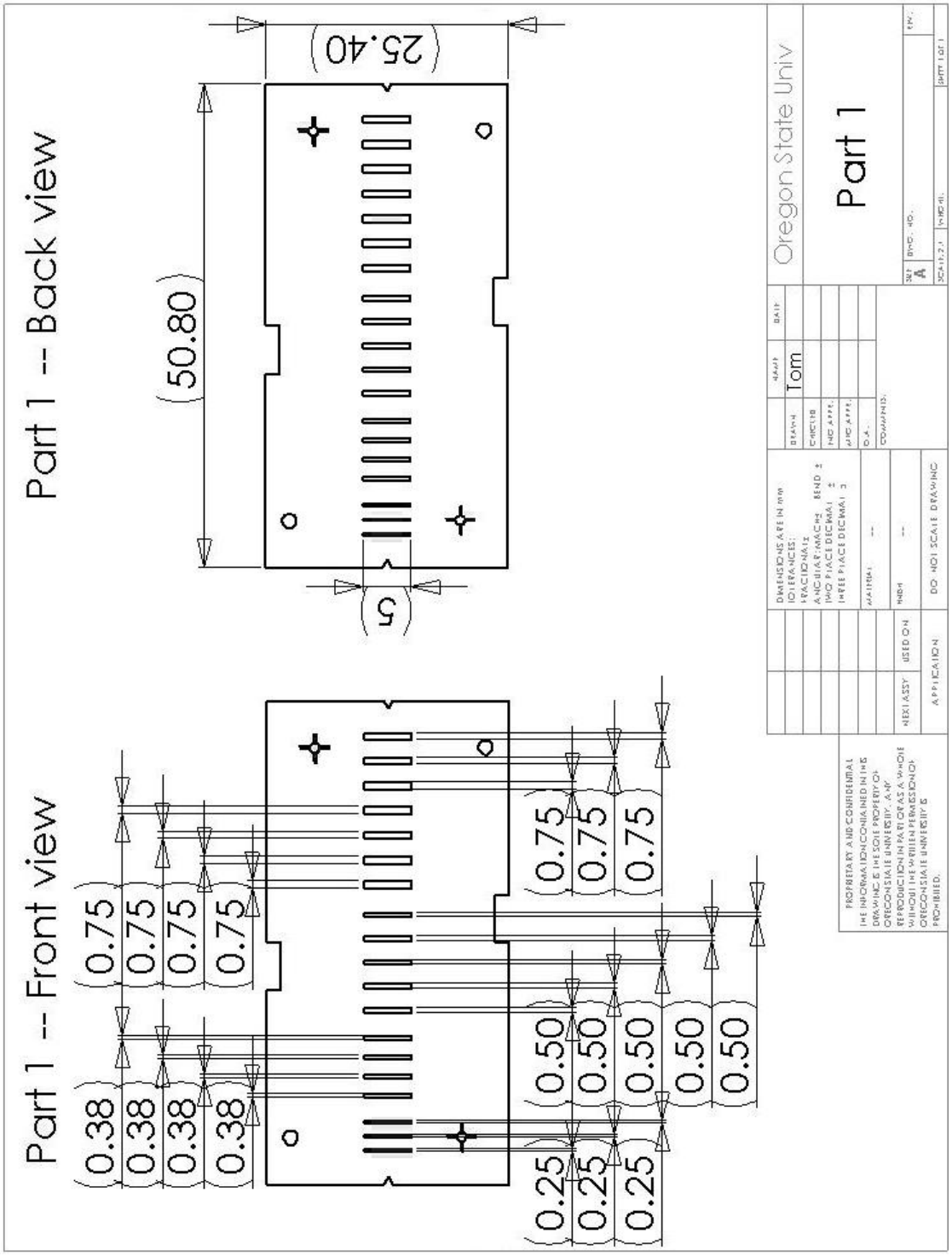
Part 1 -- Front view
Part 1 -- Back view
0.38
0.75
0.50
0.25
(50.80)
(25.40)
(5)
Part 1
Oregon State Univ
Tom

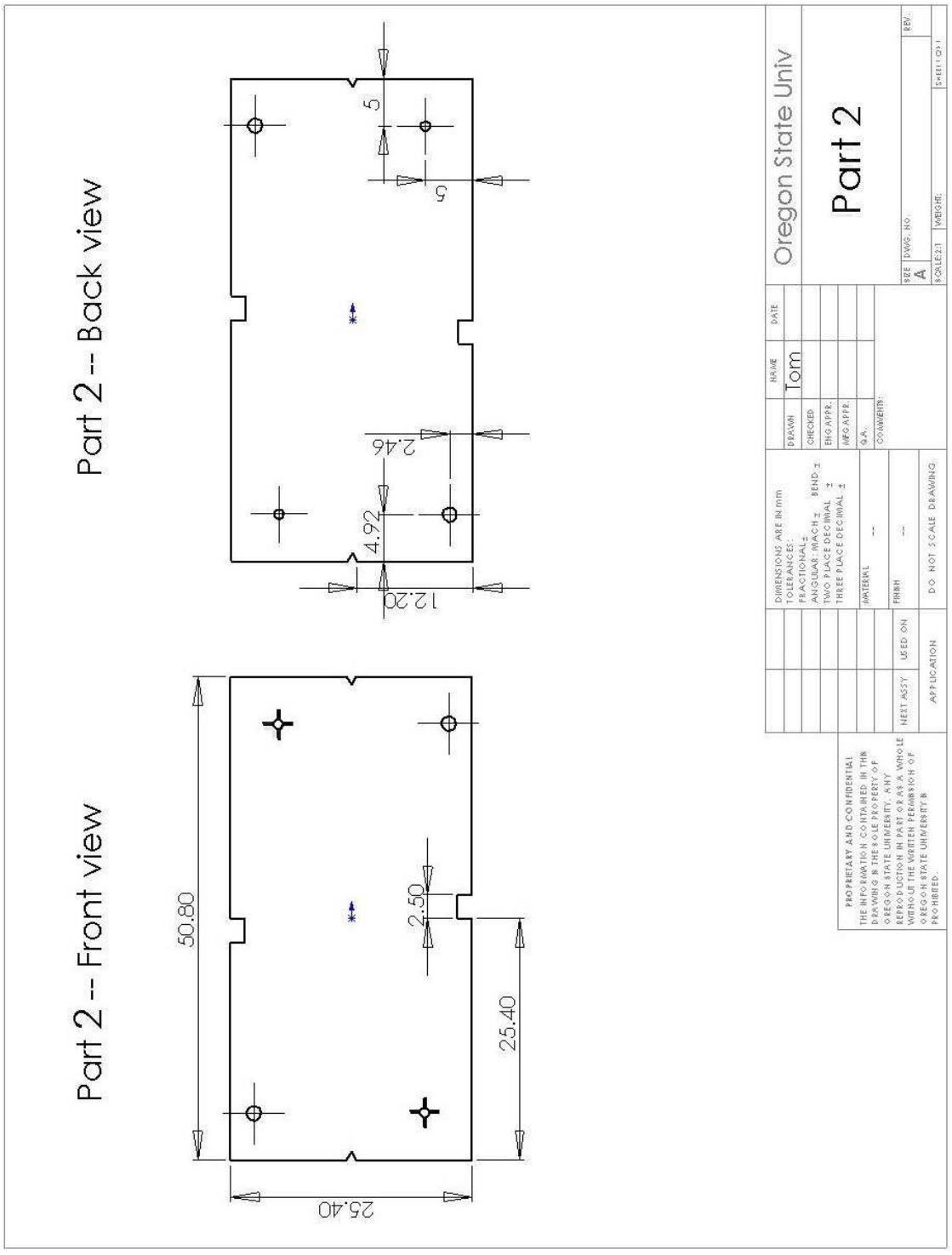
Part 2 -- Front view
Part 2 -- Back view
50.80
25.40
2.50
25.40
5
5
2.46
4.92
12.20
Oregon State Univ
Part 2
Tom
DRAWN
CHECKED
ENG APPR.
MFG APPR.
Q.A.
COMMENTS:
DIMENSIONS ARE IN mm
TOLERANCES:
FRACTIONAL ±
ANGULAR: MACH ± BEND ±
TWO PLACE DECIMAL ±
THREE PLACE DECIMAL ±
MATERIAL --
FINISH --
NEXT ASSY
USED ON
APPLICATION
DO NOT SCALE DRAWING
SIZE A
DWG. NO
REV
SCALE 2:1
WEIGHT:
SHEET 1 OF 1
PROPRIETARY AND CONFIDENTIAL
THE INFORMATION CONTAINED IN THIS DRAWING IS THE SOLE PROPERTY OF OREGON STATE UNIVERSITY. ANY REPRODUCTION IN PART OR AS A WHOLE WITHOUT THE WRITTEN PERMISSION OF OREGON STATE UNIVERSITY IS PROHIBITED.

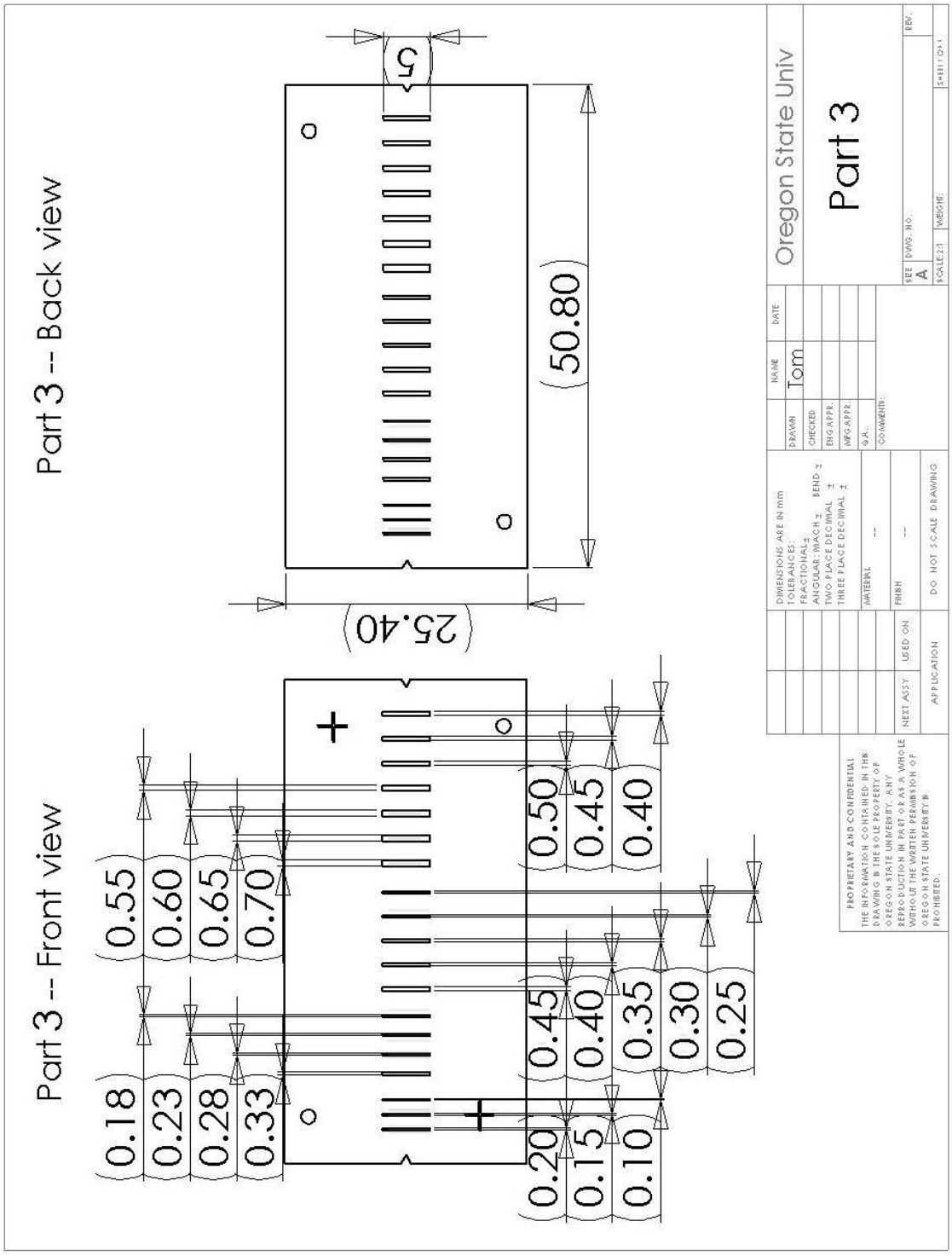
Part 3 -- Front view
Part 3 -- Back view
0.18
0.23
0.28
0.33
0.55
0.60
0.65
0.70
0.20
0.15
0.10
0.45
0.40
0.35
0.30
0.25
0.50
0.45
0.40
(25.40)
(50.80)
5
Oregon State Univ
Part 3
Tom
PROPRIETARY AND CONFIDENTIAL
THE INFORMATION CONTAINED IN THIS DRAWING IS THE SOLE PROPERTY OF OREGON STATE UNIVERSITY. ANY REPRODUCTION IN PART OR AS A WHOLE WITHOUT THE WRITTEN PERMISSION OF OREGON STATE UNIVERSITY IS PROHIBITED.
DO NOT SCALE DRAWING

APPENDIX G

Fiducial Design for Alignment

The registration features are designed so that when three test coupons are stacked, it can be visually validated from the top using a traditional microscope (see Appendix D for measuring equipment summaries). The following figures show the registration feature design for each individual layer. The circles are through cut features while the crosses are blind cuts.

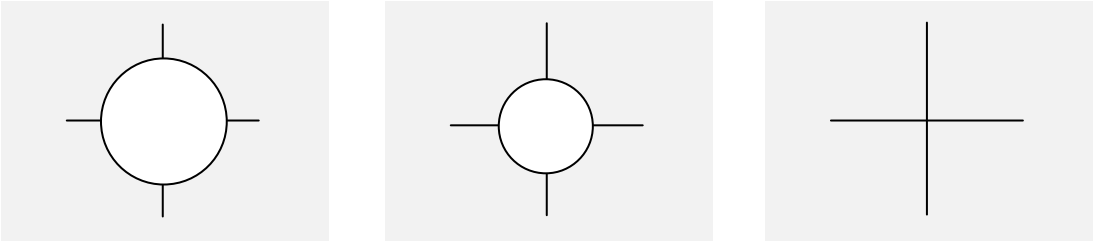

(a) (b) (c)

Registration design feature in top shim (a), middle shim (b), and bottom shim (c)

Figure below shows the actual image of how it looks under the microscope after three test coupons are stacked.

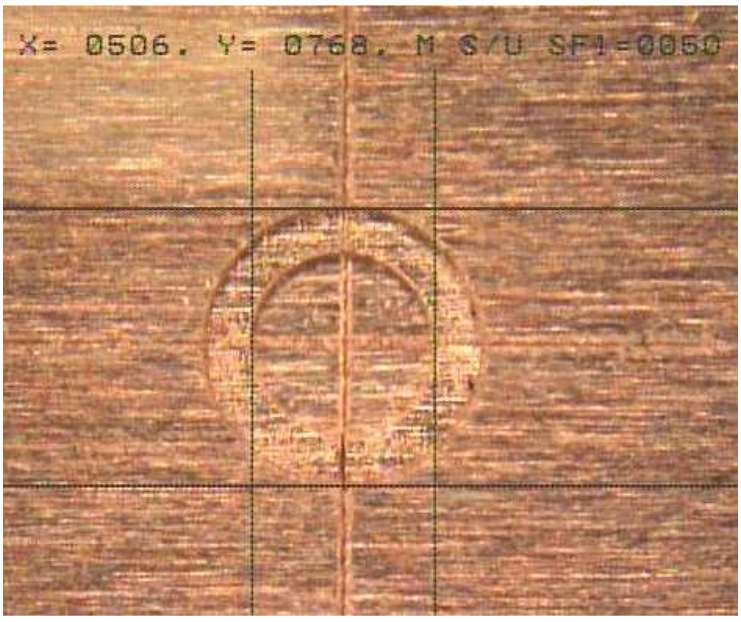

APPENDIX H

Preliminary Test Coupon Design (Sample S1 to S4)

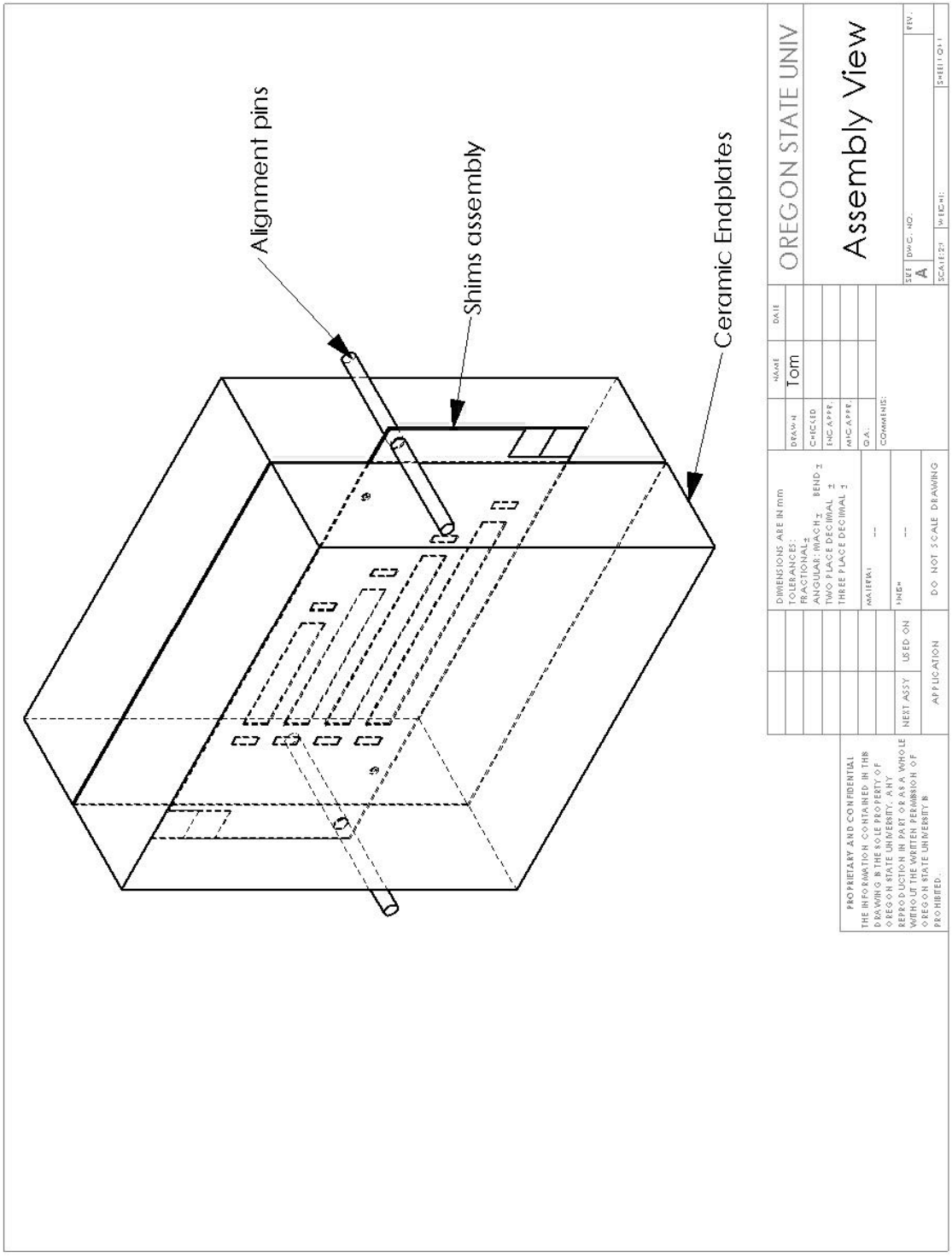

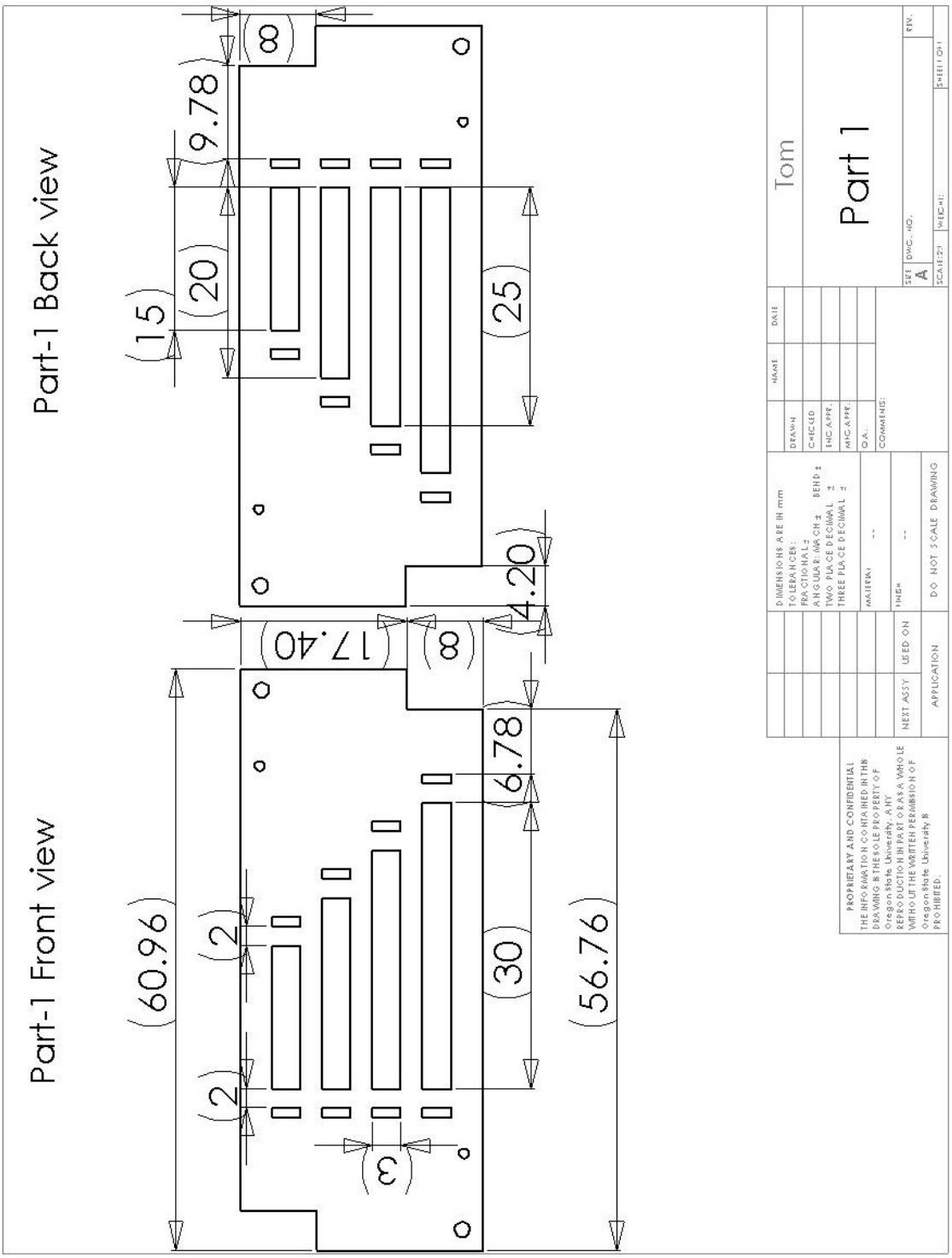
Part-1 Front view
Part-1 Back view
(60.96)
(2)
(2)
(3)
(30)
(56.76)
(17.40)
(8)
(4.20)
6.78
(8)
9.78
(15)
(20)
(25)
Tom
Part 1
PROPRIETARY AND CONFIDENTIAL
THE INFORMATION CONTAINED IN THIS DRAWING IS THE SOLE PROPERTY OF Oregon State University. ANY REPRODUCTION IN PART OR AS A WHOLE WITHOUT THE WRITTEN PERMISSION OF Oregon State University IS PROHIBITED.
DIMENSIONS ARE IN mm
TOLERANCES:
FRACTIONAL ±
ANGULAR: MACH ± BEND ±
TWO PLACE DECIMAL ±
THREE PLACE DECIMAL ±
MATERIAL --
FINISH --
NEXT ASSY
USED ON
APPLICATION
DO NOT SCALE DRAWING
NAME
DATE
DRAWN
CHECKED
ENG APPR.
MFG APPR.
Q.A.
COMMENTS:
SIZE A
DWG. NO.
REV.
SCALE: 2:1
WEIGHT:
SHEET 1 OF 1

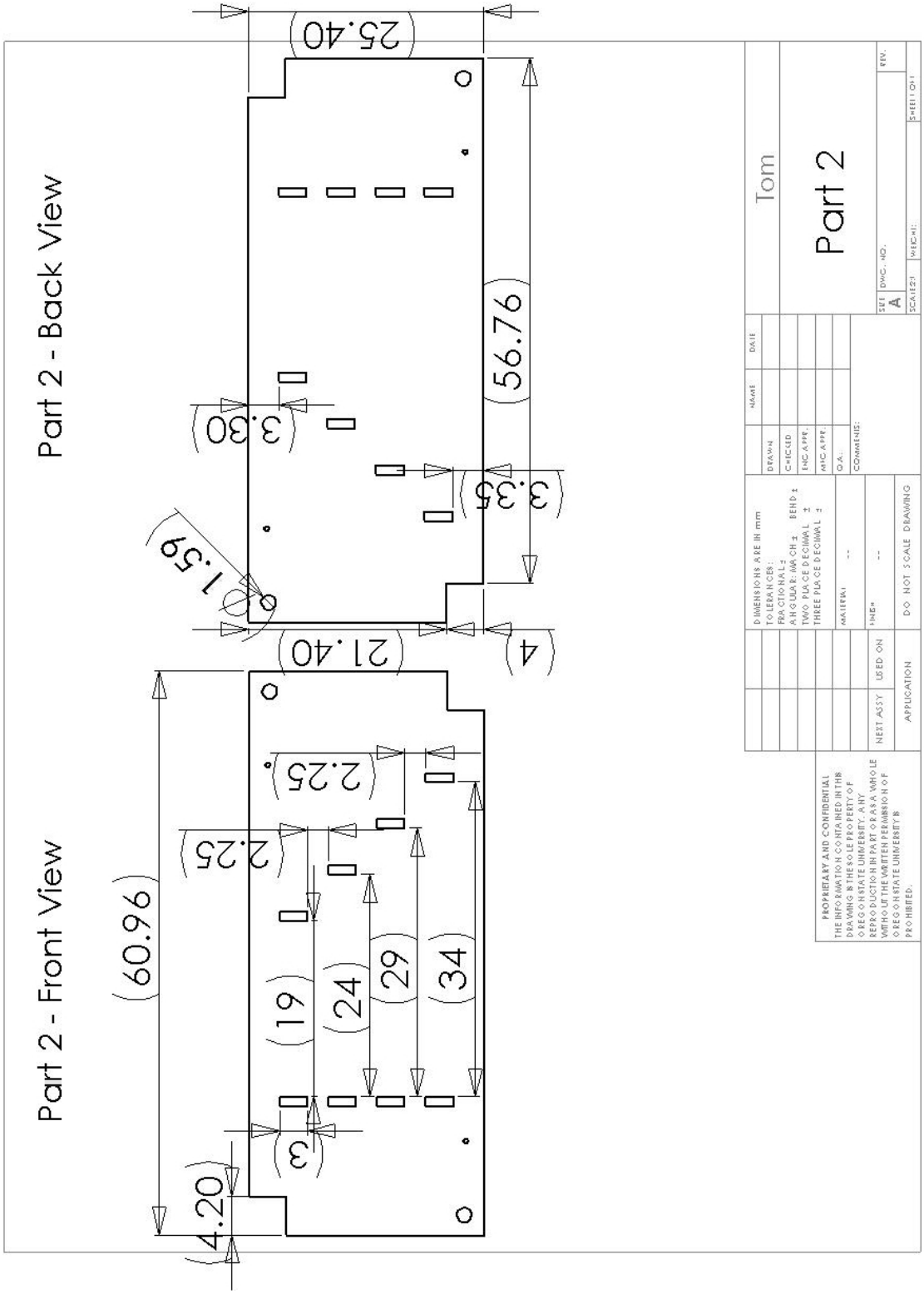
Part 2 - Front View
Part 2 - Back View
(60.96)
(19)
(24)
29
34
2.25
2.25
3
4.20
21.40
25.40
56.76
3.30
3.35
1.59
4
Tom
Part 2
DIMENSIONS ARE IN mm
TOLERANCES:
FRACTIONAL ±
ANGULAR: MACH ± BEND ±
TWO PLACE DECIMAL ±
THREE PLACE DECIMAL ±
DRAWN
CHECKED
ENG APPR.
MFG APPR.
Q.A.
COMMENTS:
NAME
DATE
MATERIAL
FINISH
NEXT ASSY
USED ON
APPLICATION
DO NOT SCALE DRAWING
SIZE
A
DWG. NO.
REV.
SCALE:
WEIGHT:
SHEET 1 OF 1
PROPRIETARY AND CONFIDENTIAL
THE INFORMATION CONTAINED IN THIS DRAWING IS THE SOLE PROPERTY OF ◇REGON STATE UNIVERSITY. ANY REPRODUCTION IN PART OR AS A WHOLE WITHOUT THE WRITTEN PERMISSION OF ◇REGON STATE UNIVERSITY IS PROHIBITED.

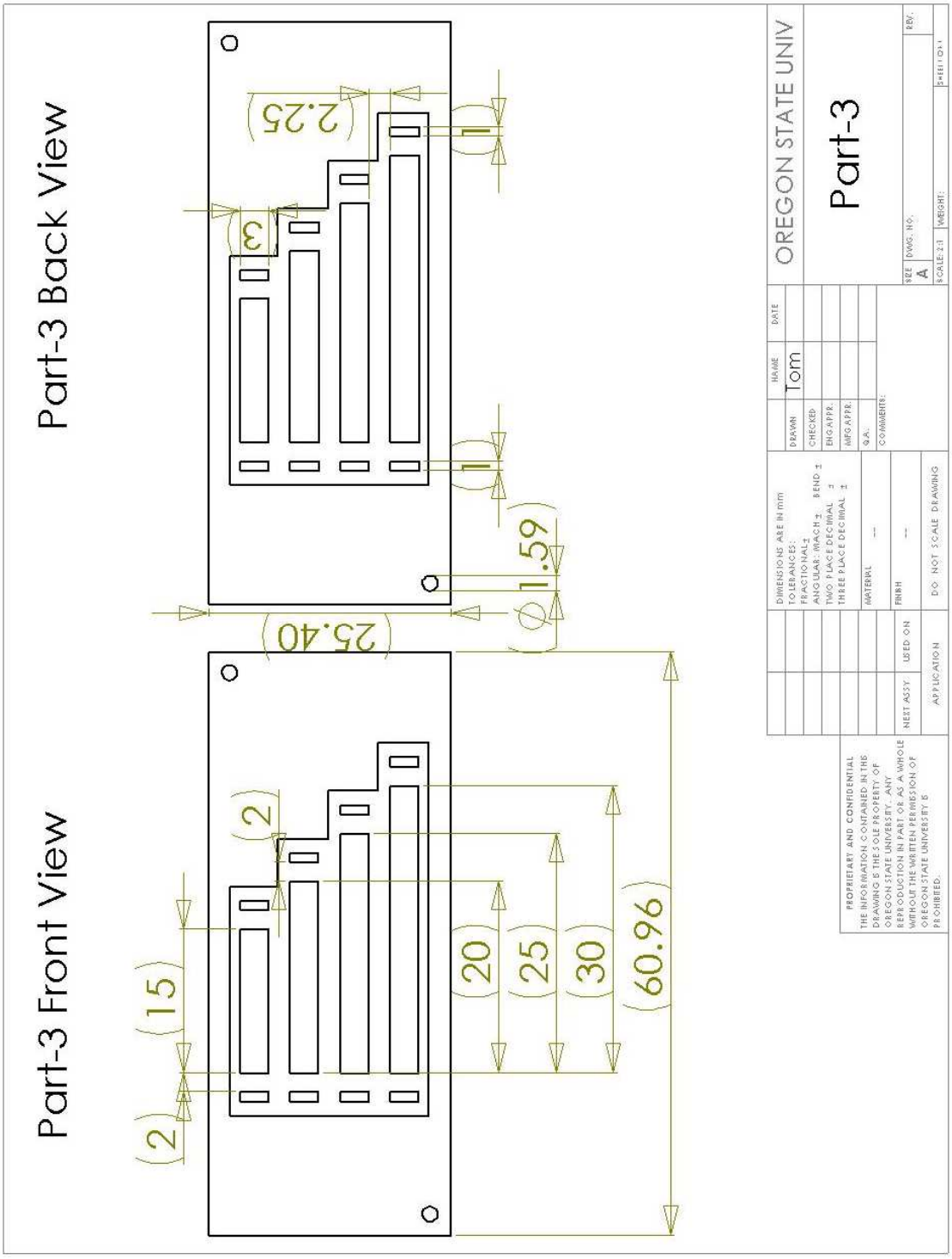
Part-3 Front View
Part-3 Back View
(2)
(15)
(2)
(20)
(25)
(30)
(60.96)
(25.40)
(Ø1.59)
(2.25)
(3)
(1)
(1)
PROPRIETARY AND CONFIDENTIAL
THE INFORMATION CONTAINED IN THIS DRAWING IS THE SOLE PROPERTY OF OREGON STATE UNIVERSITY. ANY REPRODUCTION IN PART OR AS A WHOLE WITHOUT THE WRITTEN PERMISSION OF OREGON STATE UNIVERSITY IS PROHIBITED.
DIMENSIONS ARE IN mm
TOLERANCES:
FRACTIONAL ±
ANGULAR: MACH ± BEND ±
TWO PLACE DECIMAL ±
THREE PLACE DECIMAL ±
MATERIAL —
FINISH —
NEXT ASSY: USED ON
APPLICATION
DO NOT SCALE DRAWING
NAME
DATE
DRAWN Tom
CHECKED
ENG APPR.
MFG APPR.
Q.A.
COMMENTS:
OREGON STATE UNIV
Part-3
SIZE A
DWG. NO.
REV:
SCALE: 2:1
WEIGHT:
SHEET 1 OF 1

APPENDIX I

Test Coupon Design for Structural Parameters *l* and *t* (Sample S0 to S8 and T0 to T4)

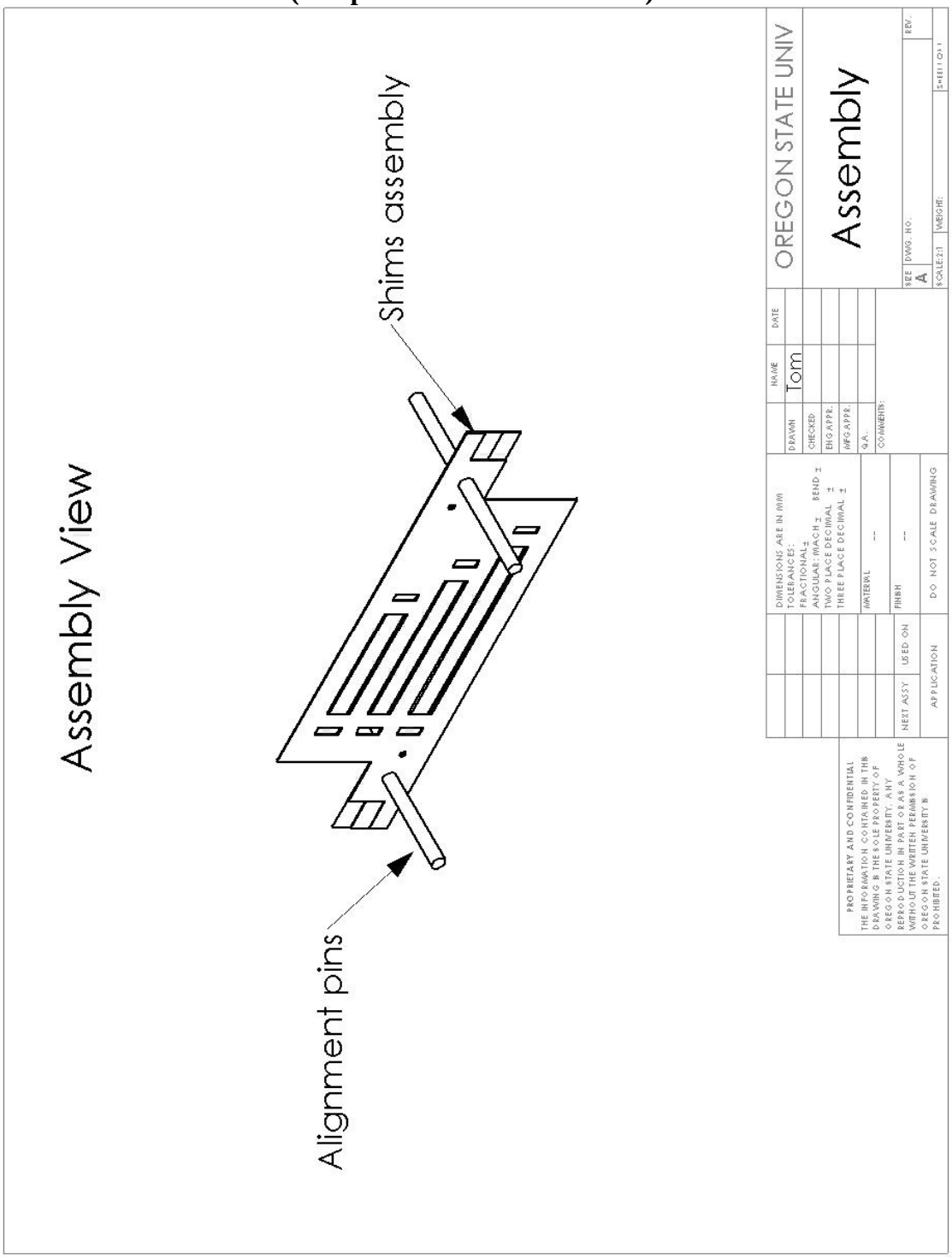

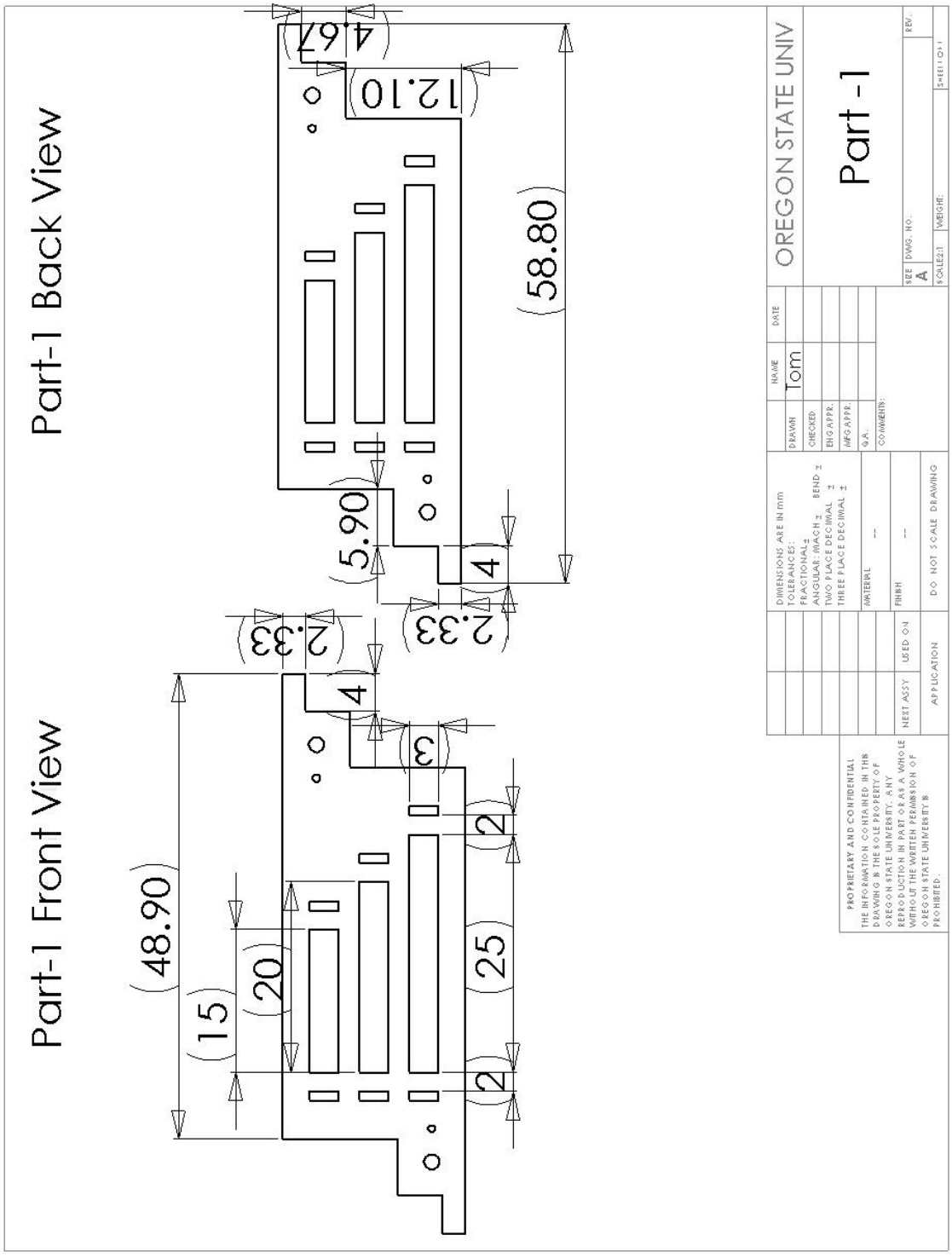
Part-1 Front View
Part-1 Back View
(48.90)
(15)
(20)
(25)
(2)
(2)
(3)
(4)
(2.33)
(2.33)
(5.90)
(4)
(58.80)
(12.10)
(4.67)
PROPRIETARY AND CONFIDENTIAL
THE INFORMATION CONTAINED IN THIS DRAWING IS THE SOLE PROPERTY OF OREGON STATE UNIVERSITY. ANY REPRODUCTION IN PART OR AS A WHOLE WITHOUT THE WRITTEN PERMISSION OF OREGON STATE UNIVERSITY IS PROHIBITED.
DIMENSIONS ARE IN mm
TOLERANCES:
FRACTIONAL ±
ANGULAR: MACH ± BEND ±
TWO PLACE DECIMAL ±
THREE PLACE DECIMAL ±
MATERIAL
FINISH
NEXT ASSY
USED ON
APPLICATION
DO NOT SCALE DRAWING
NAME
DATE
DRAWN
Tom
CHECKED
ENG APPR.
MFG APPR.
Q.A.
COMMENTS:
OREGON STATE UNIV
Part -1
SIZE
A
DWG. NO.
REV
SCALE:2:1
WEIGHT:
SHEET 1 OF 1

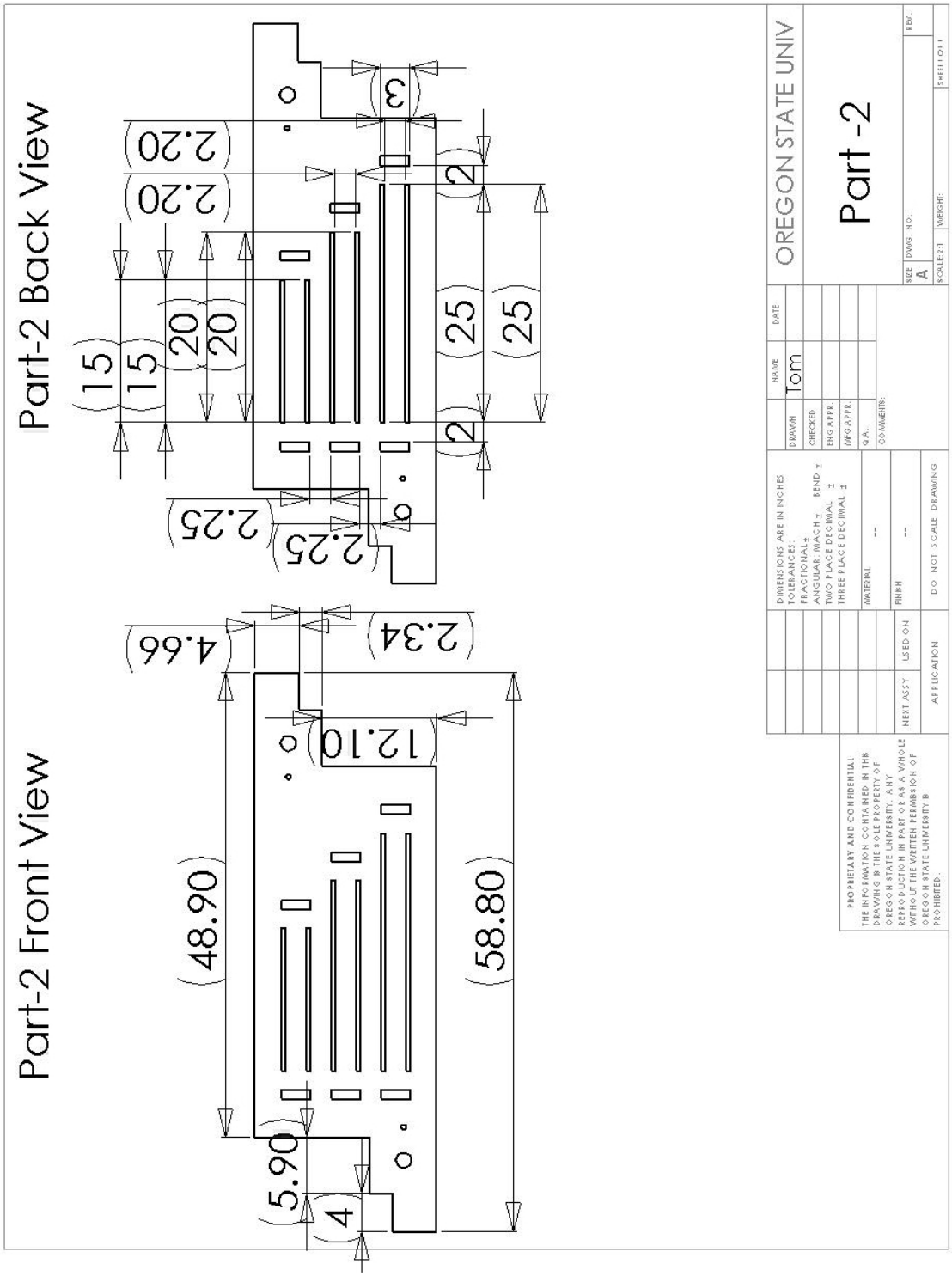
Part-2 Front View
Part-2 Back View
(48.90)
(58.80)
(5.90)
(4.66)
(2.34)
(12.10)
(4)
(2.25)
(2.25)
(15)
(15)
(20)
(20)
(2.20)
(2.20)
(3)
(2)
(2)
(25)
(25)
PROPRIETARY AND CONFIDENTIAL
THE INFORMATION CONTAINED IN THIS DRAWING IS THE SOLE PROPERTY OF ◇REGON STATE UNIVERSITY. ANY REPRODUCTION IN PART OR AS A WHOLE WITHOUT THE WRITTEN PERMISSION OF ◇REGON STATE UNIVERSITY IS PROHIBITED.
NEXT ASSY
USED ON
APPLICATION
DIMENSIONS ARE IN INCHES
TOLERANCES:
FRACTIONAL ±
ANGULAR: MACH ± BEND ±
TWO PLACE DECIMAL ±
THREE PLACE DECIMAL ±
MATERIAL --
FINISH --
DO NOT SCALE DRAWING
NAME
DATE
DRAWN
Tom
CHECKED
ENG APPR.
MFG APPR.
Q.A.
COMMENTS:
OREGON STATE UNIV
Part -2
SIZE
A
DWG. NO.
REV.
SCALE: 2:1
WEIGHT:
SHEET 1 OF 1

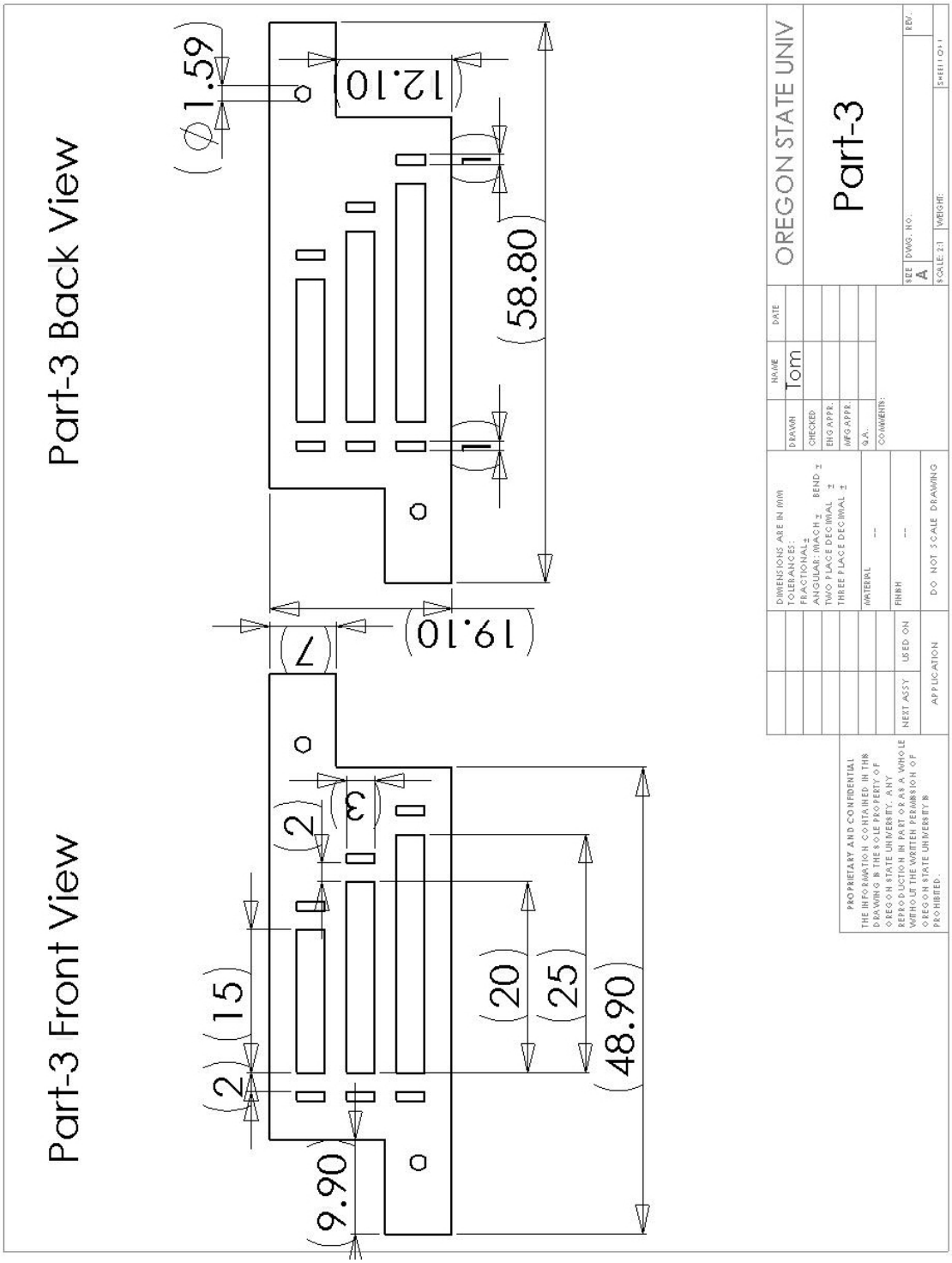
Part-3 Front View
Part-3 Back View
Ø1.59
12.10
58.80
19.10
7
2
3
2
15
20
25
48.90
9.90
1
1
PROPRIETARY AND CONFIDENTIAL
THE INFORMATION CONTAINED IN THIS DRAWING IS THE SOLE PROPERTY OF OREGON STATE UNIVERSITY. ANY REPRODUCTION IN PART OR AS A WHOLE WITHOUT THE WRITTEN PERMISSION OF OREGON STATE UNIVERSITY IS PROHIBITED.
DIMENSIONS ARE IN mm
TOLERANCES:
FRACTIONAL ±
ANGULAR: MACH ± BEND ±
TWO PLACE DECIMAL ±
THREE PLACE DECIMAL ±
MATERIAL —
FINISH —
NEXT ASSY
USED ON
APPLICATION
DO NOT SCALE DRAWING
NAME
DATE
DRAWN
Tom
CHECKED
ENG APPR.
MFG APPR.
Q.A.
COMMENTS:
OREGON STATE UNIV
Part-3
SIZE
A
DWG. NO.
REV.
SCALE: 2:1
WEIGHT:
SHEET 1 OF 1

APPENDIX J
Test Coupon Design for Mechanical Parameters *E* and *v*
(Sample E1, E3, and E5)

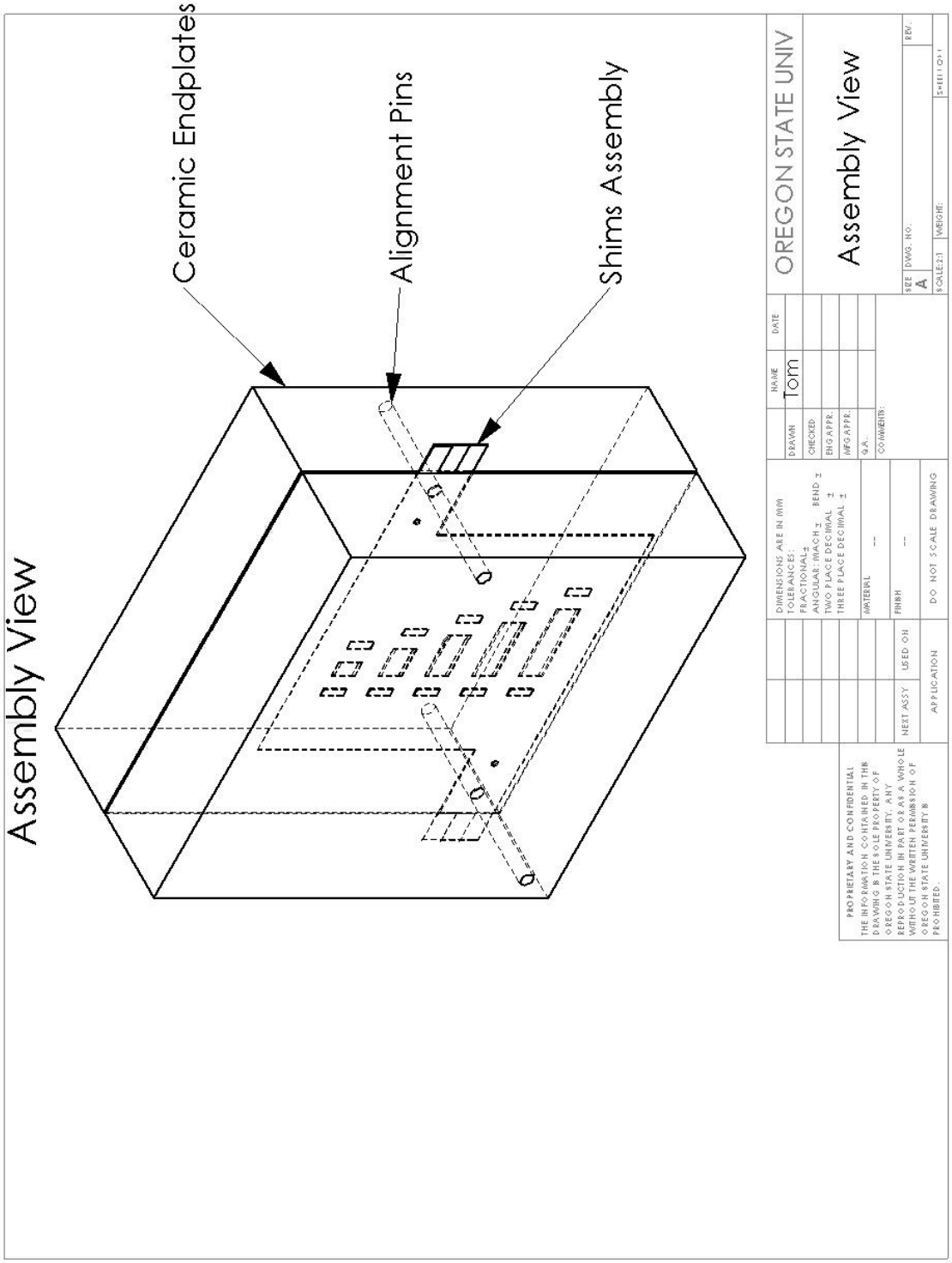

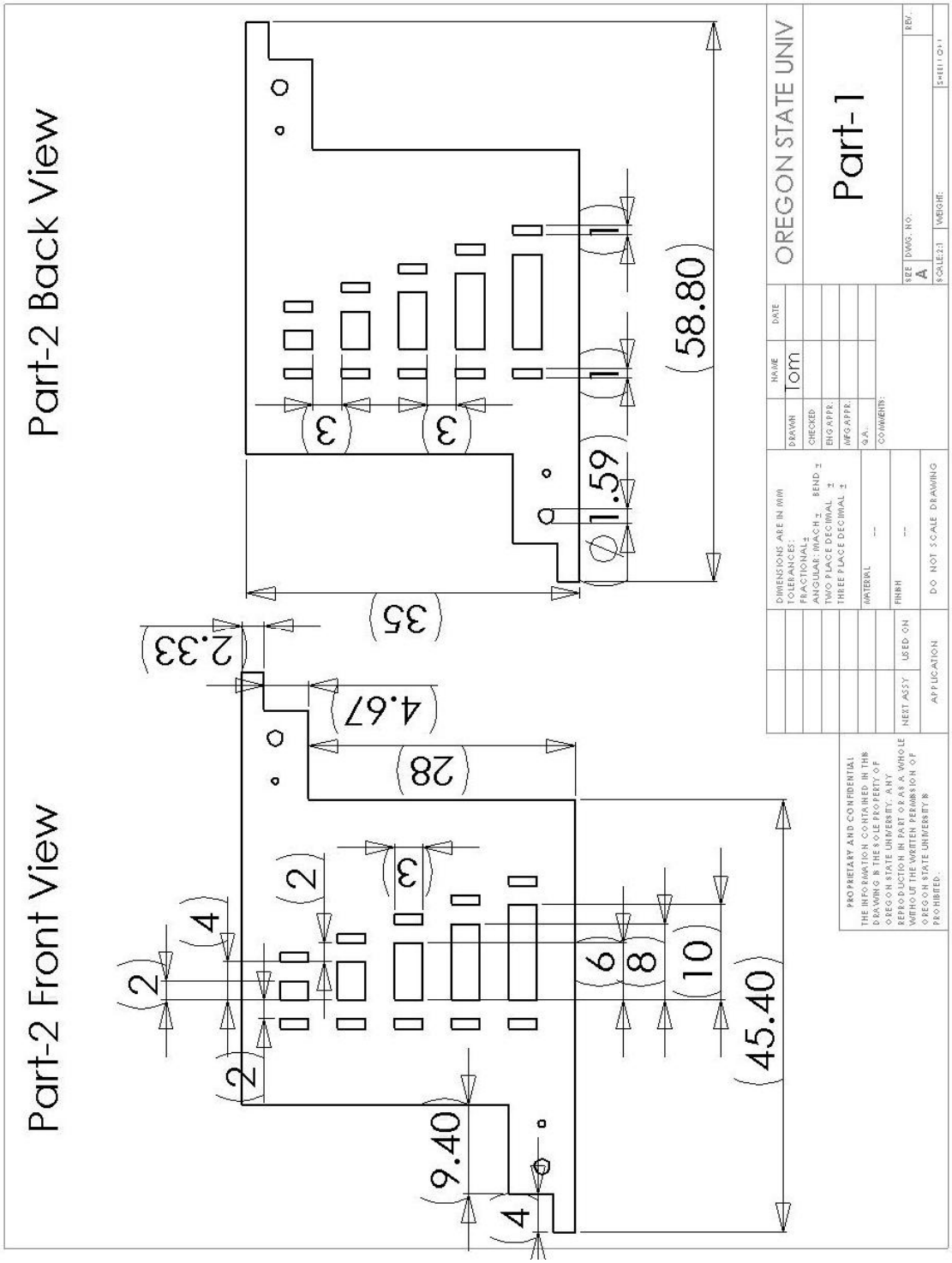
Part-2 Front View
Part-2 Back View
Part-1
OREGON STATE UNIV
Tom
PROPRIETARY AND CONFIDENTIAL
THE INFORMATION CONTAINED IN THIS DRAWING IS THE SOLE PROPERTY OF OREGON STATE UNIVERSITY. ANY REPRODUCTION IN PART OR AS A WHOLE WITHOUT THE WRITTEN PERMISSION OF OREGON STATE UNIVERSITY IS PROHIBITED.
DO NOT SCALE DRAWING
SIZE A
SCALE:2:1
WEIGHT:
SHEET 1 OF 1

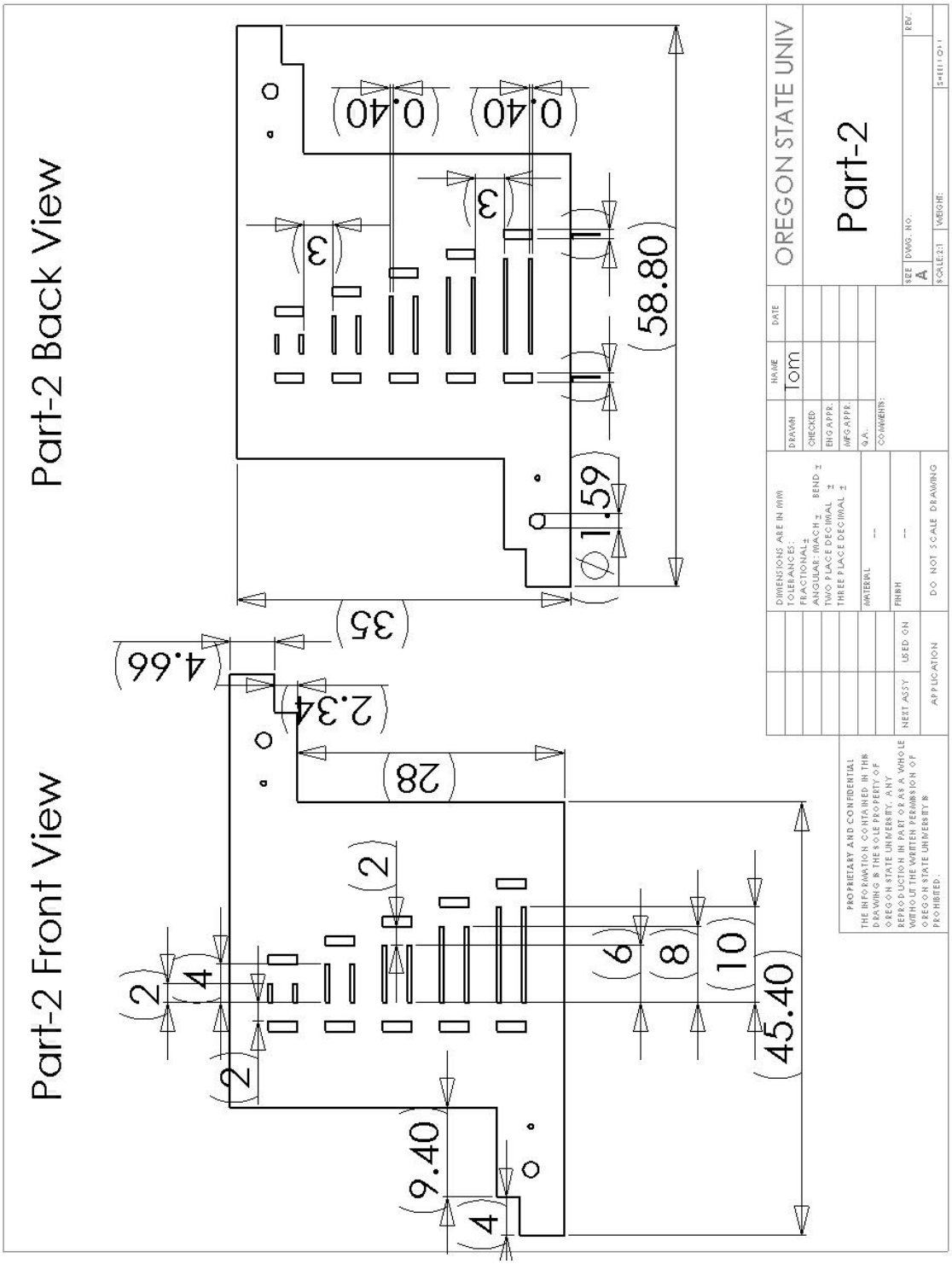
Part-2 Front View
Part-2 Back View
Part-2
OREGON STATE UNIV
PROPRIETARY AND CONFIDENTIAL
THE INFORMATION CONTAINED IN THIS DRAWING IS THE SOLE PROPERTY OF OREGON STATE UNIVERSITY. ANY REPRODUCTION IN PART OR AS A WHOLE WITHOUT THE WRITTEN PERMISSION OF OREGON STATE UNIVERSITY IS PROHIBITED.
DIMENSIONS ARE IN MM
TOLERANCES:
FRACTIONAL ±
ANGULAR: MACH ± BEND ±
TWO PLACE DECIMAL ±
THREE PLACE DECIMAL ±
MATERIAL
FINISH
NEXT ASSY
USED ON
APPLICATION
DO NOT SCALE DRAWING
DRAWN
CHECKED
ENG APPR.
MFG APPR.
Q.A.
COMMENTS:
NAME
DATE
tom
SIZE
A
DWG. NO.
REV.
SCALE: 2:1
WEIGHT:
SHEET 1 OF 1

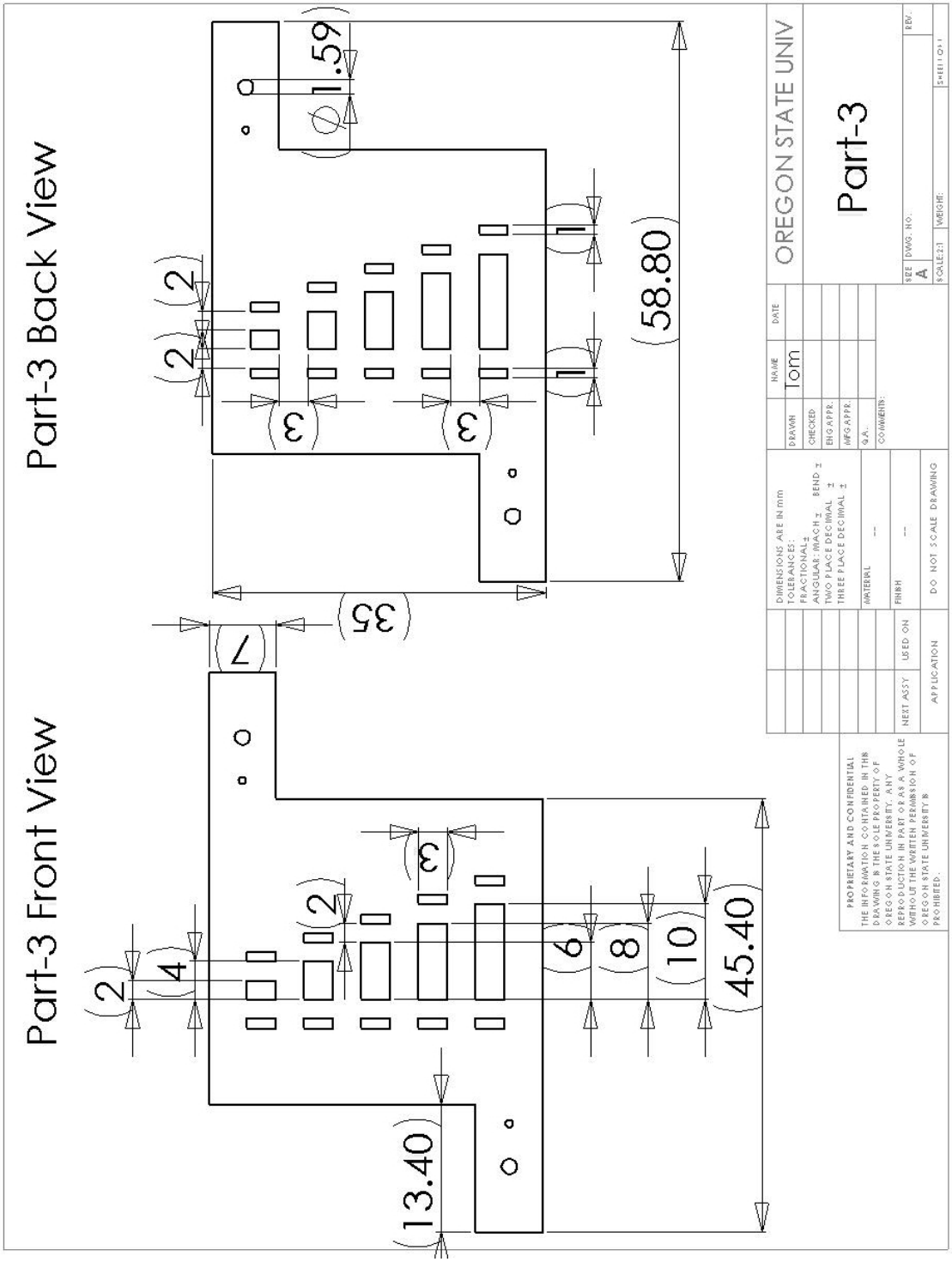
Part-3 Front View
Part-3 Back View
Part-3
OREGON STATE UNIV
Tom
DRAWN
CHECKED
ENG APPR.
MFG APPR.
Q.A.
COMMENTS:
NAME
DATE
DIMENSIONS ARE IN mm
TOLERANCES:
FRACTIONAL ±
ANGULAR: MACH ± BEND ±
TWO PLACE DECIMAL ±
THREE PLACE DECIMAL ±
MATERIAL
FINISH
NEXT ASSY
USED ON
APPLICATION
DO NOT SCALE DRAWING
SIZE
A
DWG. NO.
REV.
SCALE: 2:1
WEIGHT:
SHEET 1 OF 1
PROPRIETARY AND CONFIDENTIAL
THE INFORMATION CONTAINED IN THIS DRAWING IS THE SOLE PROPERTY OF © REGON STATE UNIVERSITY. ANY REPRODUCTION IN PART OR AS A WHOLE WITHOUT THE WRITTEN PERMISSION OF © REGON STATE UNIVERSITY IS PROHIBITED.
58.80
45.40
35
13.40
Ø1.59

Test Coupon Design for Mechanical Parameters *E* and *v*
(Sample E2, E4, and E6)

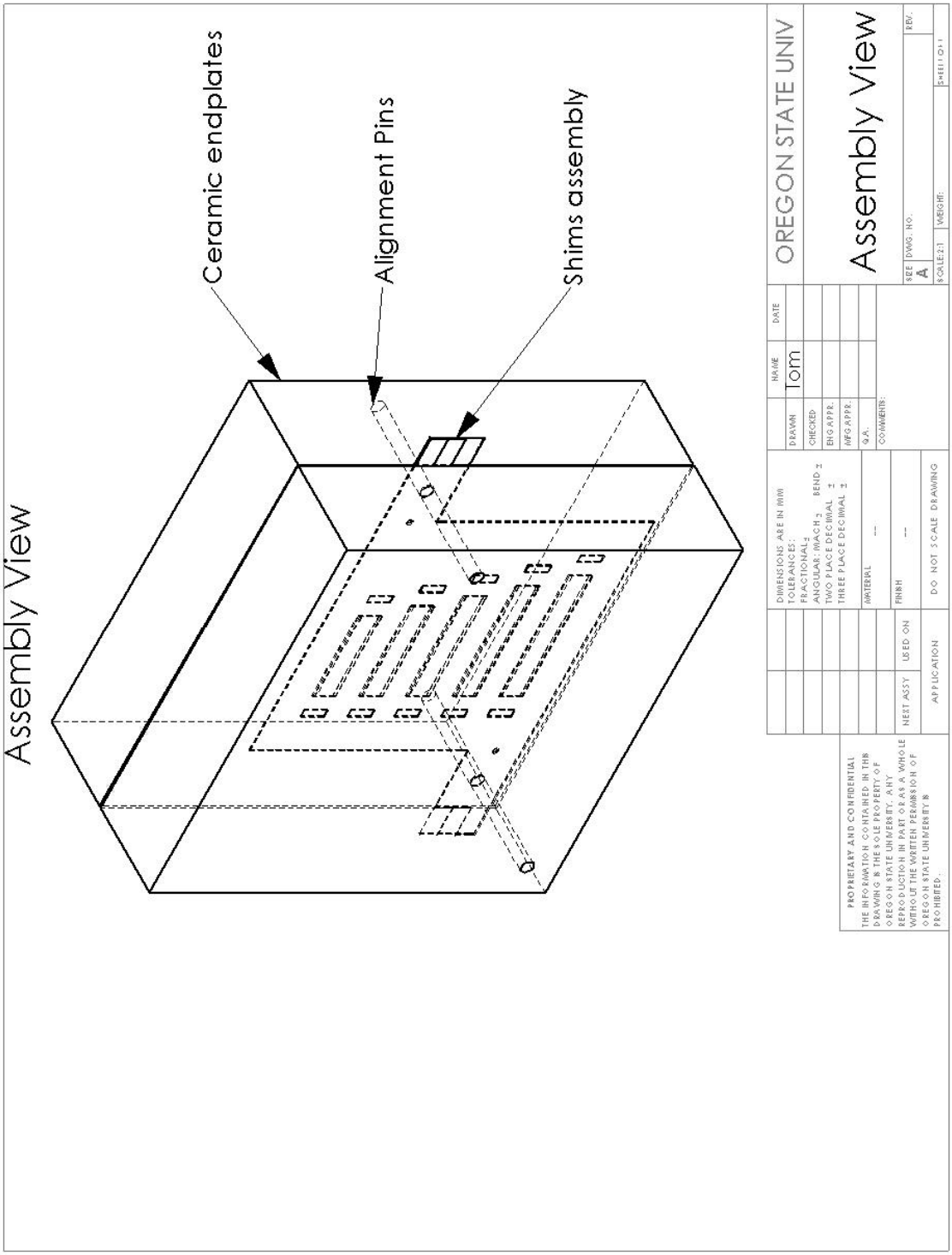

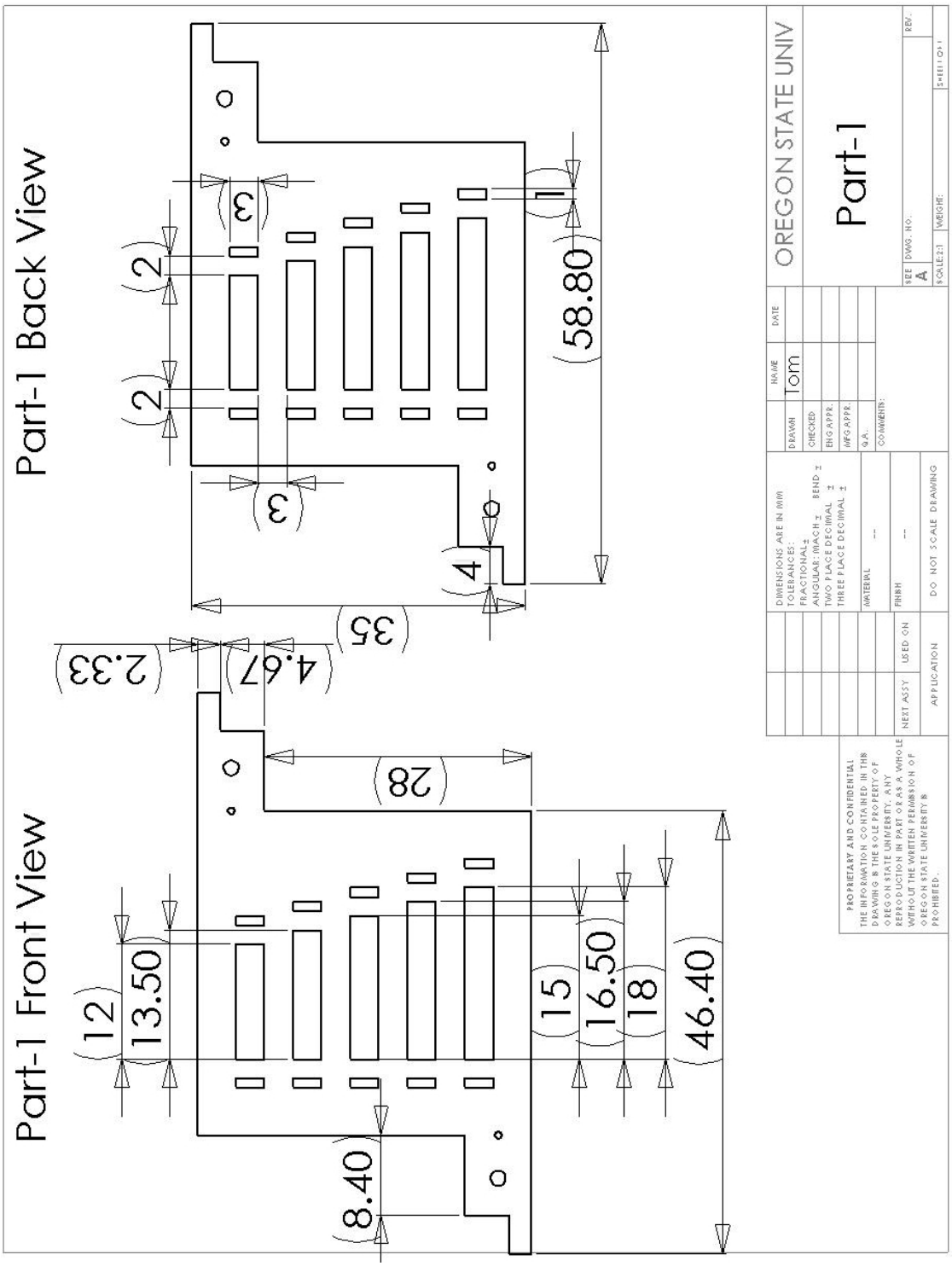
Part-1 Front View
Part-1 Back View
Part-1
OREGON STATE UNIV
Tom
PROPRIETARY AND CONFIDENTIAL
THE INFORMATION CONTAINED IN THIS DRAWING IS THE SOLE PROPERTY OF OREGON STATE UNIVERSITY. ANY REPRODUCTION IN PART OR AS A WHOLE WITHOUT THE WRITTEN PERMISSION OF OREGON STATE UNIVERSITY IS PROHIBITED.
DO NOT SCALE DRAWING

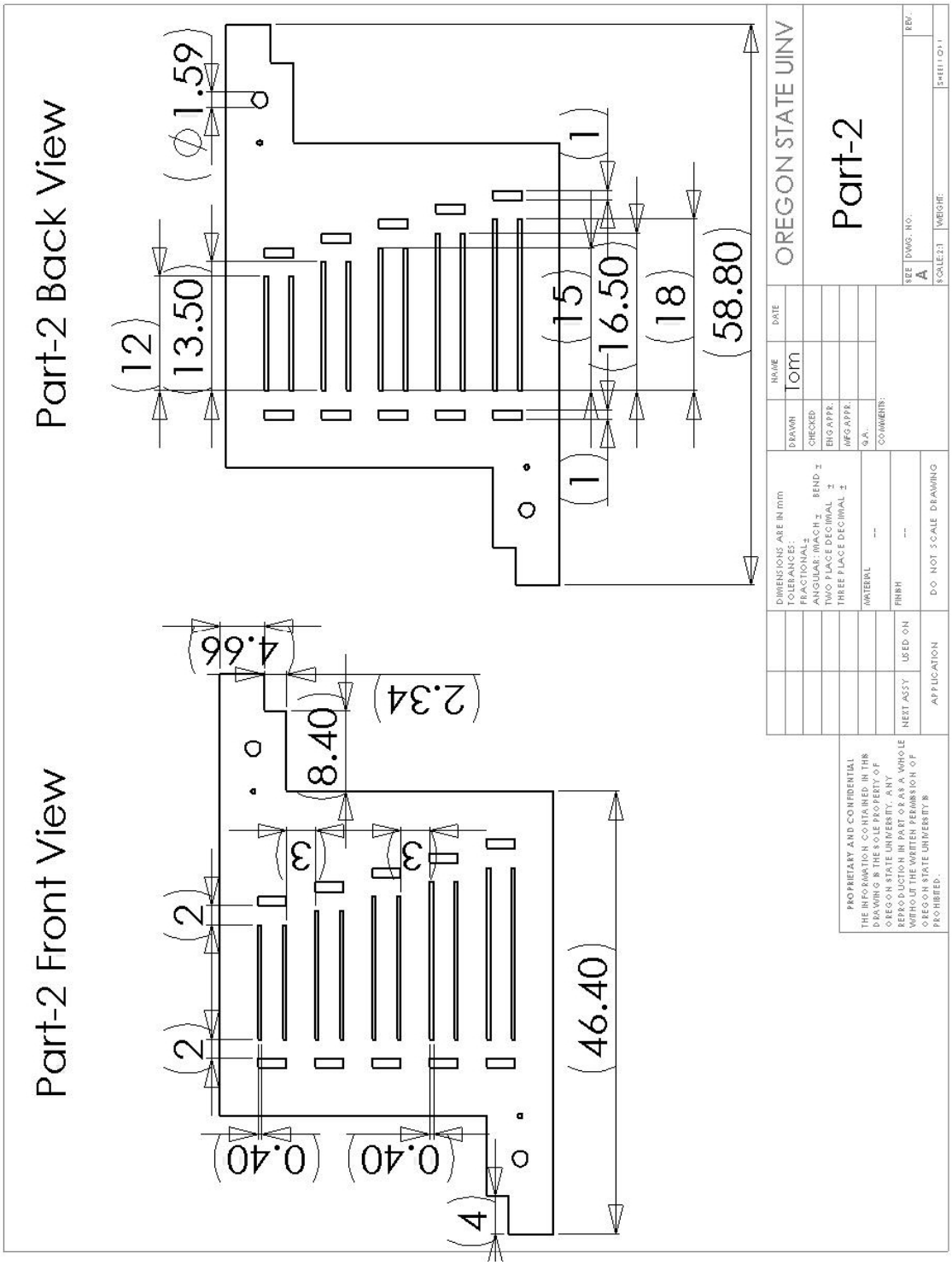
Part-2 Back View
Part-2 Front View
Part-2
OREGON STATE UINV
DIMENSIONS ARE IN mm
TOLERANCES:
FRACTIONAL ±
ANGULAR: MACH ± BEND ±
TWO PLACE DECIMAL ±
THREE PLACE DECIMAL ±
MATERIAL --
FINISH --
NEXT ASSY USED ON
APPLICATION
DO NOT SCALE DRAWING
DRAWN
CHECKED
ENG APPR.
MFG APPR.
Q.A.
COMMENTS:
NAME
DATE
tom
SIZE
A
DWG. NO:
REV:
SCALE:2:1
WEIGHT:
SHEET 1 OF 1
PROPRIETARY AND CONFIDENTIAL
THE INFORMATION CONTAINED IN THIS DRAWING IS THE SOLE PROPERTY OF OREGON STATE UNIVERSITY. ANY REPRODUCTION IN PART OR AS A WHOLE WITHOUT THE WRITTEN PERMISSION OF OREGON STATE UNIVERSITY IS PROHIBITED.
12
13.50
Ø1.59
1
15
16.50
18
58.80
4.66
2.34
8.40
2
2
3
3
0.40
0.40
46.40
4

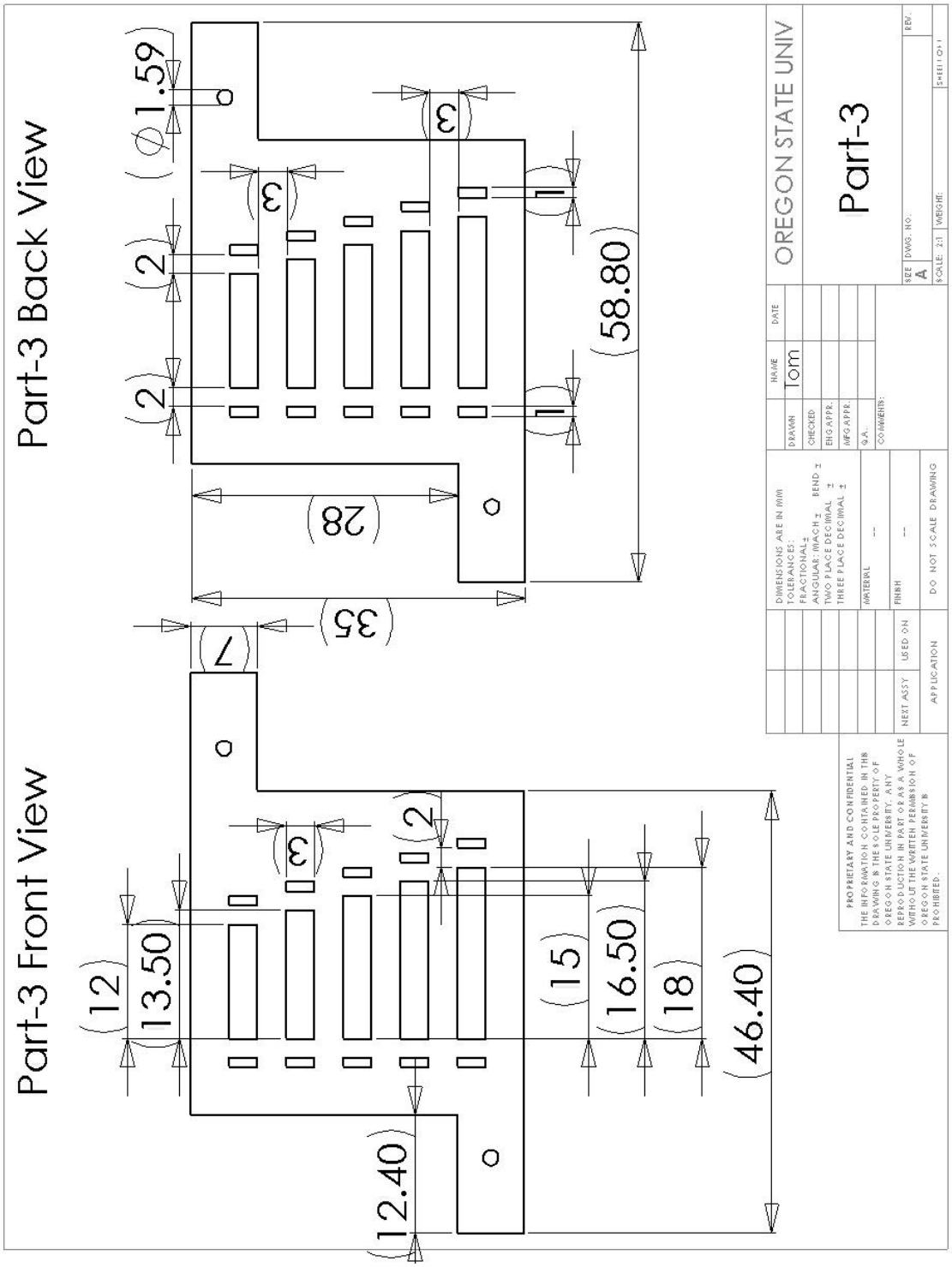
Part-3 Front View
Part-3 Back View
12
13.50
3
2
15
16.50
18
46.40
12.40
7
35
28
58.80
2
3
3
3
Ø1.59
PROPRIETARY AND CONFIDENTIAL
THE INFORMATION CONTAINED IN THIS DRAWING IS THE SOLE PROPERTY OF ◊ OREGON STATE UNIVERSITY. ANY REPRODUCTION IN PART OR AS A WHOLE WITHOUT THE WRITTEN PERMISSION OF ◊ OREGON STATE UNIVERSITY IS PROHIBITED.
NEXT ASSY
USED ON
APPLICATION
DO NOT SCALE DRAWING
DIMENSIONS ARE IN MM
TOLERANCES:
FRACTIONAL±
ANGULAR: MACH ± BEND ±
TWO PLACE DECIMAL ±
THREE PLACE DECIMAL ±
MATERIAL
FINISH
DRAWN
Tom
CHECKED
ENG APPR.
MFG APPR.
Q.A.
COMMENTS:
NAME
DATE
OREGON STATE UNIV
Part-3
SIZE
A
DWG. NO.
REV.
SCALE: 2:1
WEIGHT:
SHEET 1 OF 1

APPENDIX K

Test Coupon Design in Pluess's Publication